

METAL ADDITIVE MANUFACTURING OF TITANIUM ALUMINIDES FROM BLENDED ELEMENTAL POWDER

ASAVELA ZENANI

Dissertation submitted in fulfilment of the requirements for the Degree

MASTER OF ENGINEERING
In
MECHANICAL ENGINEERING

In the

Department of Mechanical and Mechatronics Engineering
Faculty of Engineering, Built Environment and Information Technology

At the

Central University of Technology, Free State

Supervisor: Prof W B du Preez

Co-supervisors: Prof I Yadroitsev

Dr T C Dzogbewu

BLOEMFONTEIN

May 2020

DECLARATION WITH REGARD TO INDEPENDENT WORK

I, ASAVELA ZENANI, identity number _____ and student number _____, do hereby declare that this research project submitted to the Central University of Technology, Free State for the Degree MASTER OF ENGINEERING IN MECHANICAL ENGINEERING, is my own independent work; and complies with the Code of Academic Integrity, as well as other relevant policies, procedures, rules and regulations of the Central University of Technology, Free State; and has not been submitted before to any institution by myself or any other person in fulfilment (or partial fulfilment) of the requirements for the attainment of any qualification.



May 2020

SIGNATURE OF STUDENT

DATE

ACKNOWLEDGEMENTS

I would like to thank God the eternal father for his everlasting favour and for granting me strength and wisdom to complete this work.

I would like to thank Prof. Willie du Preez for being my supervisor throughout the study; I would like to thank my co-supervisors Prof Igor Yadroitsev and Dr. Thywill Dzogbewu. I would like to express my gratitude to Dr. Thywill Dzogbewu for all the patience you have shown, for dedicating your time after hours to help me, motivating when I thought I would give up and for believing in me.

I would also like to send a message of gratitude to Dr. Ina Yadroitsava for always offering advice and guidance when she meets me working at the lab and for opening your doors whenever I had questions. I would like to thank Dean Koupryanoff for always helping me with my samples at the lab. I would like to thank Amos Muiruri for his contribution towards the success of this work.

My gratitude goes to my Mother for all her prayers towards my success, best friend Gaven Mahlalela for his support, prayers and vote of confidence throughout this degree. I would like to thank the Layman family for their endless support, for welcoming me in their home, for being understanding and for their prayers.

The South African Department of Science and Technology through the Collaborative Program in Additive Manufacturing supported this work, and I would to thank them for the opportunity.

ABSTRACT

Titanium aluminide is considered a key material for high performance gas turbines for aircraft engines, manufacturing of engine valves and a variety of automotive applications. This is due to the attractive high oxidation resistance and strength retention of the Titanium aluminide alloy at high temperatures.

The limitations of the conventional methods of manufacturing Titanium aluminide alloy components with precise geometry and near net shape functional characteristics have limited the usefulness of the Titanium aluminide alloys. However, additive manufacturing (AM) methods such as direct metal laser sintering (DMLS) have proven to have the capacity to uncover the full potential of the Titanium aluminide alloy by producing components with complex shapes.

The aim of this study was to determine the feasibility of using a blend of elemental Ti and Al powders in a DMLS system, to make parts that have comparable or better geometric, functional and microstructural properties to that of the conventionally processed titanium.

In this, study Ti6Al and Ti46Al alloys were investigated, using blends of elemental powders of Ti and Al. Single tracks were manufactured and single layers were built using a wide range of process parameters to determine the optimum process parameters for use in building good Titanium aluminide parts. Finally, two three-dimensional (3D) samples were built from Ti6Al (low Al content) and Ti46Al (high Al content).

The Ti6Al sample was built at the optimum parameters of laser power 150W and scanning speed 1.2m/s and the Ti46Al sample was built at the optimum parameters of 170W laser power and 0.1m/s scanning speed as identified in this study.

The Ti46Al 3D sample was not a success and further analysis could not be completed as the 3D sample collapsed.

The Ti6Al sample was a success, showing good overlapping of the single layers forming the 3D part. Good penetration depth of the single layers was achieved, complete melting and homogeneity of the powder were achieved, and finally, a good dense 3D part with $\alpha+\beta$ microstructure was achieved.

A 2% loss of Al in the produced 3D part of Titanium aluminide alloy, which was attributed to the differences in thermo-physical properties between the powders (Ti and Al).

The process of rescanning improved the homogeneity and promoted complete melting of the powder. Improving the mixing method of the powders prior to in-situ alloying improved the homogeneity of the alloy by reducing Al rich zones in the Ti matrix. A 2% Al loss allowance should be considered in further studies to ensure that the resultant alloy would meet the required compositional specification.

Keywords: Titanium aluminide, additive manufacturing, selective laser melting, elemental powder, Pre-alloying, Microstructure, Rescanning, Homogeneity

PUBLICATIONS AND PRESENTATIONS TO DATE

Zenani A., du Preez W. B., Dzogbewu T.C., Yadroitsev I. 2017. Metal additive manufacturing of Ti6Al4V from blended elemental powder. *Proceedings of the 18th Annual International RAPDASA Conference*, 8-10 November 2017.

Zenani A., du Preez W. B., Dzogbewu T.C., Yadroitsev I. 2017. Metal additive manufacturing of Ti6Al from blended elemental powder. *Proceedings of the 7th International COMA Conference*, 30 January – 01 February 2019.

A Zenani, T C Dzogbewu, W B du Preez & I Yadroitsev, *Optimum process parameters for direct metal laser sintering of Ti6Al powder blend*, Universal Journal of Mechanical Engineering, Vol 8, No 3, 2020.

CONTENTS

DECLARATION OF INDEPENDENT WORK	ii
ACKNOWLEDGEMENTS.....	iii
ABSTRACT	iv
PUBLICATIONS AND PRESENTATIONS TO DATE.....	6
LIST OF FIGURES.....	9
LIST OF TABLES	14
ABBREVIATIONS & NOMENCLATURE.....	15
CHAPTER 1 INTRODUCTION	16
1.1 Background.....	16
1.2. Problem Statement.....	18
1.3. Aim of the project	19
1.4. Objectives	19
1.5. An overview of the dissertation.....	19
CHAPTER 2- LITERATURE REVIEW	20
2.1 Titanium and Titanium alloys	20
2.1.1 Introduction	20
2.1.3 Titanium Alloying.....	21
2.1.4 Effects of Alloying Elements in Ti Alloys.....	22
2.1.5 Classes of Titanium alloys.....	23
2.2 Titanium aluminides	23
2.2.1 Introduction	23
2.2.2 The microstructure and deformation of titanium aluminides.....	28
2.2.3 Mechanical properties of Titanium aluminide-based alloys.....	32
2.2.4 Applications of Titanium aluminides	33
2.3 Additive manufacturing (AM).....	35
2.3.1 Introduction	35
2.3.2 Powder Bed Fusion.....	37
2.3.3 Direct Metal Laser Sintering	39
2.3.4 Powder Characteristics	45
2.3.5 Advantages and Disadvantages of DMLS	47
2.3.6 Optimizing the process parameters of DMLS	48
2.3.6.1 Single Tracks.....	48
2.3.6.2 Single Layers	53
2.3.6.3 3D Objects	56

2.4 Mechanical properties of DMLS Titanium aluminide -based alloys	59
CHAPTER 3 – METHODOLOGY.....	60
3.1. Schematic summary of the research methodology	60
3.1.1 Ti6Al experiment	62
3.1.2 Ti46Al Experiment - Run 1	71
3.1.3 Ti46Al experiment - Run 2.....	72
3.1.4 Ti46Al single layers and 3D samples experiment	73
CHAPTER 4.....	74
Results and Discussion.....	74
4.1 Ti6Al Experiment	74
4.1.1. Top surface analysis of the single tracks	74
4.1.2 Cross-sectional analysis of the single tracks	80
4.1.3 Top Surface Analysis of Ti6Al single layers.....	84
4.1.4 Cross-sectional analysis of single layers	86
4.2 Ti46Al Experiment Run 1	89
4.2.1. Top surface analysis of the single tracks.....	89
4.2.2. Cross sectional analysis of the Ti46Al single tracks	91
4.3 Ti46Al Experiment run 2.....	93
4.3.1. Top surface analysis of the single tracks	93
4.3.2. Cross sectional analysis of the single tracks	96
4.4 Ti6Al and Ti46Al single layers and 3D samples Experiment	98
4.4.1. Top surface analysis of the single layers	99
4.4.2. Cross-sectional analysis of the single layers	102
4.4.3. Analysis of the 3D sample.....	104
4.4.4. Hardness of Ti6Al DMLS 3D built part.....	108
4.4.4.1 Microhardness Tests	108
4.5 Summary.....	109
CHAPTER 5 – Conclusions and recommendations	110
5.1 Conclusions.....	110
5.2 Recommendations	110
References.....	111

LIST OF FIGURES

Figure 1. Specific strength versus operational temperature of selected structural materials compared with titanium alloys and aluminides (Donachie, 2000).	26
Figure 2. Titanium aluminide Binary phase diagram (McCullough <i>et al.</i> , 1988).	27
Figure 3. Nucleation and growth of α to form α/β equilibrium microstructure during a slow cooling process from above the β -transus temperature (Kelly, 2004)	28
Figure 4. Different Titanium aluminide microstructures obtained with different heat treatments	29
Figure 5. Crystal structure and possible slip planes and slip vectors in Ti_3Al Froes <i>et al.</i> , (1992)	31
Figure 6. A γ -TiAl LPT blade and microstructure details, B TiAl turbocharger wheel produced by EBM; C cross section of a hollow TiAl turbocharger wheel (Baudana <i>et al.</i> , 2016).	33
Figure 7. Material mix in advanced turbofan engine (Bradley, 1989)	34
Figure 8. Metal AM categories (Lewandowski & Seifi, 2016)	37
Figure 9. Schematic illustration of the laser-based powder bed fusion process (Sun <i>et al.</i> , 2017).	38
Figure 10. The DMLS EOSINT M280 machine used in the experiments	40
Figure 11. Pelvic implant of a 15 year old cancer patient (EOS GmbH, 2016) (A) and a maxilla implant produced by DMLS in CRPM at Central University of Technology (B).	40
Figure 12. Illustration of the DMLS process (Meiners & Breme, 2012).	41
Figure 13. Major powder characterization parameters for AM (Benson & Snyders, 2015).	45
Figure 14. Geometrical characteristics of a single DMLS track (Yadroitsev, 2009)..	49
Figure 15. Laser radiation transfer in a powder layer on a substrate: Q_0 incident power density, z powder depth, L layer thickness, θ radiation propagation angle, and $I(z,\theta)$ radiation intensity (Gusarov <i>et al.</i> , 2009).	50
Figure 16. Instability of laser sintered tracks from stainless steel grade 316L ($-25 \mu m$) powder on (Yadroitsev, 2009)	51

Figure 17. The effect of scanning speed on the relative density for AISI 316L stainless steel processed on a Concept Laser M3 machine (Thijs *et al.*, 2010) 52

Figure 18. Top view of a laser sintered track (Yadroitsev *et al.*, 2015)..... 53

Figure 19. (a) Top view of single layer produced by one-zone strategy (b) and two-zone strategy (Yadroitsev *et al.*, 2015)..... 54

Figure 20. Schematic of the island scan strategy (Qiu, 2013) 54

Figure 21. . Different scan patterns a) one direction b) double scanning each layer c) alternating scanning d) the direction of scanning rotated through a certain angle between consecutive layers (Yadroitsev *et al.*, 2015). 55

Figure 22. Bending stresses within the specimens (Kruth *et al.*, 2004)..... 56

Figure 23. Algorithm for optimal DMLS process parameters (Yadroitsev *et al.*, 2015). 58

Figure 24. Schematic of research methodology for the study 61

Figure 25. Particle size distributions for employed CP Ti powder. 62

Figure 26. Sieving of the powder manually 64

Figure 27. The substrate prepared and levelled onto the elevating system 65

Figure 28. Top view of the substrate with single tracks and single layers 66

Figure 29. Optical microscope (ZEISS Axio Scope.A1)..... 66

Figure 30. Struers CitoPress-1 (a) and polishing machine Struers Tegramin-25 (b).67

Figure 31. Lab Companion UC-02 Ultrasonic cleaner (a) and ESCO Ductless fume hood (b)..... 68

Figure 32. Cross-section of the single track. 69

Figure 33. The JEOL JSM-7800F SEM used in the study..... 69

Figure 34. (A) FM-700 Digital Vickers microhardness tester (B) Indenter for Vickers hardness test..... 70

Figure 35. Surftest SJ-210 portable surface roughness tester. 71

Figure 36. The design of the experiment..... 73

Figure 37. Top surface optical micrographs of Ti6Al single tracks (a) Continuous track at 150 W and 1.2 m/s (b) Irregular track at 350 W and 2.4 m/s and (c) Balling track at 350 W and 3.4 m/s 75

Figure 38. Process map for Ti6Al single tracks 76

Figure 39 . Droplets next to a single track of Ti6Al and satellites on the track surface 77

Figure 40. The width of the Ti6Al single tracks at different scanning speeds and laser power.	78
Figure 41. Linear energy density of Ti6Al single tracks at different scanning speeds and laser power.....	79
Figure 42. Cross-sectional views of the level of penetration into the substrate of the Ti6Al laser sintered single tracks.....	80
Figure 43. Re-melted depth of Ti6Al single tracks at different scanning speeds and laser power.....	82
Figure 44 Cross sectional profiles of the Ti6Al single tracks with poor penetration (a) 150W at 2.2m/s (b) 350W at 1.8m/s (c) 350W at 2.6m/s.....	82
Figure 45. Cross sectional profiles of Ti6Al single tracks with deep penetration (V-shape) profiles (a) 150W at 0.4m/s (b) 150W at 0.8m/s (c) 350W at 1m/s.....	83
Figure 46. Cross sectional profiles of Ti6Al single tracks with humping and undercutting (a) 150W at 1.4m/s (b) 150W at 1.6m/s (c) 150W at 1.8m/s.....	84
Figure 47. Cross-sectional profile of a Ti6Al single track, formed at optimal process parameters of 150 W at 1.2 m/s, with a U-shape profile.....	84
Figure 48. Optical micrographs of the top surfaces of Ti6Al single layers at 150 W and 1.2 m/s at hatch distances 80 μm , 90 μm and 100 μm	85
Figure 49. SEM secondary electron micrographs of Ti6Al samples at different hatch distances for single scanned and rescanned layers built at 150 W and 1.2 m/s.	86
Figure 50. Optical micrographs of cross-sectional views of Ti6Al built at 150 W laser power and 1.2 m/s scanning speed for single and re-scan at hatch distances 80 μm , 90 μm and 100 μm	87
Figure 51. EDS Al elemental mapping of single scanned and rescanned areas on the cross-sections of the Ti6Al samples built at different hatch distances and at 150 W laser power and 1.2 m/s scanning speed.	87
Figure 52 Top surface optical micrographs of Ti46Al single tracks (A) 150W at 0.4m/s (B) 150W at 0.8m/s (B) 150W at 2m/s (D) 350W at 1m/s (E) 350W at 2m/s (F) 350W at 3.4m/s.....	89
Figure 53. Process map for Ti46Al single tracks produced at laser powers from 150 W to 350 W with varied scanning speeds (0.4–3.4 m/s).....	90
Figure 54. The width of the Ti46Al single tracks at different scanning speeds and laser power.....	90

Figure 55. Linear energy density of the Ti46Al single tracks <i>versus</i> scanning speed	91
Figure 56. Cross-sectional view of single laser tracks at a laser power of 150 W (A) 0.6m/s (B) 2m/s (C) 2.2m/s	91
Figure 57. Cross-sectional view of single tracks at a laser power of 350 W (A) 1m/s (B) 1.2 m/s (C) 2.6m/s.....	92
Figure 58. Cross-sectional view of single laser tracks at a laser power of 350 W (A) 2.8m/s (B) 3m/s (C) 3.4m/s	92
Figure 59. Remelted depth of Ti46Al single tracks versus scanning speed and laser power	93
Figure 60. Top view of Ti46Al single tracks (A) 150W 0.08m/s (B) 150W 0.1m/s (C) 170W 0.1m/s	93
Figure 61. Top view of Ti46Al single tracks (A) 170W 0.2m/s (B) 170W 0.4m/s (C) 170W 0.7m/s	94
Figure 62. Top view of Ti46Al single tracks (A) 150W 0.12m/s (B) 150W 0.18m/s (C) 150W 0.26m/s	94
Figure 63. Top view of Ti46Al single tracks (A) 100W 0.4m/s (B) 100W 1.8m/s (C) 100W 2.2m/s	94
Figure 64. Top view of Ti46Al single tracks (A) 50W 0.08m/s (B) 50W 0.18m/s (C) 50W 0.4m/s	95
Figure 65. Process map for Ti46Al single tracks produced at laser powers from 50W, 100W, 150 W and 170 W with varied scanning speeds	95
Figure 66. Width of Ti46Al single tracks versus the scanning speed	96
Figure 67. Cross-sectional view of Ti46Al single tracks at a laser power of 170 W (A) 0.1m/s (B) 0.2m/s (C) 1m/s	97
Figure 68 Cross-sectional view of single laser tracks at a laser power of 150 W (a) 0.08m/s (b) 0.1m/s (c) 0.4m/s	97
Figure 69 Cross-sectional view of Ti46Al single laser tracks at a laser power of 100 W (a) 0.6m/s (b) 1.2m/s (c) 2.2 m/s.....	98
Figure 70. Cross-sectional view of single laser tracks at a laser power of 50 W (a) 0.14m/s (b) 0.18m/s (c) 0.4 m/s	98
Figure 71. Single layers and 3D samples (A) Ti6Al (B) Ti46Al.....	98
Figure 72. Optical micrographs of the top surfaces of Ti6Al at 150W and 1.2m/s....	99
Figure 73. Optical micrographs of the top surfaces of Ti46Al at 170W and 0.1m/s	100

Figure 74. Surface roughness R_a of Ti6Al and Ti46Al at varied hatch distance, laser power and scanning speeds..... 101

Figure 75. Surface roughness R_z of Ti6Al and Ti46Al at varied hatch distance, laser power and scanning speeds..... 101

Figure 76. Optical micrographs of the cross-sections of single layers of Ti6Al at 150W and 1.2m/s at different hatch distance, on a single and re-scan method 102

Figure 77. Cross-sections of single layers of Ti46Al at 170W and 0.1m/s at different hatch distances, on a single and re-scan method 103

Figure 78. EDS analysis results for Ti6Al 103

Figure 79. Point analyses of the (a) Ti46Al (b) Ti5Al single layers in the SEM..... 104

Figure 80. Cubes of (a) Ti6Al at 150W 1.2m/s (b) Ti46Al at 170W 0.1m/s..... 104

Figure 81. The DMSL scanning co-ordination system..... 105

Figure 82. Optical microscope pictures of Ti6Al 3D part (a) Top view (b) Side view (c) Front view..... 106

Figure 83. SEI and BEC SEM micrographs of the Ti6Al..... 106

Figure 84. Optical microscope pictures of Ti6Al 3D part (a) Top view (b) Side view (c) Front view un-etched..... 107

Figure 85. EDS Al elemental mapping of Ti6Al 3D part views (a) Top (b) Side (c) Front..... 107

Figure 86. Vickers microhardness of different surfaces of the Ti6Al 3D part..... 108

LIST OF TABLES

Table 1. Comparison of Titanium Aluminides with Titanium and Ni-Superalloys (Chesnutt, 1992)	25
Table 2. Possible Aircraft engine mix in 2010 (Bradley, 1989)	34
Table 3. Typical physical and mechanical properties of pure Ti (grade 2) (ASM aerospace, 2016)	46
Table 4. Physical and mechanical properties of Aluminium (ASM aerospace, 2016)	46
Table 5. Chemical composition of CP Ti powder in weight %	62
Table 6. The polishing procedure recommended by Struers and adopted for the studies	67
Table 7. Experimental process parameters of the Ti46Al Run 1.	71
Table 8. Design of experiment process parameters of the Ti46Al 2 nd t run.	72
Table 9. Material properties of Ti and Al	88
Table 10. Micro-hardness values of Ti6Al 3D part	108

ABBREVIATIONS & NOMENCLATURE

AM	Additive Manufacturing
ASTM	American Society for Testing and Material
CRPM	Centre for Rapid Prototyping and Manufacturing
CSIR	Council for Scientific and Industrial Research
CUT	Central University of Technology, Free State
DMLS	Direct Metal Laser Sintering
EOS	Electro Optical Systems GmbH
SEM	Scanning electron microscopy
SLM	Selective laser melting
ρ	Density
h	Layer thickness
P	Laser power
V	laser scanning speed

CHAPTER 1 INTRODUCTION

1.1 Background

In this modern era of technological advancement and industrialization, the manufacturing industry has seen tremendous transformation in terms of its production processes. The dynamics in the market, which is being attributed to the customers changing demands for excellent products, have compelled the manufacturing industry to adopt technology as a strategic element to enhance their productivity. One of the cutting edge technologies that is bound to influence today's manufacturing paradigm is additive manufacturing (AM), also known as 3D printing or rapid prototyping, which is one of the key technologies of the emerging fourth industrial revolution (Industry 4.0). Industry 4.0 is the recent movement on intelligent automation technology, which is focused on the integration of intelligent production systems and advanced information technologies. Digitization and intelligentization of the manufacturing process is the need for today's industry. AM is considered an essential ingredient in this new movement. Due to the necessity for mass customization in Industry 4.0, non-traditional manufacturing methods are a necessity (Dilberoglu *et al.*, 2007).

Additive manufacturing (AM) is a process of joining materials to make objects from 3D model data, usually layer upon layer, as opposed to subtractive manufacturing methodologies. AM builds components from different range of metals, plastics and ceramics. These materials are made available in powder form, liquid form, sheets, filaments or ribbons. AM is used in various industries such as aerospace, biomedical, and automotive manufacturing. Therefore, AM is a key technology for fabricating customized products due to its benefits in cases where conventional manufacturing has limitations, because it allows highly complex components to be made (Fraunhofer Institute, 2016).

Over the years, the application of AM has shifted from a rapid prototyping technology to a manufacturing technology for production of final parts. AM will probably never fully replace conventional manufacturing technologies, but is growing as a mature manufacturing technology in sectors and applications where the advantages of the technology outweigh conventional manufacturing technology, as the production

technology of choice. AM has received the largest interest as a manufacturing technology in applications where part complexity would increase performance requirements, weight reduction strategies and mass customisation of parts.

Titanium is the ninth most abundant element in the earth's crust and the fourth most abundant metal (Donachie, 2000). Because of the abundance of the metal and the benefits of the flexibility of AM, titanium metal powder development and application becomes a significant aspect of research with potential impact on the growth of the titanium industry in the world. Titanium aluminide is considered a key material for high performance gas turbines for aircraft engines, manufacturing of engine valves and a variety of automotive applications. Titanium aluminide alloys are gaining approval in other markets such as architecture, sports and leisure, chemical processing and transportation, due to the outstanding thermo-physical properties of Titanium aluminide alloys (. Liu *et al.*, 1996; Austin, 1999; Dimiduk, 1999; Tetsui *et al.*, 2005).

The replacement of Ni-based superalloy parts with Titanium aluminide -based alloys could reduce the structural weight of high-performance gas turbine engines by 20–30%, which would enhance engine performance and fuel efficiency (Voice *et al.*, 2005). However, the conventional methods of manufacturing the Titanium aluminides lead to the production of parts with metallurgical defects such as porosity, shrinkage, poor room-temperature mechanical properties, and inhomogeneous microstructure. To avoid the afore-mentioned drawbacks parts with simple shapes and moderate dimensions have in the past been produced from Titanium aluminide alloys.

To satisfy the industrial requirements of producing geometrical, technical and functional properties of components of complex shapes and uniform microstructure, an alternative processing route(s) that satisfies the industrial requirements needs to be exploited (Thomas *et al.*, 2016). The unique manufacturing capabilities of AM technology such as direct metal laser sintering (DMLS) could be used to produce Titanium aluminide parts with the desired properties for high value engineering applications at elevated temperatures.

1.2. Problem Statement

Titanium aluminide based alloys represent an important class of high-temperature structural materials providing a unique set of physical and mechanical properties that can lead to substantial payoffs in aircraft engines, industrial gas turbines, and automotive parts. Their technological maturity has been proven due to the significant advances in understanding of the relationships between composition, processing, microstructural characteristics, and properties.

However, the inherent limitations of the conventional method of manufacturing near net shapes have limited the widespread adoption of the Titanium aluminide alloy as a structural material for high-temperature engineering applications. In order to harness the full potential of the alloy there is a need to adopt a technology that is capable of producing 3D objects with intricate geometrical characteristics. This makes additive manufacturing technology, such as DMLS, the preferred choice.

Commercially pure Ti has been successfully blended with Al using conventional powder metallurgy processes and in additive manufacturing processes, such as laser solid forming (LSF) and in laser engineered net-shaping. However, the use of blended elemental powder in powder bed fusion (PBF) processes for metal additive manufacturing (MAM) of Titanium aluminide alloy parts has, to the knowledge of the author, not been demonstrated yet. The use of blended elemental powder instead of pre-alloyed powder is a cost effective option as it eliminates the pre-alloying step in the process, which includes melting or mechanically alloying powder blends in a high-energy ball mill to produce a homogeneous powder metal alloy.

1.3. Aim of the project

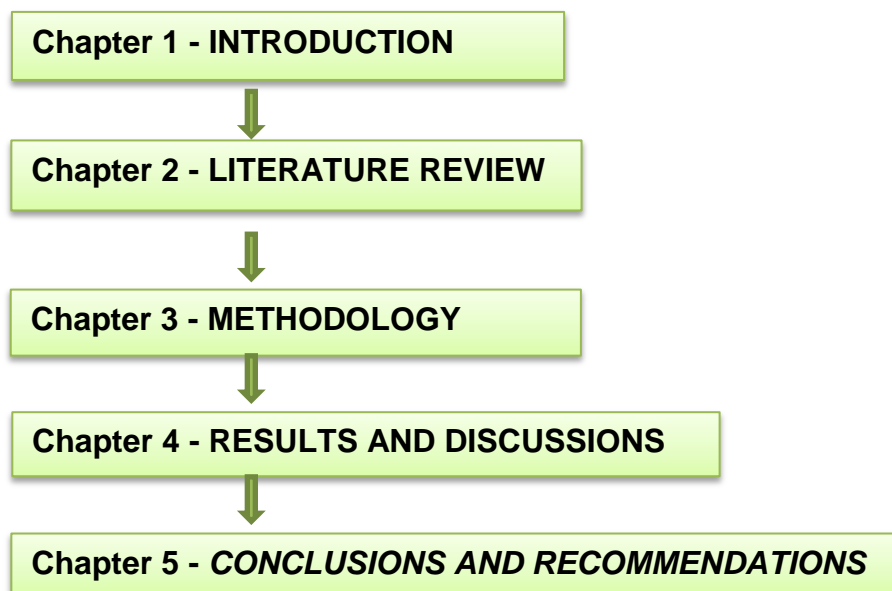
The aim of this study is to determine the feasibility of using blended elemental (BE) Ti and Al powder mixtures in a DMLS system, to make parts that have comparable or better geometric, functional and microstructural properties to that of the conventional processed titanium aluminide alloy.

1.4. Objectives

The objectives are:

- To determine the optimum process parameters that could be used to manufacture Ti6Al and Ti46Al from BE powders through the DMLS process using the EOSINT M280 machine.
- To produce dense 3D Ti6Al and Ti46Al DMLS samples using the EOSINT M280 machine
- To study the microstructure and hardness of Ti6Al and Ti46Al samples manufactured from BE powders through the DMLS process using the EOSINT M280 machine.

1.5. An overview of the dissertation



CHAPTER 2- LITERATURE REVIEW

2.1 Titanium and Titanium alloys

2.1.1 Introduction

Titanium was discovered in 1791, by a British reverend, mineralogist and chemist William Gregor. He discovered titanium by examining the magnetic sand from a local river and isolated “black sand”, now known as “ilmenite”. By removing the iron with a magnet and treating the sand with hydrochloric acid he produced the impure oxide of a new element and named it “mechanite”. Four years later, a Berlin chemist named Martin Heinrich Klaproth independently isolated titanium oxide from a Hungarian mineral, known as “rutile”. Greek mythology renamed it after the the children of Uranos and Gaia, the titans. The titans were utterly hated by their father and so detained in captivity by him in the earth’s crust, similar to the hard to extract ore, hence he named it Titanium (Titanium historical information, 2019)

More than 100 years later; Matthew Albert Hunter from Rensselaer Polytechnic Institute in Troy, New York was able to isolate the metal in 1910 by heating titanium tetrachloride ($TiCl_4$) with sodium. Eventually, Wilhelm Justin Kroll from Luxembourg was recognized as the father of the titanium industry. In 1932 he produced significant quantities of titanium by combining $TiCl_4$ with calcium. He fled to the United States at the beginning of World War II, and at the U.S.Bureau of Mines, he demonstrated that titanium could be extracted commercially by changing the reducing agent of $TiCl_4$ from calcium to magnesium. This process is now known as the “Kroll process” (Titanium historical information, 2019).

Titanium is ranked as the ninth most plentiful element and the fourth most abundant structural metal in the Earth’s crust. Titanium is found in low concentrations and it is found in an impure state, and therefore this makes it difficult and expensive to process. Titanium is classified as a nonferrous and light metal and it stands out primarily because of its high specific strength and corrosion resistance. At high temperatures, the specific strength of titanium alloys is particularly attractive at service temperatures 538 °C to 595 °C. However, the maximum application temperature is limited by the oxidation behaviour, whereby the Titanium metal

surface chemically reacts with oxygen and oxidises; causing corrosion of the metal surface. Titanium aluminides partly overcome the oxidation disadvantage; and because of this, they have become the subject of intense alloy development efforts (Donachie, 2000). Pure titanium crystallises at low temperatures in a hexagonal close packed structure (HCP), which is called the alpha titanium phase and at high temperatures it crystalizes to the body centred cubic structure (BCC), which is called the beta titanium phase (Donachie, 2000).

2.1.2 Titanium powder production

Powder Metallurgy (PM) processes can be used in production of components with complex geometry with little machining and low production costs using metal powders. The powder used in AM processing can be Pre-alloyed (PA) powder or Blended Elemental (BE) powder mixtures. In PA powder, each individual powder particle has the composition of the desired alloy composition of the final part and in the BE powder mixtures each individual powder particle has an elemental composition with the powder mixture as a whole representing the chemical specification of the alloy (Simonelli *et al.*, 2018).

Powder production plays an important role in AM processing and exploring economical ways of producing powder is vital. The PA powders have a high cost due to the chain of processes involved in the production of these powders. The required alloy composition is first obtained through the conventional production route in the form of a solid metal, which is then processed back into powder through another additional gas atomization process, which adds further cost to the production process. Instead of using the conventional PA powders in AM, BE powdermixtures can be used to lower the cost of the feedstock material (Simonelli *et al.*, 2018).

2.1.3 Titanium Alloying

Alloying is a common process when it comes to the use of metals in commercial applications. One or more elements are commonly alloyed with the base metal to modify its characteristics to meet the desired properties for a specific application. Some significant benefits offered by titanium alloys form the basis for the widespread use of titanium today (Donachie, 2000).

These are:

- Titanium has a lower density (40% less) than that of steel and nickel-based super alloys.
- Titanium has good tensile strength, better than that of austenitic or ferritic stainless steel.
- Titanium alloys are useful at temperatures to about 538 °C to 595 °C, dependent on composition. Titanium aluminides can retain strength to 750 °C.
- The cost of titanium alloys is comparable to that of super alloys.
- Titanium is corrosion resistant.
- Titanium is easy to fuse and bond; it can be joined through welding, brazing, adhesives, diffusion bonding, and fasteners.
- Titanium is formable and machinable

2.1.4 Effects of Alloying Elements in Ti Alloys

Alloying elements can be classified as alpha stabilizers or beta stabilizers. Alpha stabilizers such as oxygen, aluminium and nitrogen increase the temperature at which the alpha phase is stable. Beta stabilizers such as vanadium and molybdenum stabilize the beta phase at lower temperatures (Donachie, 2015). The beta transus is defined as the lowest equilibrium temperature at which the metal consists of 100% beta phase. The beta transus is critical in deformation processing and in heat treatment. The transformation temperature is strongly influenced by the following (Donachie, 2015):

- Interstitial elements, which are mainly alpha stabilizers (oxygen, nitrogen, and carbon).
- Hydrogen, which is a beta stabilizer.
- Metallic impurities and alloying elements. They can both either raise or lower the transformation temperature

2.1.5 Classes of Titanium alloys

There are four generally accepted classes of titanium alloys:

A. Alpha alloys (α)

These are single-phase alloys. They exist as solid solutions that are strengthened by adding alpha phase stabilizers and neutral alloying elements. Alpha alloys have good stability and have good high temperature properties. The disadvantage of alpha alloys is that they are not responsive to heat treatment for modification of the microstructural properties (Vydehi, 2006).

B. Near – Alpha alloys

Near-alpha alloys are formed by adding 1 to 2% of beta stabilizers to alpha alloys to improve the strength and workability. Near alpha alloys are a good compromise between the higher strength of alpha plus beta alloys and the creep resistance of alpha alloys. Near-alpha alloys are the most widely used commercial high-temperature Ti alloys. Aero-engine applications belong to this class. They are primarily alpha alloys containing some amount of retained beta in the final microstructure (Vydehi, 2006).

C. Beta alloys (β)

Beta alloys are formed by adding large amounts of beta stabilizers, up to 30% to the alloy. This causes the microstructure to retain the beta structure as a stable phase at room temperature. Beta alloys are commonly used for highly specialized burn-resistant and corrosion-resistant applications. Beta alloys have better formability compared to alpha alloys and they have high densities and poor ductility (Vydehi, 2006).

D. Alpha-Beta alloys

These alloys contain about 4 to 6% of beta stabilizers. Ti-6Al-4V, the most widely used titanium alloy, belongs to this class (Vydehi, 2006).

2.2 Titanium aluminides

2.2.1 Introduction

Titanium aluminide alloys are classified as ordered intermetallic compounds, which means they form when atoms of two or more metals combine in a fixed ratio to produce a crystalline material different in structure from the individual metals.

For titanium aluminides, the two metals are titanium (with a body-centred-cubic crystal structure) and aluminium (face-centred-cubic structure) (Kear, 1970). These materials have a similar or lower density and higher Young's modulus than conventional titanium alloys. The density of titanium aluminides is between 3.9 and 4.3 g cm⁻³ as opposed to 4.4 to 4.8 g cm⁻³ for titanium alloys and the Young's modulus of titanium aluminides is 145–175 GPa versus 90–120 GPa for titanium alloys. Titanium aluminides also have higher oxidation resistance and strength retention at high temperature, which makes them better suited for use in gas turbine engines and rocket propulsion systems. Several types of titanium aluminide alloys retain strength to 750 °C, which is at least 150 °C higher than the operating temperature limit of conventional titanium alloys.

Titanium aluminides have a small number of slip systems in their crystal structure, which limits the movement of dislocations at high temperature, thereby retaining their strength and providing one of the advantages of using titanium aluminide as a structural material. The ordered structure results in good strength and stiffness properties at elevated temperatures, because the long-range ordered super lattice structure reduces dislocation mobility and diffusion processes at elevated temperatures. (Stoloff & Davies, 1960; Kear, 1970).

Titanium aluminides can be classified into three major intermetallic compounds: gamma Titanium aluminide, alpha 2-Ti₃Al and TiAl₃. Ti₃Al is called α₂-aluminide (Alpha-2) and forms when the aluminium content of the alloy is above 6 at. % (i.e Ti–25Al–5Nb, Ti–24Al–11Nb). The Titanium aluminide compound is known as γ-aluminide (Gamma), and is formed when there are approximately equal amounts of Ti and Al (i.e Ti–48Al–1 V, Ti–48Al–2Mn). Vanadium (V) is a Beta-phase stabilizer. Niobium (Nb) is added to produce Ti₂Nb precipitates, which contribute to strength retention at high temperature and increased ductility at room temperature.

The Titanium aluminide α₂-alloy has superior specific strength compared with the Titanium aluminide near-alpha alloys up to 800 °C, and therefore Ti₃Al could be used as a lightweight replacement for conventional titanium alloys in jet engines. The γ-aluminide has a lower specific yield strength than the Titanium aluminide near-alpha alloys, but is able to retain its strength to higher temperatures (Chesnutt, 1992).

A comparison of titanium aluminide alloys with conventional titanium-base and nickel-base alloys is shown in Table 1.

Table 1. Comparison of Titanium Aluminides with Titanium and Ni-Superalloys (Chesnutt, 1992)

Property	Ti	Ti ₃ Al	Gamma	Nickel superalloys
Density, g cm ⁻³	4.54	4.84	4.04	8.3
Stiffness, GPa	110	145	176	207
Maximum Creep Temp, °C	540	730	900	1090
Maximum Oxidation Temp, °C	590	705	815	1090
Ductility - Operating Temp, %	15	5 - 12	5 - 12	10 - 20

The maximum operating temperature of γ -aluminides is similar to nickel super alloys used in the hottest sections of jet engines. Titanium aluminides have potential application in high-pressure compressor and turbine blades and γ -aluminides have less than one-half the density (3.9 g cm^{-3}) of nickel alloys ($8.7\text{--}8.9 \text{ g cm}^{-3}$) and therefore can be used as a lighter-weight engine material.

The outstanding high-temperature strength of titanium aluminides offers the possibility of increasing the maximum temperature limit of titanium-based alloys as well as being a lighter-weight substitute for nickel super-alloys in jet engines. However, titanium aluminides are susceptible to brittle fracture owing to their low ductility and poor fracture toughness, and this is a key factor limiting their use in aircraft engines. Typically, titanium aluminides have a room temperature ductility of 1–2% and a fracture toughness of about $15 \text{ MPa m}^{-0.5}$, which is lower than the ductility and toughness of conventional titanium alloys. Another problem is the high cost of processing engine components from titanium aluminides, being more expensive than for conventional titanium and nickel base alloys. Different ways to reduce the manufacturing costs and increase the ductility are being researched, so that titanium aluminides may eventually find increased use in jet engines.

Figure 1 shows that conventional titanium alloys are used up to temperatures slightly above 750K (477°C). Titanium aluminide based alloys compete with high temperature steels and Ni-base superalloys (Donachie, 2000).

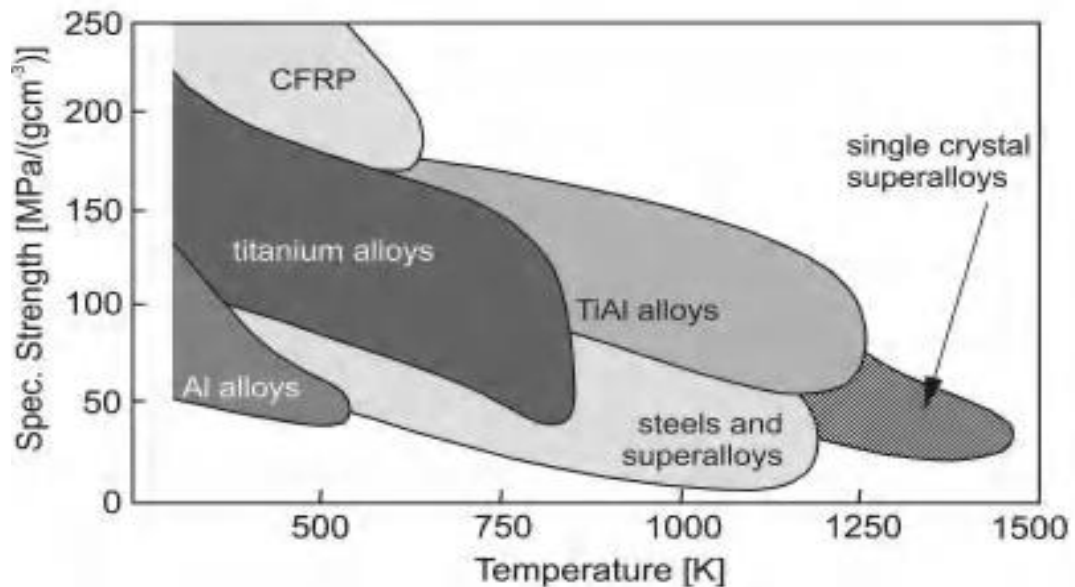


Figure 1. Specific strength versus operational temperature of selected structural materials compared with titanium alloys and aluminides (Donachie, 2000).

The titanium-aluminium binary system provides a model for solution strengthening. It is a model of the technical alpha and beta alloys. Titanium-aluminium alloys exist in either a hexagonal close-packed or body - centered cubic structure in the solid state. Figure 2 shows a comprehensive binary Ti-Al phase diagram, which includes Ti_3Al (α_2), TiAl (γ), $TiAl_2$, and $TiAl_3$ intermediate phases, and α -Ti, β -Ti and α -Al terminal solid solutions.

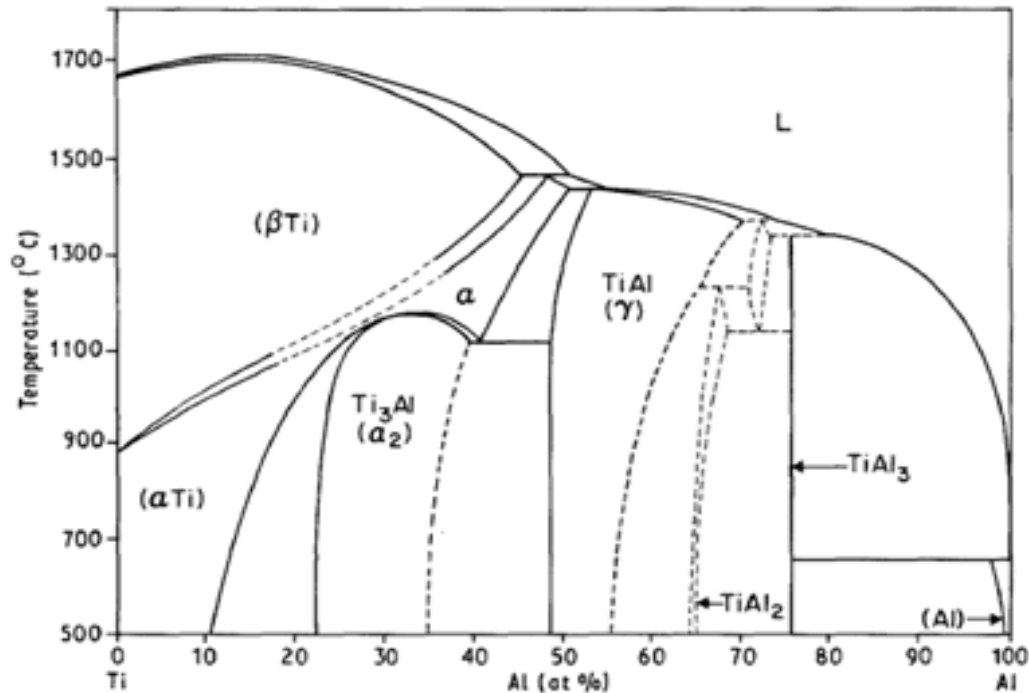


Figure 2. Titanium aluminide Binary phase diagram (McCullough *et al.*, 1988).

Ti50Al at. % alloy will solidify as cubic dendrites of β surrounded by γ formed according to the peritectic reaction $L + \alpha \sim \gamma$, or $L + \beta \sim \alpha$. At lower Al contents and at lower temperatures, the α phase forms from the β and γ phases by a peritectoid reaction, with subsequent α decomposition taking place eutectoidally to a lamellar ($\alpha + \gamma$) structure. Results from both ingot metallurgy and rapid solidification routes indicate that at about 50.at % of Al, the α phase forms directly from the liquid state according to the peritectic reaction $L + \beta \sim \alpha$ (McCullough *et al.*, 1988).

The Ti₃Al phase undergoes a disorder order transformation in the range of 22 to 39.at % Al and congruently at 1180°C. The ordered α phase has a hexagonal structure with

$a = 0.5782\text{nm}$ and $c = 0.4629\text{ nm}$. The TiAl (γ) phase, stable from 49 to 66.at % Al, is considered to be ordered up to the melting point. The antiphase boundaries were observed in rapidly solidified Ti60Al (wt. %) alloy. The γ phase has an ordered face-centred tetragonal structure with $a = 0.4005\text{ nm}$ and $c = 0.4070\text{ nm}$, and a tetragonality of 1.02 at the equiatomic position, which increases to 1.03 at higher Al contents (Haug & Siemers, 1989; Froes *et al.*, 1992).

2.2.2 The microstructure and deformation of titanium aluminides

Understanding the thermo-mechanical processing properties and the behaviour of the alloy is advantageous in manipulating the microstructure to yield the desired properties for a specific application. Titanium aluminide alloys can be heat treated to manipulate the microstructure to meet the desired properties for a specific application. They can be heat treated below and above the β -transus temperature (Donachie, 2000).

The cooling process that results in the transformation of a metal from one phase to another in α/β Ti alloys is shown in Figure 3.

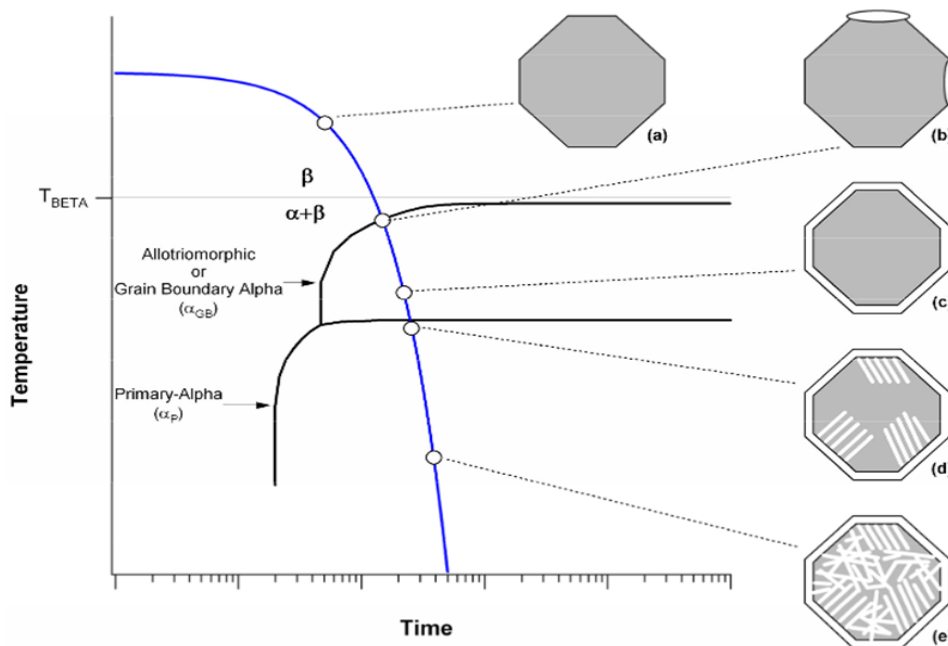


Figure 3. Nucleation and growth of α to form α/β equilibrium microstructure during a slow cooling process from above the β -transus temperature (Kelly, 2004)

Figure 3(a) shows a β -grain. A β -grain is formed when a $\alpha+\beta$ Ti-based alloy is heated above the β transus (T_β) temperature and a bcc structure is formed. Figure 3(b) shows two α grains growing from the boundary of the β -grain at temperatures below the β -transus.

Figure 3(c) shows α -phase all along the grain-boundary of the primary β -grain. Figure 3(d) shows lamellar colonies growing from the grain boundary towards the interior of the parent β -grain and figure 3(e) shows the growth and nucleation of further lamellae inside the parent β -grain during the cooling. The liquid solidifies from the β -phase (*bcc*) to the α -phase (*hcp*). The grain size and the morphology of the solid are determined by the nucleation rate, the thermal conditions at the time of solidification and the growth characteristics of the alloy. Heat treatment can alter the distribution, size and morphology of α -phase but has less effect on the prior β -grains (Sames *et al.*, 2016).

Titanium aluminide based alloys have different types of microstructures, depending on the heat treatment:

- (a) Fully lamellar
- (b) Nearly fully lamellar
- (c,d) Duplex
- (e) Near gamma and
- (d) Equiaxed

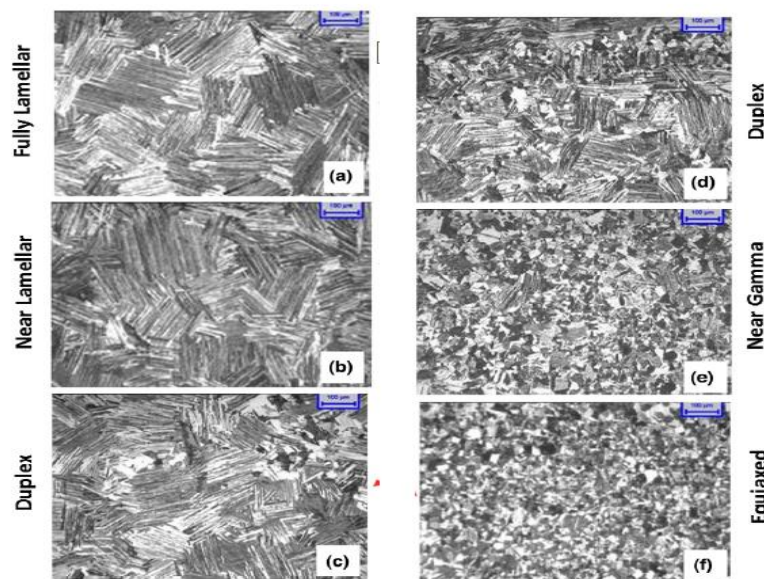


Figure 4. Different Titanium aluminide microstructures obtained with different heat treatments

Duplex microstructures are known for higher ductility, tensile strength and increased fatigue life resulting from a homogeneous microstructure and fine grains. By heat treating the material at a temperature above the α -transus a fully lamellar microstructure is obtained as shown in Figure 4(a).

Heat treating the alloy at a temperature below the transus temperature results in a near lamellar microstructure as shown in Figure 4 (b). If the annealing temperature is below the α -transus temperature, the amount of equiaxed grains increases and the microstructure transforms from a duplex to an equiaxed type with globular gamma grains only (c–f). A fully lamellar microstructure exhibits higher toughness and creep resistance (Kim & Dimiduk, 1991; Appel *et al.*, 2000).

The heat treatment of Titanium aluminide alloy is sensitive to changes, even minor changes in chemical composition causes a variation in the phase transformation temperatures, and so a complete rework of heat treatment has to be started all over again whenever the chemical composition is changed. For high temperature applications of these alloys, it is important to consider the oxidation behaviour of these alloys. At temperatures over 700°C, Titanium aluminide alloys reveal severe oxidation and form detrimental titanium oxides (Terner *et al.*, 2015).

Microstructural features of titanium aluminides can be varied by thermo-mechanical processing (TMP) and these features include β -grain morphology and distribution, primary α grain size and volume fraction, and secondary α_2 plate morphology and thickness. β processing generally results in elongated Widmanstätten α_2 in large primary β -grains, while α - β processing results in more equiaxed primary α grains. Both microstructure and mechanical properties follow the behaviour of more conventional titanium alloys, with the caveat that because of their ordered nature the Ti_3Al alloys are very brittle and fracture by a cleavage mechanism at ambient temperatures. Transformed β microstructures are considered the optimum microstructures because the structure makes it possible to achieve a good balance of room-temperature ductility and elevated temperature properties (Liu *et al.*, 1990; Froes *et al.*, 1992).

A small α_2 -grain size, allotropic change in the grain structure and growth of second-phase particles enhance strength by encouraging shorter slip lengths. The poor ductility behaviour of Ti_3Al alloys at low temperatures is attributed to the planarity of slip and the absence of slip in planes parallel to and/or inclined to the hexagonal axis (Blackburn *et al.*, 1978). Ti_3Al (α_2) has a DO_{19} ordered hexagonal structure as shown in Figure 5 A.

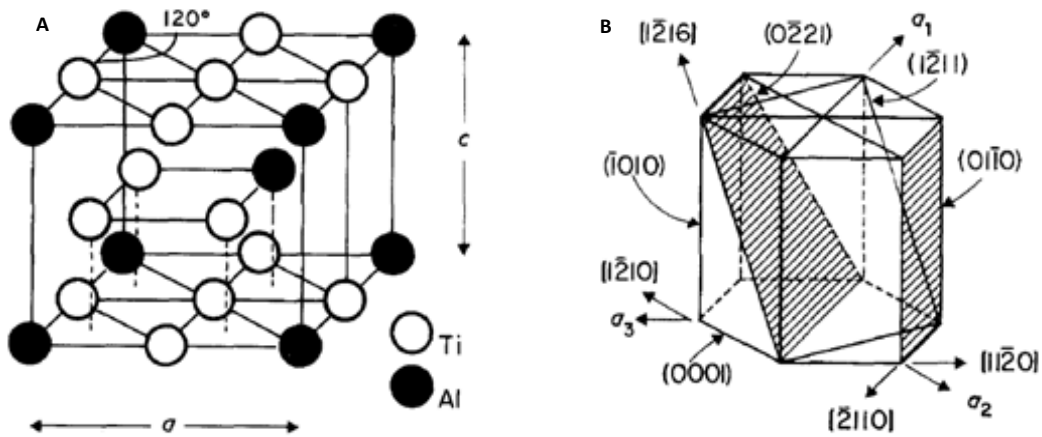


Figure 5. Crystal structure and possible slip planes and slip vectors in Ti_3Al Froes *et al.*, (1992)

The difference in the deformation behaviour of Ti_3Al and other hcp alloys and metals is due to the absence of twinning with preferred slip planes in Ti_3Al . Long-range order suppresses twinning in Ti_3Al because such deformation produces disorder. The possible slip planes and directions are shown in Figure 5 B.

There are three types of dislocations possible:

- $\langle a \rangle$ type moving on basal (0001) and pyramidal $\{2021\}$ planes;
- $\langle c \rangle$ type moving on second-order (1120) prism planes, and
- $\langle c + a \rangle$ type on $\{1121\}$ or $\{2021\}$ pyramidal planes

For Ti_3Al alloys, only $\langle a \rangle$ type dislocations are observed for deformation at room temperature and intermediate temperatures. The absence of $\langle c \rangle$ deformation at room temperature results in the generation of local stresses that cause poor ductility. (Lipsitt, 1985)

Ductility is improved by micro twinning and the presence of $\langle c \rangle$ and $\langle c + a \rangle$ type dislocations in samples at high temperature. It has been shown that $\langle c \rangle$ dislocations are present in under formed material whenever the α_2 phase has precipitated from the β phase; thus $\langle c \rangle$ dislocations are transformation-induced rather than deformation-induced products (Sastry, & Lipsitt, 1977).

The fracture behaviour in the Titanium aluminide alloys is related to the slip behaviour and the presence of the $\beta/B2$ -phase in the α_2 -phase. At room temperature and intermediate temperatures, fracture in Titanium aluminide alloys occurs by cleavage. Primary α_2 particles crack during a tensile test giving an effective drop in

load-bearing area. At higher temperatures, when the alloy exhibits ductility, intergranular cracking takes place instead of a complete ductile fracture thus accommodating strain across grain boundaries (Lipsitt, 1985).

The ductility is influenced by both the distribution fraction and the volume fraction of the α_2 phase and worsens at 30 to 35% α_2 . This behaviour is not the same in conventional titanium alloys where increasing the amount of equiaxed primary α improves ductility. When a good amount of equiaxed α_2 grains are produced by thermo-mechanical processing, room-temperature ductility can be improved, thereby reducing the inconsistency with the behaviour of conventional titanium alloys (Lipsitt, 1985).

Crack propagation in the α_2 phase happens easily, due to the difficulty of the $\langle c \rangle$ component slip. When a crack is initiated on the basal plane and activates co-planar $\langle a \rangle$ slip, large normal stresses near the crack tip are generated, which relax only when $\langle c + a \rangle$ slip is activated. If the $\langle c + a \rangle$ slip is not activated, the cracks continue to grow in the α_2 . The ability of the β phase to prevent cracks increases as the temperature increases and this explains the increased ductility at higher temperatures (Löfvander *et al.*, 1989).

2.2.3 Mechanical properties of Titanium aluminide-based alloys

Alloys based on the Titanium aluminide composition have higher elastic modulus, lower density and enhanced elevated temperature capabilities. However, they are known for poor room-temperature ductility and fracture resistance. At approximately 1000°C, the strength gradually decreases with increasing Al levels (Kim & Froes, 1990).

Tensile strength and hardness decreases with an increase in aluminium content (Kim, 1991). The tensile elongation reaches a maximum at a composition of approximately Ti-48Al at room temperature (Kim & Froes, 1990; Liu *et al.*, 1990). Low-cycle fatigue experiments suggest that fine grain sizes raise the fatigue life at temperatures below 800°C. Fatigue crack growth rates are more rapid than those for superalloys, even when density is normalized. Fracture toughness and impact

resistance are low at ambient temperatures, but fracture toughness increases with temperature. Fracture toughness increases with higher proportions of the lamellar structure. Increasing the volume fraction of the lamellar structure lowers ductility and enhances creep properties (Blackburn *et al.*,1984). Creep properties are improved beyond the behaviour of superalloys when normalized by density, but are strongly influenced by alloy chemistry and heat treatment (Kim, 1991).

2.2.4 Applications of Titanium aluminides

Titanium aluminides are used in automotive applications, in particular for the production of engine valves and turbine wheels for turbocharger and high performance gas turbines for aircraft engines; specifically the production of low-pressure turbine blades (see Figure 6).Titanium aluminide alloys are possible replacements of the Ni-based super alloy parts because of the reduced structural weight of Titanium aluminide components by 20–30% (Baudana *et al.*,2016).

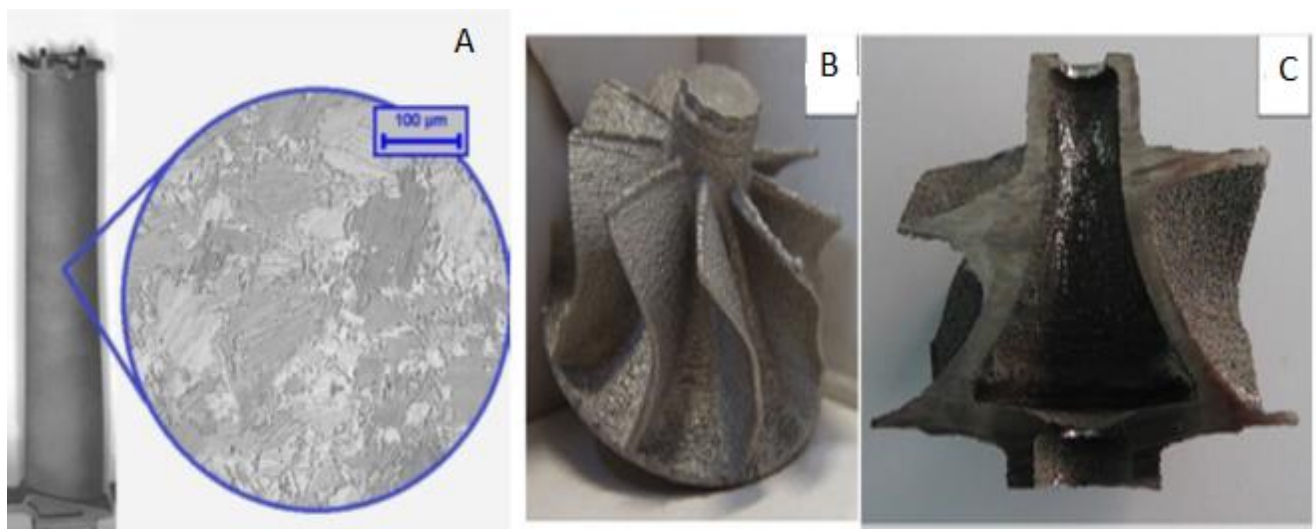


Figure 6. A γ -TiAl LPT blade and microstructure details, B TiAl turbocharger wheel produced by EBM; C cross section of a hollow TiAl turbocharger wheel (Baudana *et al.*,2016).

A prediction in 1989 of the possible materials mix in an aircraft engine is shown in Table 2 and in Figure 7

Table 2. Possible Aircraft engine mix in 2010 (Bradley, 1989)

Material	Percentage
Metal matrix composites	30
Ceramics (aluminides) and ceramic composites	30
Superalloys	13
Resin (Polymer) composites	10
Titanium	10
Steel	7
Aluminium	0
Magnesium	0

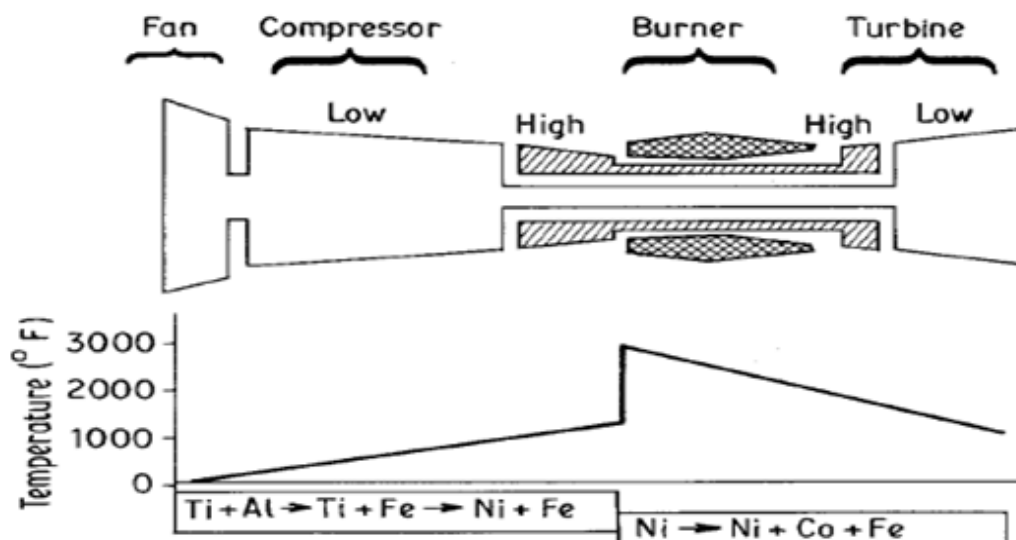


Figure 7. Material mix in advanced turbofan engine (Bradley, 1989)

Titanium aluminide based alloys have a strong potential to increase the thrust-to-weight ratio in the aircraft engine. This is especially the case with the low-pressure turbine blades and the high-pressure compressor blades of the engine. These were traditionally made from Ni-based superalloy, which is nearly twice as dense as Titanium aluminide based alloys.

Among the three major intermetallic compounds gamma Titanium aluminide has excellent mechanical properties and oxidation and corrosion resistance at elevated temperatures (over 600 °C), which makes it a possible replacement for traditional Ni based superalloy components in aircraft turbine engines. General

Electric currently uses gamma Titanium aluminide for the low-pressure turbine blades on its GENx engine, which powers the Boeing 787 and Boeing 747-8 aircraft. This was the first large-scale use of this material on a commercial jet engine when it entered service in 2011 (AviationPros, 2015)

2.3 Additive manufacturing (AM)

2.3.1 Introduction

AM is defined as “the process of joining materials to make objects from three-dimensional (3D) model data, usually layer upon layer, as opposed to subtractive manufacturing methodologies” (ASTM 52900, 2015).

AM is well known as 3D printing. AM makes 3D parts from a 3D model designed by computer-aided design (CAD) software. The computer software creates virtual cuts to the solid model in the form of cross sections thus generating a sequence of layers. The 3D printing machine then overlays the 2D layers layers onto each other and fuse them together until the entire 3D part has been formed (Fraunhofer Institute, 2003). AM builds components from different ranges of metals, plastics and ceramics. These materials are made available in powder form, liquid form, sheets, filaments or ribbons. AM is beneficial in cases where conventional manufacturing has limitations, because it allows highly complex components to be made. AM provides a high degree of design freedom whereby special features and details of components that would previously have been impossible and costly to build in conventional manufacturing, can now be made possible with AM (Fraunhofer Institute, 2003).

There are two main categories in metal AM namely; The Powder bed fusion (PBF) and the Directed energy deposition (DED). In Figure 8, these main categories are further broken down into different technologies. There are a number of the AM technologies as listed below; their functions depend on the type of heat source and method of deposition. Materials are melted at different combinations of absorbed power and beam velocity. There are seven standardised categories of additive manufacturing processes (ASTM52900, 2015: Lewandowski & Seifi, 2016).

1. VAT photo polymerisation – This process uses a vat of liquid photopolymer resin, out of which the model is constructed layer by layer.
2. Material jetting –This process, the material is jetted onto a build platform using a continuous stream or drop on demand approach.
3. Binder jetting – This process uses two materials; a powder based and a liquid binder. The printing head moves along the x and y axes of the machine and deposits alternating layers of the build material and the binding material.
4. Material extrusion – This process uses a technique where the material is drawn through a nozzle, where it is heated and deposited layer by layer.
5. Powder bed fusion (PBF) – This process uses the commonly used printing techniques such as; direct metal laser sintering (DMLS) and electron beam melting (EBM). The details of this technique are discussed further later.
6. Sheet lamination – This process uses techniques that use sheets and ribbons of material; the material is bound together using an adhesive. Ultrasonic additive manufacturing (UAM) and laminated object manufacturing (LOM) are examples of sheet lamination.
7. Directed energy deposition – This process uses techniques such as laser engineered net shaping (LENS), and is commonly used to repair and add material to existing components.

There are two main metal additive manufacturing categories namely; powder bed fusion (PBF) and the directed energy deposition (DED). In Figure 8, these main categories are further broken down into technologies offered by different machine suppliers.

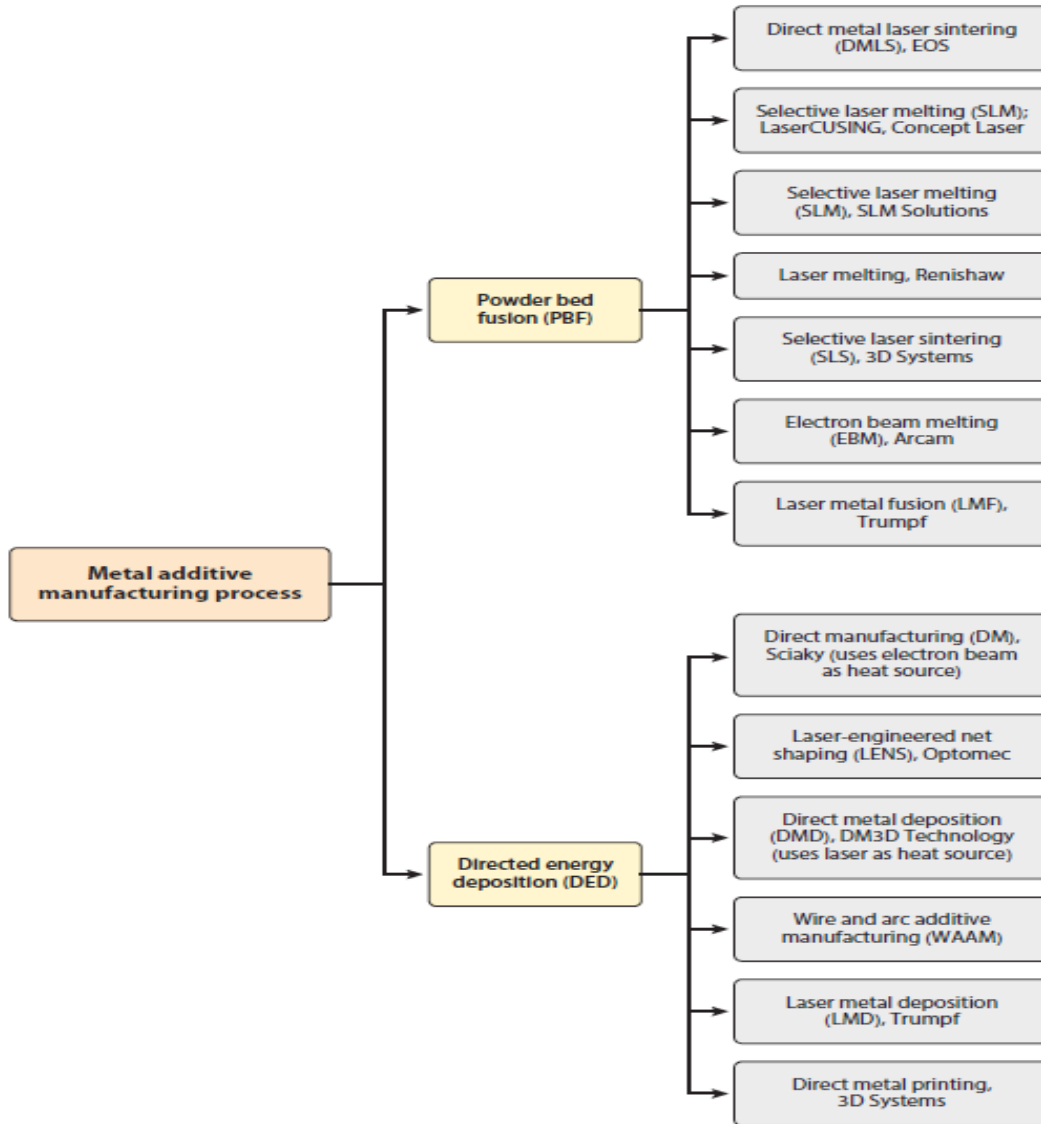


Figure 8. Metal AM categories (Lewandowski & Seifi, 2016)

2.3.2 Powder Bed Fusion

PBF is described as an additive manufacturing process in which thermal energy selectively fuses regions of a powder bed (ASTM 52900, 2015). The energy source for a PBF process is either an electron beam or a laser beam. It is programmed to deliver energy to the surface of the bed to melt or sinter the powder into the desired shape based on the information of the 2D slices of the CAD model.

In the case of laser PBF (L-PBF), a laser beam scans the selected locations of the powder bed at a controlled speed and fuses the powder particles together and onto the solid material underneath by either full melting in the case of metal using a selective laser melting (SLM) process or by partial melting in the case of polymers

using a selective laser sintering (SLS) process. After completing the fusion of a layer, the powder bed is lowered by a height equal to the powder layer thickness and then a new layer of powder is spread over the build platform. The laser again runs over the powder layer and fuses the powder; the process is repeated until a solid 3D component is completed (William & Frazier, 2014).

The path of the laser scanning in each layer is defined by the part geometry at the corresponding location along the Z-axis (the Z-axis is the building direction and is perpendicular to the plane of the build platform, the X-Y plane) and the selected scanning strategy. To prevent oxidation during the processing of the part, the building environment is protected with a flow of inert gas (argon, nitrogen). The inert gas flow also helps with the removal of condensate that is due to the melting of the powder and therefore a homogeneous flow of gas across the build has an important role in the quality and properties of parts built (Ferrar *et al.*, 2012).

Figure 9 shows an illustration of the powder bed fusion process.

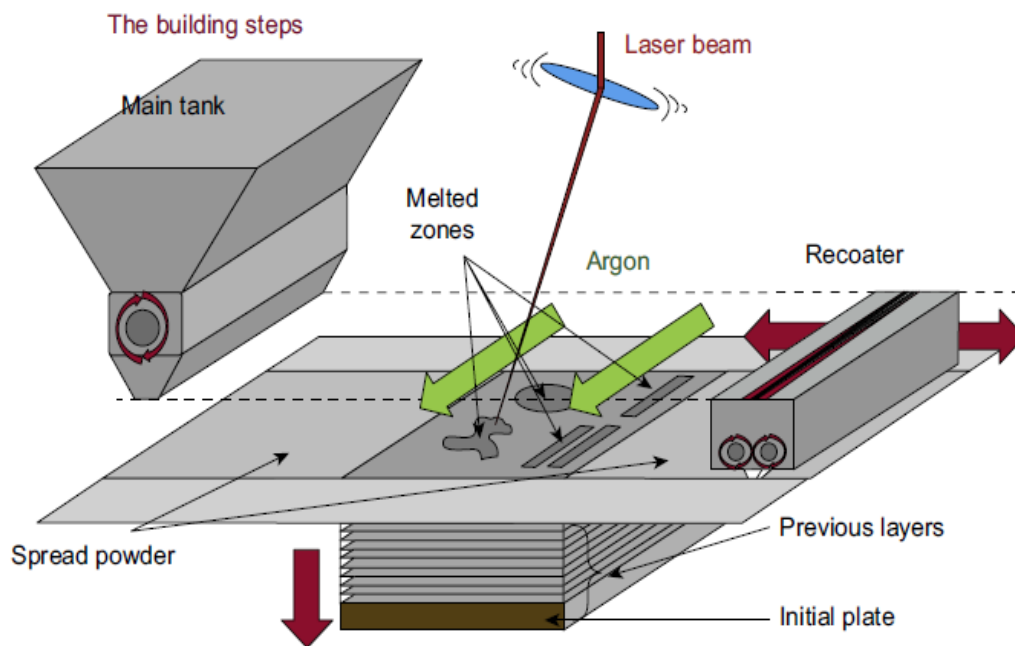


Figure 9. Schematic illustration of the laser-based powder bed fusion process (Sun *et al.*, 2017).

A homogeneous powder thickness in each layer must be maintained to control the quality of the part. Sufficient powder for building each layer can be supplied by dropping a controlled volume through a recoater or a hopper to a controlled height, or by spreading it from a powder dispensing container across the build platform. The

powder is spread uniformly over the build platform by a counter rotating roller, wiper or a doctor blade (Sun *et al.*, 2017).

Some of the processing parameters in the powder bed fusion process are: layer thickness (t), laser power (P), laser scanning speed (v) and scanning path strategy, hatching space (h) and laser spot size (d), particle size and distribution, platform pre-heating temperature and laser beam scanning strategy. Most metals can be processed using the powder bed fusion methods; however, all differ when it comes to processing windows and parameters. The differences in processing parameters are due to the differences in the metal chemical composition, heat absorption, surface tension and viscosity of the melt and thermal conductivity (Sun *et al.*, 2017).

2.3.3 Direct Metal Laser Sintering

Direct Metal Laser Sintering (DMLS) technology is a powder bed fusion technique. DMLS is a name used by the supplier Electro Optical Systems (EOS) GmbH to describe a laser-based AM process similar to that of selective laser melting (SLM), which is used for metallic powders only. In the DMLS process the laser beam scans over the surface of a powder layer previously deposited on a substrate to fuse powder particles together. The forming process proceeds along the scanning direction of the laser beam. Each layer of the part is filled with single tracks of molten powder (Yadroitsev, 2009).

Materials such as aluminium alloys, stainless steel, titanium alloys and more are used in this process. The DMLS technology can be used to manufacture a functional part that has similar properties as that obtained from bulk materials. DMLS allows for multiple components such as fasteners and mountings to be made at once and this reduces waste of time and resources. Figure 10 shows an EOS DMLS machine.



Figure 10. The DMLS EOSINT M280 machine used in the experiments

DMLS has already had a positive impact on manufacturing industries such as aerospace, medical implants and devices, automotive, sports equipment, marine applications and more. Complex parts, small and light components with complex geometric features such as hollows, thin walls and undercuts, are now possible to be made with SLM (Yadroitsev, 2009). In figure 11A, a pelvic implant of a 15-year-old cancer patient that was made through the DMLS process and a maxilla implant produced by the CRPM are shown figure 11B.

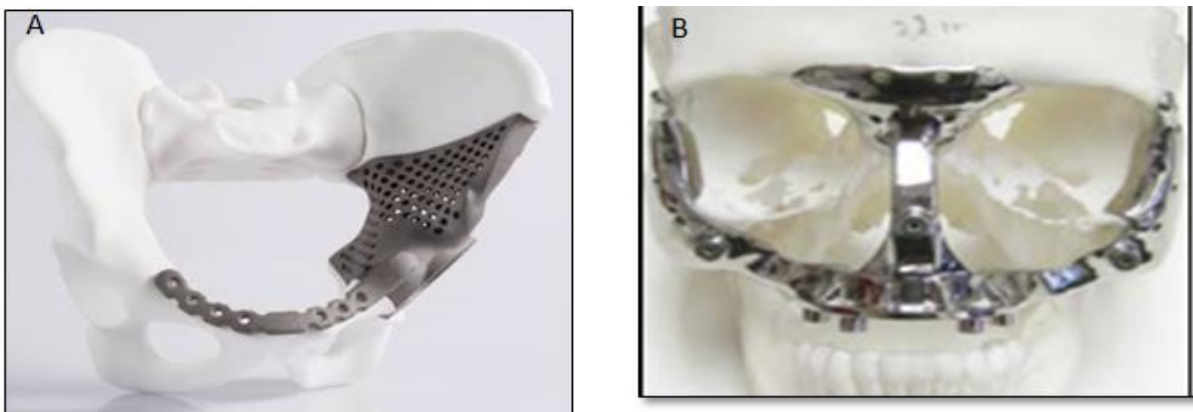


Figure 11. Pelvic implant of a 15 year old cancer patient (EOS GmbH, 2016) (A) and a maxilla implant produced by DMLS in CRPM at Central University of Technology (B).

The DMLS process is shown schematically in Figure 12. The DMLS process starts by drafting the desired component in a 3DCAD file. Subsequently, the 3D CAD model is sliced into 2D layers (Spierings *et al.*, 2011)

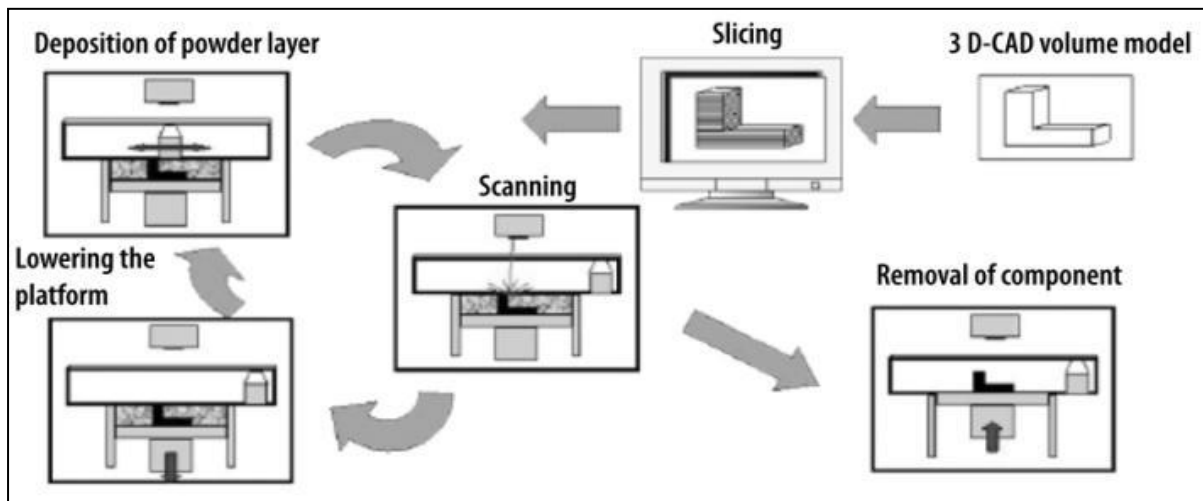


Figure 12. Illustration of the DMLS process (Meiners & Breme, 2012).

A substrate is placed on the platform of the DMLS machine and a thin layer of powder is applied on top of the substrate from the dispensing container by a wiper blade. The laser then scans across the powder layer and it fuses the powder at the exact points identified by the CAD file on the computer for that specific layer. The substrate is lowered once the layer is solidified and the next layer is built on top of, and fused to, the previous layer. This process is repeated until the last layer of the component is completed. The platform is moved up to lift the three-dimensional part out of the powder bed. Once the part is out, the excess powder is brushed off into the used powder container (Yadroitsev, 2009).

The substrate with the part still attached to it is heat treated to relieve residual stresses. Subsequently, the supports on angled sections or overhangs and other areas that attach the part to the substrate are broken off or machined off. Some surfaces of the part can be machined to improve the surface finish.

Characteristics of the produced DMLS object such as porosity, microstructure and mechanical properties are influenced by the parameters selected for the DMLS process. Parameters such as layer thickness, as well as powder particle size and shape, are important for deposition of a uniform powder layer.

Laser power, temperature, spot size, scanning speed of the laser and the deposition time, determine the effectiveness and success of the process and the quality of the part produced. The DMLS parameters can be categorised into three different sections (Yadroitsev, 2009).

Categories of machine based input parameters:

- Laser: Wavelength, spot size, power density and beam profile;
- Atmosphere: airflow, ionising energy;
- Substrate: roughness, chemical composition and temperature.

A DMLS machine has three main areas of interest when considering machine based input parameters: the laser or heat source, the atmosphere in which the process takes place and the substrate or base on which the objects are manufactured. Absorption of the energy from the laser beam causes the powder particles to melt. These molten particles form the molten pool. The wavelength directly affects the percentage radiation absorbed, which depends on the specific material. Laser spot size, mode and beam intensity profile define input energy density. The building atmosphere and material of the substrate also influence the quality of parts produced by DMLS. Metals such as Titanium aluminide need to be produced in an argon atmosphere to prevent the formation of oxides. The formation of oxides negatively affects the mechanical properties of the produced DMLS parts (Yadroitsev, 2009).

Process input parameters:

- Laser power;
- Scanning speed;
- Powder layer thickness;
- Design and build strategy – scanning strategy, supports and orientation.

Low scanning speed tends to form distortions and irregularities while excessively high scanning speed tends to form drops (balling effect). High scanning speed promotes lower cooling rates and therefore results in a coarser microstructure. Higher laser power and slower scanning speed promote the formation of finer microstructures. Close control of the amount of heat in the melt pool is required. High

temperatures in the melt pool can lead to oxidation. Oxygen is unfavourable for the ductility of Titanium aluminide through forming an interstitial solid solution with titanium at high temperatures. The stability of the single track is dependent on the laser power, scanning speed, layer thickness, substrate material, physical properties and the morphology of the material (Sun & Karppi, 1996).

The difference in heat expansion rates of the different metals causes internal stresses to develop in the intermetallic zone. Metals with different melting points, using the same heat source will mean that the metal with the lower melting point will be molten before the other metal gets molten. One metal melts first and causes uneven heat flow and non-uniform dilution in the molten pool. When the melt pool solidifies the metal with a higher melting point is already solid at the time the metal with the lower melting point is still liquid or it is still in a mushy state (Sun & Karppi, 1996).

The difference in thermal conductivity produces different heating and cooling rates. The metal with higher conductivity will tend to draw heat away from the melt pool. Differences in conductivity may result in uneven heat flow and prevent complete fusion of the lower conductivity metal. Uneven flow affects solidification and can lead to distortions. The difference in melting points will cause the metal with the lower melting point to separate out in the course of cooling and solidification, which increases the risk of crack formation in the low melting point metal (Sun & Karppi, 1996).

To achieve high-density parts it is important to identify the optimum set of parameters and conditions to use in building the parts, from single tracks to layers and from layers into the 3D part, to achieve the desired high densities and low roughness (Spierings *et al.*, 2011).

In laser-based processes, the energy density (E) is important. Sufficient energy density is required for the melting of powder particles of the current layer and of the previous layer to assure a good penetration depth between successive layers (substrate) and to ensure complete fusion and eliminate porosity. However, excessive energy may cause defects.

Material based input parameters:

- Chemical Composition;
- Optical Properties;
- Physical properties (particle size, powder morphology, density);
- Mechanical properties.

Powder properties directly influence the deposition of powder onto the substrate and the formation of the molten pool. The distribution of powder is primarily affected by properties such as powder size distribution and morphology of the powder particles. Particle shape or powder morphology refers to the shape of the individual powder particles. The shape of powder particles determines how the particles position themselves or pack together.

In the DMLS process particle shape is an important factor in creating an optimal layer thickness for fully dense objects. Spherical particles are preferred for the DMLS process as they flow easily to form a homogenous powder layer and have higher packing density, which is beneficial for molten pool formation (Spierings *et al.*, 2011).

Particle shape also has an influence on the absorptivity of the powder bed. The larger the absorptivity the more energy from the laser beam will be absorbed by the powder bed. Particle shape and particle size distribution also affect powder flowability. Powder flowability is defined as the ability of the powder to flow in the desired manner. It is important to have good powder flowability when depositing a thin powder layer, because it ensures a layer with consistent thickness. Powder with a particle size in the range of 0.1-5 μm tends to agglomerate in clusters and prevent uniform recoating during the AM process, while larger particles in the range of 90-120 μm reduce the maximum layer packing density (McGeary, 1961).

A mixture of small and large particle sizes is preferred, since such particle sizes would permit the smaller particles to penetrate between the larger particles and suitably fill the voids to achieve higher parking density. Inaccurate selection of powder particle size distribution can cause in situ segregation due to the mechanical re-coater pushing coarser particles away from the bed, which would result in

production of unacceptably heterogeneous parts. Generally, fine powders with wide powder particle size distribution produce parts with higher fractional density (McGeary, 1961).

Liu *et al.*(1990), investigated the effect of powder particle size on the mechanical properties of as-built DMLS samples and found that metallic powders with higher particle size distribution have higher flowability and ultimate tensile strength. An optimal powder layer thickness has to be selected for employed powders. In addition, when considering the particle size, the maximum diameter of the particles should be less than the laser spot size (Yadroitsev,2009).

2.3.4 Powder Characteristics

Spierings *et al.* (2011) highlight powder characterization as a crucial part of the additive manufacturing process. It is to ensure good powder quality and consistency in the mechanical properties of the 3D parts made. Powder properties such as size, morphology (shape), surface area, porosity and impurity content have a direct effect on the manufacturing process and the mechanical properties of the final part. Figure 13 shows the powder parameters that should be taken into consideration when characterizing a metallic powder for use in an additive manufacturing process (Benson & Snyders, 2015).

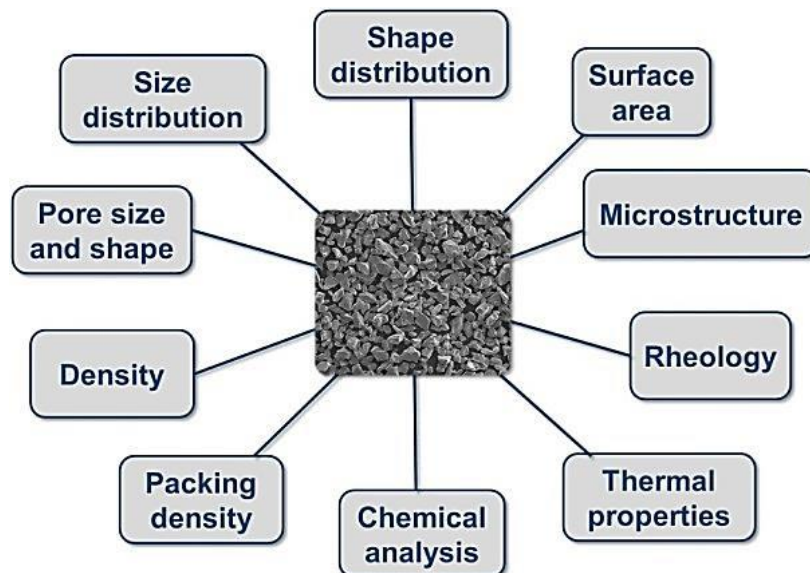


Figure 13. Major powder characterization parameters for AM (Benson & Snyders, 2015).

2.3.4.1 Titanium Powder

Commercially pure titanium (CP Ti) is unalloyed material and available in grades 1, 2, 3 and 4. Grade 2 is known for its excellent formability, superior corrosion resistance and moderate strength. It is therefore the preferred metal for several applications (Elagli *et al.*,1989). CP Ti can undergo an allotropic transformation from the hcp alpha phase to the bcc beta phase dependent on the operational temperature. It is mostly used in manufacturing of marine and chemical vessels, jewellery and medical industries (Donachie, 2000). The typical physical and mechanical properties of pure Ti are recorded in **Error! Reference source not found.**

Table 3. Typical physical and mechanical properties of pure Ti (grade 2) (ASM aerospace, 2016)

Property	CP Ti (grade 2)
Density, Kg ^m ⁻³	4500
Melting point, °C	1650-1670
Specific heat, J·kg ⁻¹ ·K ⁻¹	528
Thermal conductivity, Wm ⁻¹ ·K ⁻¹	17
Thermal diffusivity, m ² ·s ⁻¹	7.15 × 10 ⁻⁶
Heat of fusion kJ/kg	435.4
Boiling point, °C	3287
Ultimate tensile strength, MPa	220
Yield strength, MPa	140
Elasticity modulus, GPa	116
Elongation at break, %	54
Hardness, HV	60

The typical physical and mechanical properties of the Al are recorded in Table 4.

Table 4. Physical and mechanical properties of Aluminium (ASM aerospace, 2016)

Melting point	933.47 K (660.32 °C, 1220.58 °F)
Boiling point	2743 K (2470 °C, 4478 °F)
Heat of fusion	10.71 kJ/mol
Heat of vaporization	284 kJ/mol

Molar heat capacity	24.20 J/(mol·K)
Crystal structure	face-centered cubic (fcc)
Thermal expansion	23.1 $\mu\text{m}/(\text{m}\cdot\text{K})$ (at 25 °C)
Thermal conductivity	237 W/(m·K)
Electrical resistivity	28.2 n $\Omega\cdot\text{m}$ (at 20 °C)
Crystal structure	face-centered cubic (fcc)
Speed of sound- thin rod	(Rolled) 5000 m/s (at r.t.)
Thermal expansion	23.1 $\mu\text{m}/(\text{m}\cdot\text{K})$ (at 25 °C)
Thermal conductivity	237 W/(m·K)
Young's modulus	70 GPa
Shear modulus	26 GPa
Bulk modulus	76 GPa
Poisson ratio	0.35
Vickers hardness	160–350 MPa
Brinell hardness	160–550 MPa

2.3.5 Advantages and Disadvantages of DMLS

DMLS is well known for its advantages such as the possibility to produce fully dense parts, the reduced machine set-up time, its ability to produce sharp internal corners and difficult geometric features, reduced machine minding, its ability to produce parts with a high degree of accuracy, the possibility to produce net shaped complex functioning parts, the production of parts with high quality details and the fast production of custom parts with no extra tooling required (Jacobson & Bennett, 2006).

However, DMLS systems also have some limitations. The size of the part being built is limited to the size of the powder bed in the machine. There is an inevitable degree of surface roughness because the part is built from powder and additional machining or chemical treatment is required to improve the surface finish. The DMLS parts can also have porosity, however, this can be reduced and eliminated during the building process. The EOS DMLS machine has limited feedback to provide accurate monitoring and controlling of the build process during operation. Errors that occur during the building process such as short-fill recoating are not flagged during the process and therefore the machine takes no corrective steps (Jacobson & Bennett, 2006).

Build quality and machine performance is critically dependant on the operation of the recoater arm. The recoater arm motion can cause non-uniform distribution of the metal powder and cause distortions in the parts built. The recoater arm can 'bump' over an edge of a part and cause a vibration in the build volume, and because of the high density of the metal powder, this can lead to uneven powder settlement, which prevents even recoating during subsequent sweeps. This happens if the long edge of the recoater arm is parallel to long edges of the parts being built. The solution to this problem is to build the parts such that there is always an angle of more than 5 degrees between any long edge and the long edge of the `recoater arm. The use of supporting skis or sloping edges should be considered to reduce the bumping effect. Supporting structures on the sides of the part can also be useful in preventing the recoater arm from knocking it over during the building process, especially if it has a small footprint (Jacobson & Bennett, 2006).

2.3.6 Optimizing the process parameters of DMLS

An approach to optimizing the DMLS process parameters for a specific alloy that is found in literature proceeds from single layers to single tracks to 3D objects.

2.3.6.1 Single Tracks

In the approach a thin layer of powder is deposited onto a substrate or on a previously melted layer, the laser beam then scans over the surface of the powder at the selected locations of the powder bed at a controlled speed and fuses the powder. After scanning the surface of the powder, the substrate is lowered and another layer of powder is deposited, so that the surface of the powder remains in the focal plane of the laser (Yadroitsev, 2009). Figure 14 shows the geometrical characteristics of a single track.

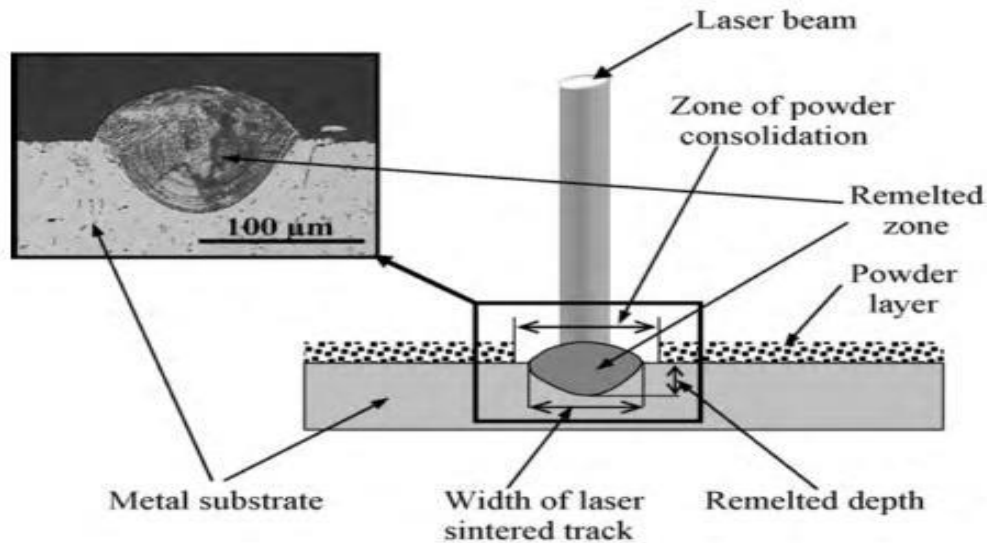


Figure 14. Geometrical characteristics of a single DMLS track (Yadroitsev, 2009).

It is important that the track formed penetrates into the substrate or the previous formed layer to ensure that continuous and stable tracks are formed. The features of a single track depend on laser power, scanning speed, powder layer thickness, substrate material, physical properties and granulomorphometry of the powder used (Yadroitsev *et al.*, 2007). The process parameters that result in stable and continuous tracks vary according to each specific metallic powder material, and therefore for each metallic powder material several single track trial runs need to be completed at different process parameters to determine and select the optimum process parameters of the specific powder material (Yadroitsava *et al.*, 2015).

The laser-powder bed interaction can be divided into three stages: preheating, melting with shrinkage and re-solidification. The laser-matter interaction is dependent on several physical parameters such as power density, wavelength and pulse duration and the thermodynamic and physiochemical properties of the material. Figure 15 shows an illustration of laser-powder interaction. In laser powder interaction the free electrons of the material absorb the energy of the laser radiation, the photons from the electro-magnetic field causes the free electrons to fluctuate and the energy will then be transmitted to the other electrons and to the crystal lattice (Yadroitsava *et al.*, 2015).

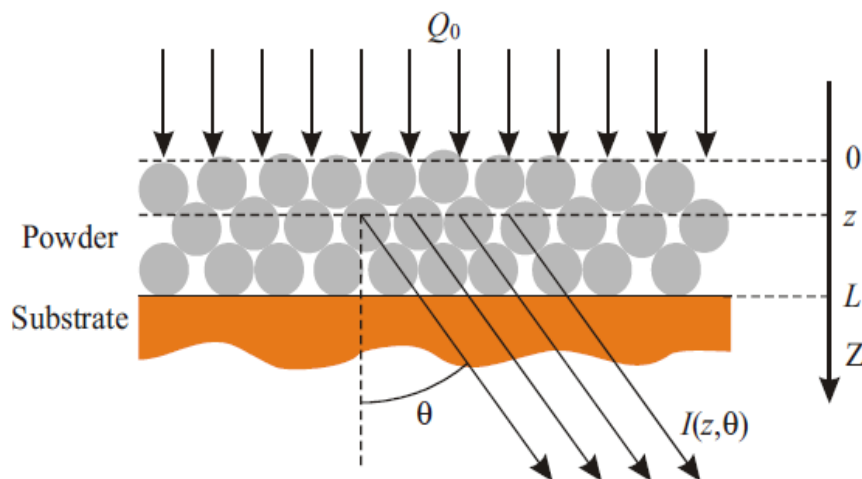


Figure 15. Laser radiation transfer in a powder layer on a substrate: Q_0 incident power density, z powder depth, L layer thickness, θ radiation propagation angle, and $I(z, \theta)$ radiation intensity (Gusarov *et al.*, 2009).

The limited interaction of the powder and heat source that is caused by the high scanning speed of the laser beam leads to rapid heating, melting and circulation of molten metal driven by surface tension and temperature gradients. During melting drastic shrinkage occurs from 50% powder packing density to ~100% solid material density. The resulting heat flow will determine the geometry of the melt pool, the cooling rate and the transformation reaction in the melt pool and heat affected zone (Kruth *et al.*, 2005).

Laser power density (Q_0) is defined as the ratio of laser power to laser spot size. Laser power density determines the depth (z) and width of penetration of the track into the substrate, while the powder layer thickness (L) determines the height of the track. The power density of the laser determines the temperature gradient and the scanning speed determines how long the heat source will interact with the material. A high energy density with low scanning speed will cause a deep pool and some of the material to evaporate. The re-melted depth is of major importance as the penetration into the previous layer is required for good cohesion (Kruth *et al.*, 2005).

The geometry of the single track is dependent on the amount of metal powder material involved in the process. If the layer thickness is too high, optimal adhesion of the track to the substrate or previous layers will be hard to achieve because of

inadequate melting depth. The adjacent powder due to scattering of the radiation, conduction through the solid material and neighboring particles and capillary phenomena also needs to be melted to form the track. The melt pool geometry influences the grain growth and the resulting microstructure of the parts. A high temperature gradient causes non-equilibrium of solid/liquid interface leading to rapid solidification of the melt. Due to this rapid solidification various effects arise; among these are changes in general microstructure and non-equilibrium phases (Kruth *et al.*, 2005).

Yadroitsev *et al.* (2010) states that low scanning speed causes instability of the molten pool due to an increase in melt volume and decrease in melt viscosity. Reducing laser power at low speeds influences the penetration and thus the stabilizing effect that penetration gives to the molten pool. At low scanning speeds instabilities such as distortions and irregularities of the track occur and at high scanning speeds tracks can break up into drops and this phenomenon is called the “balling” effect (Figure 16).

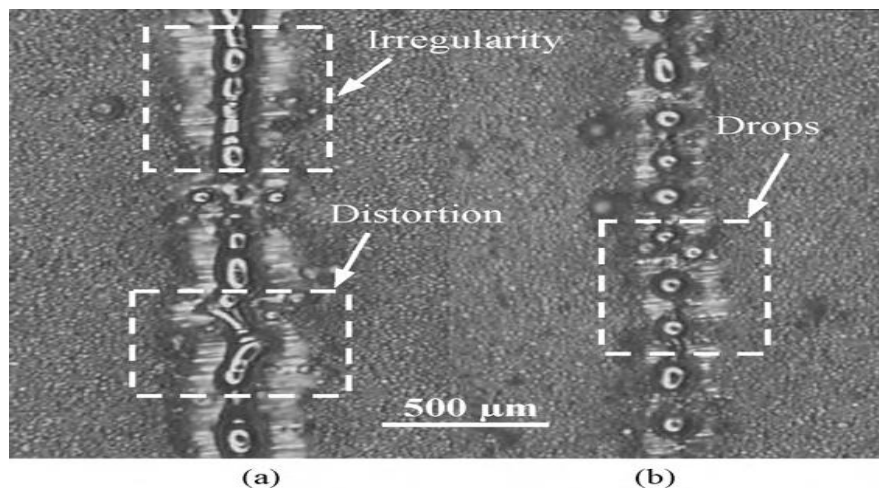


Figure 16. Instability of laser sintered tracks from stainless steel grade 316L (-25 μm) powder on (Yadroitsev, 2009)

Balling occurs when the molten material does not wet the underlying substrate due to surface tension, which tends to spheroidise the liquid. Balling leads to rough surfaces obstructing smooth layer deposition and decreasing the density of the part. Since liquid metals do not wet oxide films in the absence of chemical reactions it is important to avoid oxidation and have sufficient re-melting of previous layers to break down oxide films and provide a solid-liquid interface (Yadroitsev *et al.*, 2010).

Thijs *et al.* (2010) states that a simple parameter such as scanning speed could vary slightly and cause the density to fall. Figure 17 shows how the scanning speed influences the relative density at three different layer thicknesses for AISI 316L stainless steel processed in a Concept Laser M3. Different scanning speeds could produce desirable densities if the layer thickness is adjusted to accommodate the scanning speed of a certain power density laser.

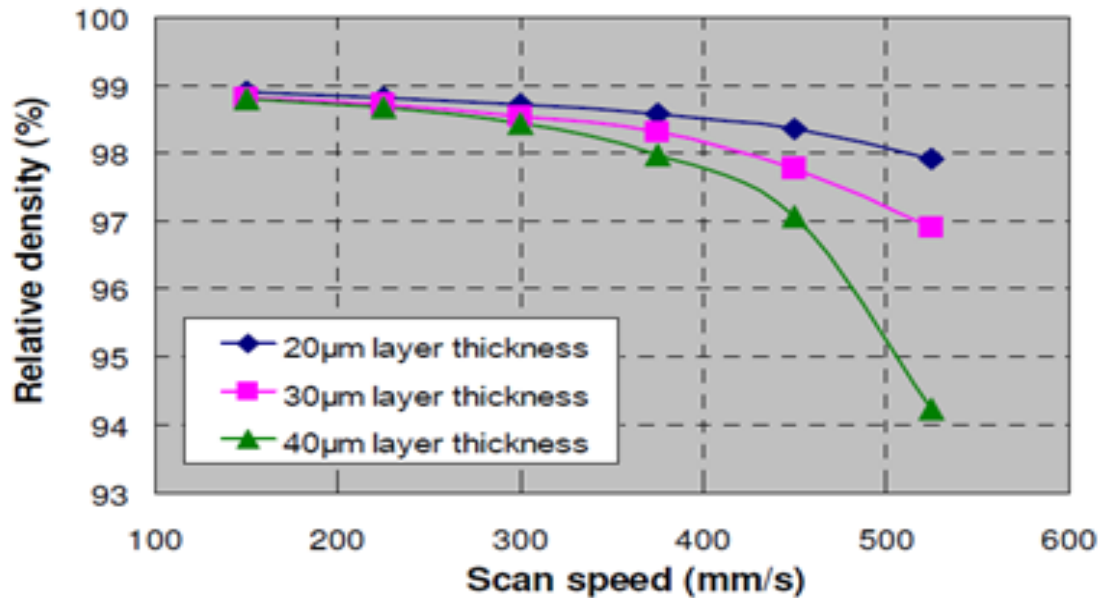


Figure 17. The effect of scanning speed on the relative density for AISI 316L stainless steel processed on a Concept Laser M3 machine (Thijs *et al.*, 2010)

Single track formation involves powder placed directly under the laser spot, it involves the adjacent particles that are due to scattering of radiation, and it involves conduction through the substrate and through neighbouring particles. Each layer of the part is filled with single tracks of melted powder. The area of the substrate without powder after laser scanning can be twice as large as the width of the track and is referred to as the “denudation zone” as indicated in Figure 18 (Yadroitsev *et al.*, 2015).

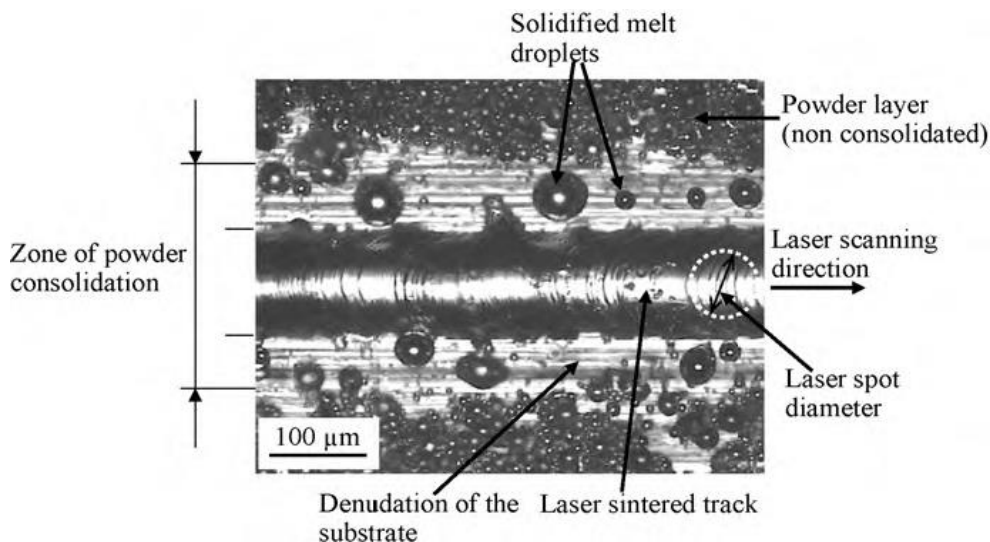


Figure 18. Top view of a laser sintered track (Yadroitsev *et al.*, 2015)

The width and the remelted depth of a single track have a linear dependence: they decrease with decreasing scanning speed and decreasing laser power. An increase in the laser scanning speed results in the absorbed energy of laser radiation going directly into fusing the material. Consequently, there will be a reduction in the heat loss by conduction, and the width of the single tracks will be comparable to the laser beam diameter (Yadroitsev *et al.*, 2010).

Under DMLS conditions, heat conduction, melting, densification and cooling takes place simultaneously within a short period of time. Different materials behave differently under similar DMLS conditions. Heat transfer is induced by good wettability of the substrate and a wide zone of contact (Yadroitsev *et al.*, 2010).

2.3.6.2 Single Layers

A single layer is formed from a sequence of single tracks. Single layers are a superposition of the fused single tracks. The properties of the single layers depend on the geometric characteristics of the single tracks, hatch distance (the distance between the tracks) and the scanning strategy. All these properties have a direct influence on the residual stresses in the part, they influence the density of the part and the microstructure of the part formed. The concept of re-melting layers during DMLS may improve the properties of the part built, however, it increases production costs and the production time (Yadroitsev *et al.*, 2015).

Scanning strategies are also known as “laser scan paths” and different manufacturers provide different options. Scanning strategies are the patterns formed by the tracks of each layer. These scanning strategies include one-zone strategy, two zone strategy, island strategy and hatch pattern along xy and alternating xy for different requirements.

Figure 19 shows top views of single layer produced by one-zone and two-zone strategy of laser scanning.



Figure 19.(a) Top view of single layer produced by one-zone strategy (b) and two-zone strategy (Yadroitsev *et al.*, 2015).

One-zone strategy is when tracks are in one direction and overlapping each other. A two-zone strategy is when each layer is melted twice with the laser: at first, the laser scans through and melts the powder layer and then successively the laser beam passes in between sintered tracks and re-melts each two neighboring tracks. Rescanning improves the surface quality of single layers; it facilitates reduction of roughness and reduces the appearance of droplets (Yadroitsev *et al.*, 2015).

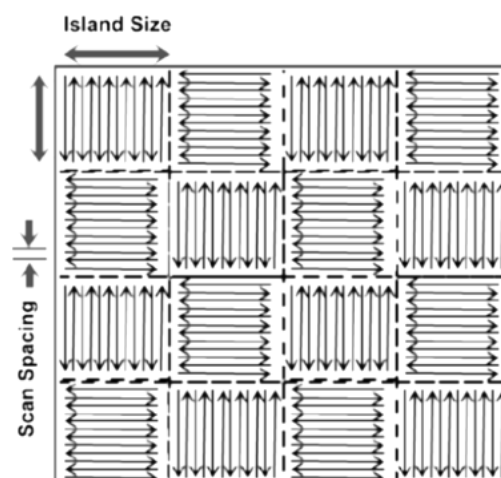


Figure 20.Schematic of the island scan strategy (Qiu, 2013)

Figure 20 shows the island scanning strategy. The area is divided into small square islands and the scanning sequence then randomly selects the different squares to be scanned. Changes to the size and orientation can be made between the layers (Thijs *et al.*, 2010).

The thermo-physical conditions of the different strategies are different. This is because the absorptivity, reflectivity, thermal conductivity and heat transfer of powder and solid material differ from each other. During the DMLS process, the inner solidified layer is subjected to several heating and cooling cycles. When the hatch distance is more than a single-track width, powder is melted in a sequence of individual tracks. Non-optimal hatch distance can result in formation of gaps between tracks in a single layer, which causes chains of pores in the final DMLS part (Yadroitsev *et al.*, 2015). The scanning direction of an object can be rotated from layer to layer. The hatch distance contributes to achieving successful dense parts. When the hatch distance is too large, porosity will increase and weaken the final mechanical and structural properties of the object. When the hatch distance is too small it will increase the total cost and time of production (Yadroitsev *et al.*, 2015).

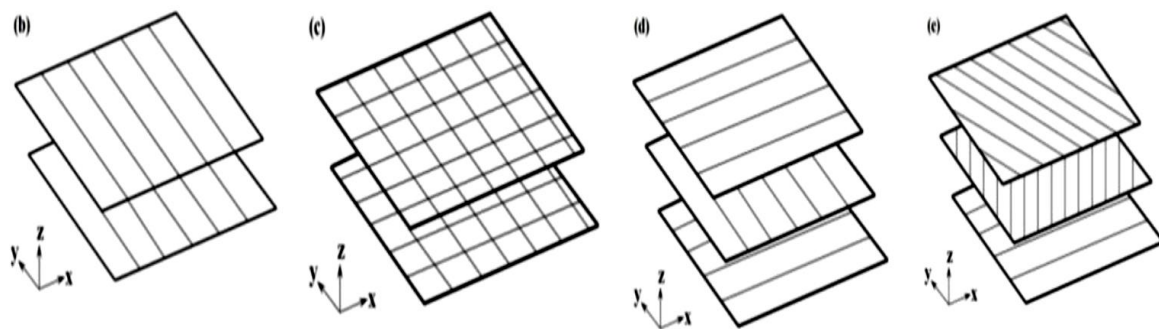


Figure 21. . Different scan patterns a) one direction b) double scanning each layer c) alternating scanning d) the direction of scanning rotated through a certain angle between consecutive layers (Yadroitsev *et al.*, 2015).

The scanning strategy has a major influence on the residuals stresses in the part. DMLS specimens are exposed to bending stresses. Figure 22a shows the rapid heating of the upper surface accompanied with slow heat conduction causing a steep temperature gradient. Because the surrounding material restricts free expansion, compressive strains will occur at the top layer. During cooling, the

compressed upper layers become shorter than bottom layers causing bending towards the laser path.

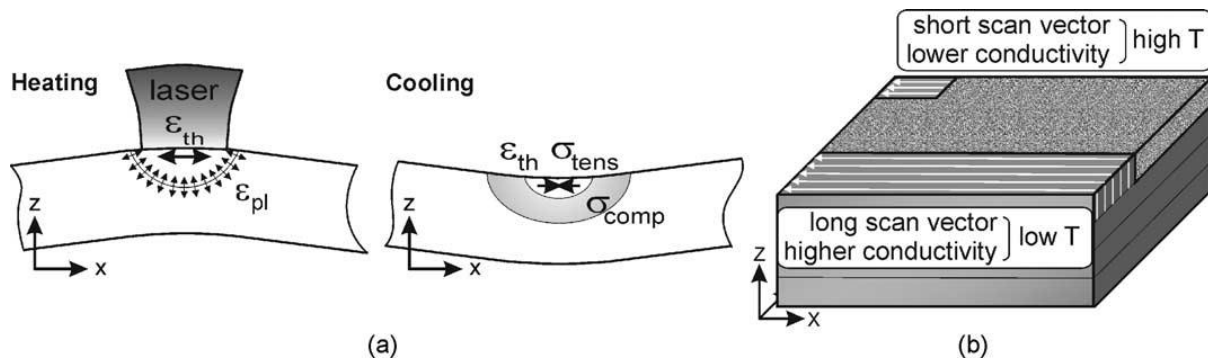


Figure 22. Bending stresses within the specimens (Kruth *et al.*, 2004)

The way in which these stresses are generated results in them attempting to bend the consolidated layers towards the laser beam, which in turn could cause distortion and part failure by delamination or cracking. The cooling of layers below the top layers adds to the tensile stress in the part as they are shrinking while their temperature is lowering (Kruth *et al.*, 2004)

The part geometry and scanning strategy influences the internal stresses induced. If the scanning area is small, short scanning vectors are used, which will in turn cause little cooling time for adjacent tracks, resulting in higher temperatures of the scanned area. For larger scanning vectors adjacent tracks have more cooling time, leading to lower temperature of the scanned area, see Figure 22 b. Lower temperatures could cause worse wetting conditions, leading to density issues. When scanning small zones such as corners, less heat sink volume is available with the powder acting as isolation, causing higher temperatures to result in these areas (Kruth *et al.*, 2004).

2.3.6.3 3D Objects

To produce a successful 3D object using the DMLS process requires that the single tracks are stable and continuous with no defects and the single layers are formed effectively to produce fully dense 3D parts without defects. The material properties of the 3D part formed, such as yield strength, elongation, ductility and hardness are directly affected by the microstructural features, therefore the mechanical properties obtained with DMLS differ from conventional production techniques (Kruth *et al.*, 2010) Yadroitsev *et al.*, (2015) confirmed that the properties of parts produced by the

DMLS process depend on the geometrical characteristics of each single track, the morphology of each single layer, and the interconnection of tracks and layers. Changing only one process parameter or powder property could cause changes in the properties of the 3D object.

A schematic of the selection process is shown in Figure 23. It illustrates the necessary areas of focus when evaluating or developing a set of parameters for successful manufacturing of 3D objects by DMLS from different materials. The process parameters of DMLS are critical for the production of successful 3D objects with suitable properties for different materials and applications.

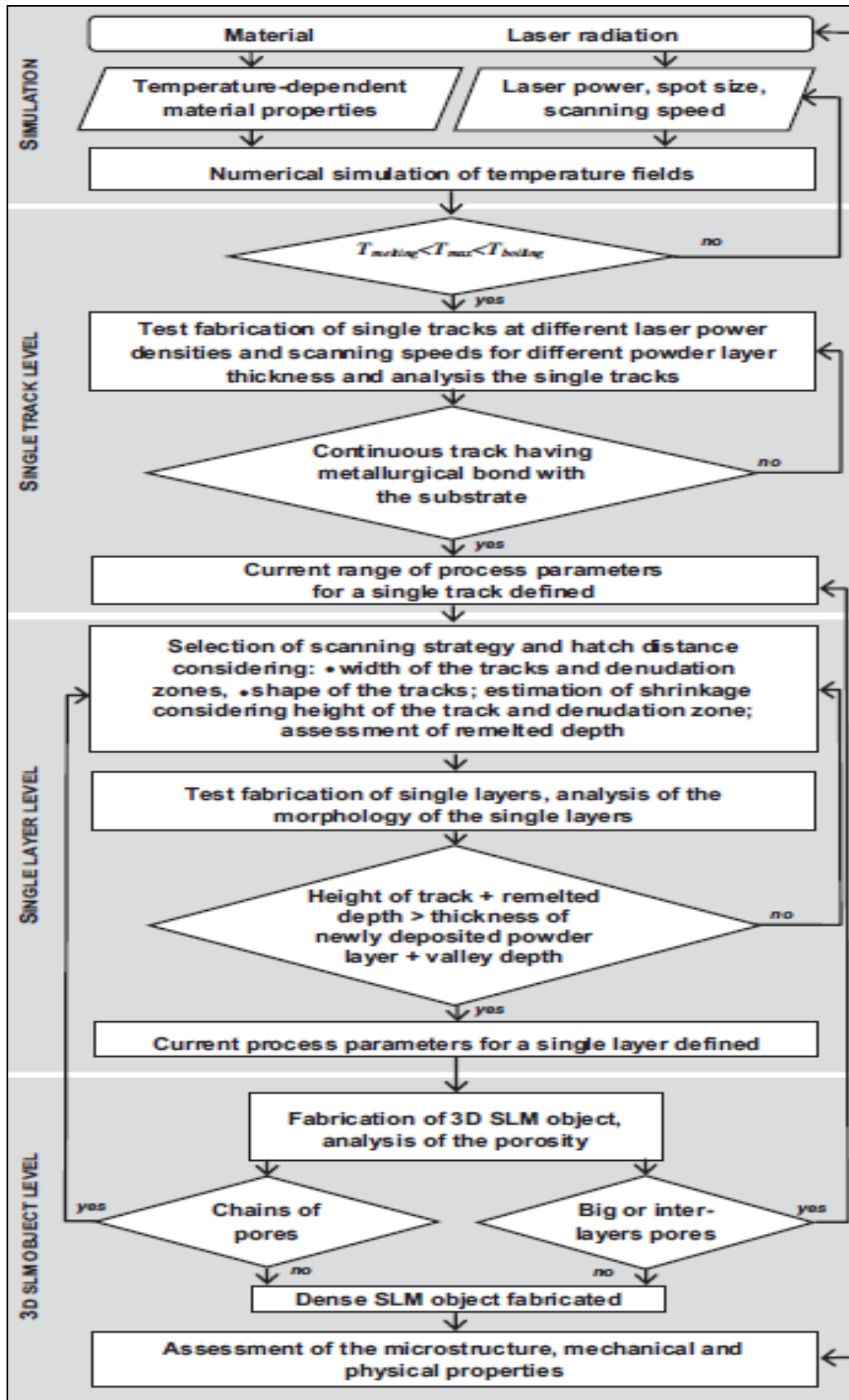


Figure 23. Algorithm for optimal DMLS process parameters (Yadroitsev *et al.*, 2015).

2.4 Mechanical properties of DMLS Titanium aluminide -based alloys

Loeber *et al*, (2011) in a comparative study of Titanium aluminide from EBM and DMLS processing, concluded that the oxygen content and the amount and type of porosity have the biggest influence on the mechanical properties. The results showed that the Al content dropped by at least 1.22 wt.% from the original powder content to the final specimen content. The oxygen content was observed to increase from the original powder content by 60% in the specimen after DMLS.

Baudana *et al.*(2016) reported that there was a slight aluminium loss in the as-EBM built Titanium aluminide parts and further reported that the reduction was due to evaporation, because Al has a lower melting point than Ti. The Al evaporation was constant and repeatable once the process parameters were fixed. The Al content can be managed by making provision for higher Al content in the starting powder. The density of DMLS parts can achieve a maximum density of around 99.9%. Optimization of the DMLS process parameters is necessary to improve the density Loeber *et al.*, (2011).

CHAPTER 3 – METHODOLOGY

This chapter gives a detailed description of the methodology followed in the study including the powder materials, the machines, and the measuring equipment used during the experimental work.

3.1. Schematic summary of the research methodology

In figure 24, the flow diagram provides an overview of the different aspects of the research. Single tracks and single layers were produced at different process parameters (laser powers and scanning speeds) to identify optimum process parameter suitable for the DMLS manufacturing approach. When the process parameters were determined, 3D test specimens were built tested and results were compared to results that were produced from the wrought and pre-alloyed manufacturing approaches.

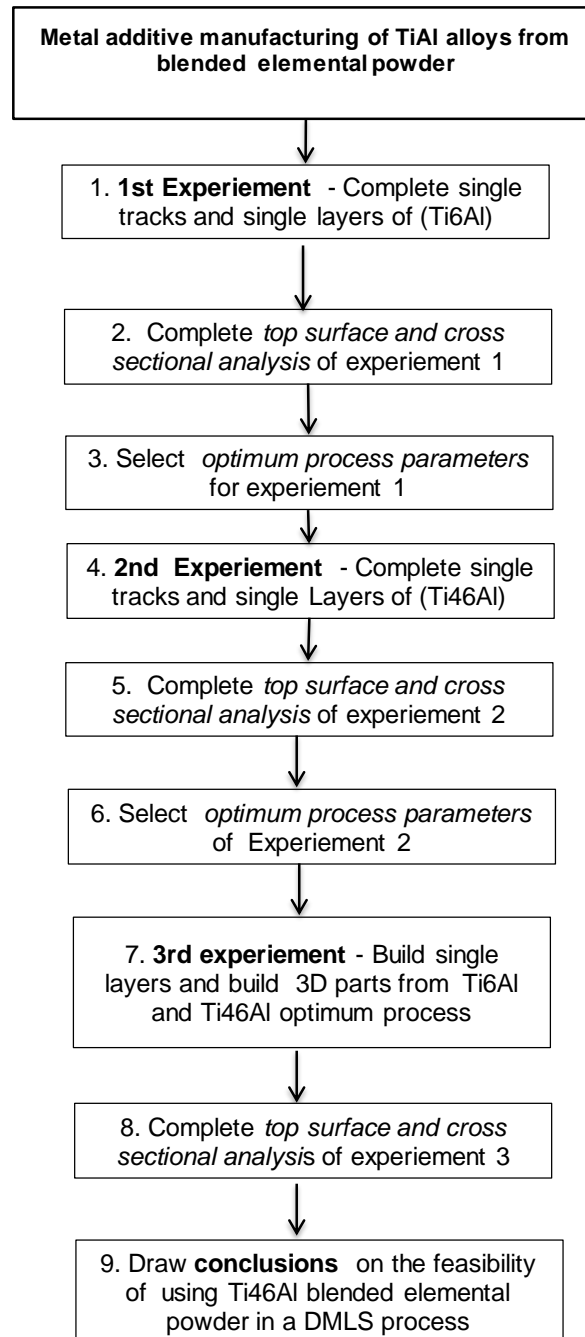


Figure 24. Schematic of research methodology for the study

3.1.1 Ti6Al experiment

Manufacturing the single tracks

The powder was prepared for the in-situ alloying process by mixing 50 g of Ti and 3.2 g of Al to make up 94 wt% Ti and 6 wt% Al. The two powders were mechanically mixed by stirring by hand for 30 minutes using a wooden stick of diameter 6cm in a 15cm diameter-mixing vessel. The Ti particle size was $<45 \mu\text{m}$ and the Al powder particle size ranged from 20 - 45 μm as-supplied specification. 99.8% pure Al spherical gas atomized powder was used.

The chemical composition of the employed powder is shown in Table 5.

Table 5. Chemical composition of CP Ti powder in weight %

Element	Ti	O	Fe	C	H	N
	ISO 5832-2 (Cp-Ti grade 2)					
Composition	Bal	≤ 0.45	≤ 0.30	≤ 0.10	≤ 0.0125	≤ 0.05
	Powder used in current study					
Composition	Bal	0.17	0.062	0.006	0.002	0.012

The particle size distribution of the CP Ti powder is given in Figure 25. The equivalent diameters of the 10th, 50th and 90th percentiles were $d_{10}=11.6 \mu\text{m}$, $d_{50}=24.6 \mu\text{m}$ and $d_{90}=38.4 \mu\text{m}$ respectively. The powder was gas atomized and it is spherical in shape.

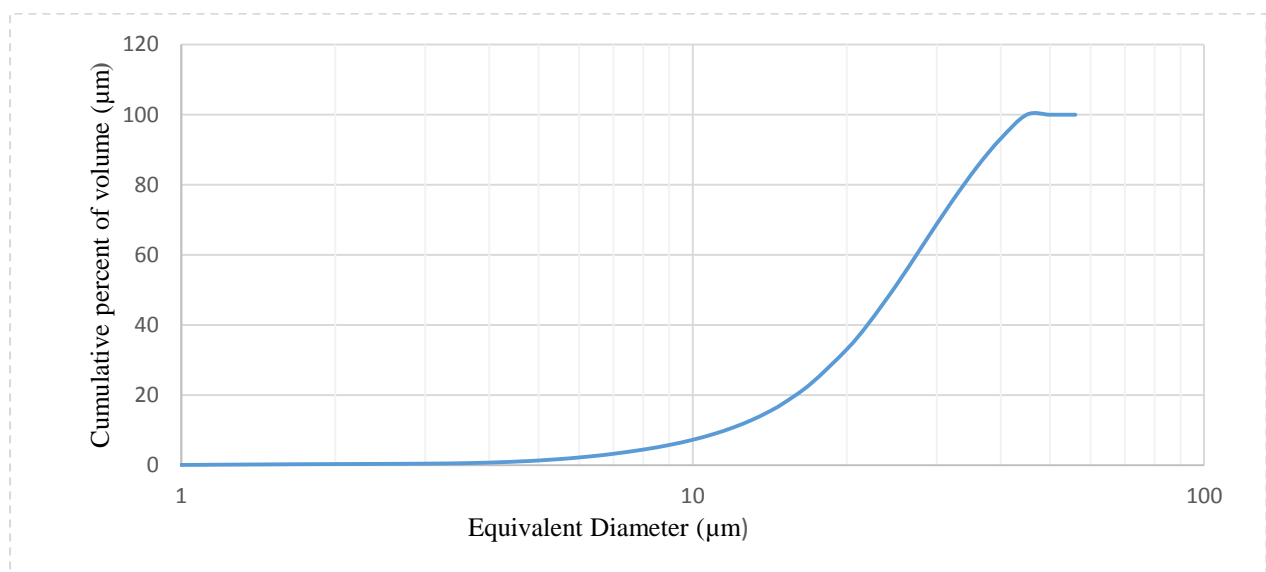


Figure 25. Particle size distributions for employed CP Ti powder.

The mixed powder was placed in an oven for 1 hour at 80°C. This was done to dry the powder and to improve the powder flowability. The original oxygen content as displayed on the M280 DMLS machine was 21%, was agornised and dropped to 0.1%.

All tracks were of 20 mm length. For each scanning speed, three single scan lines were produced. A gap of 1.0 mm was used between adjacent single tracks to avoid any interaction between neighbouring scan tracks. To easily differentiate each set of scan lines a gap of 2 mm was placed between each set of single tracks produced by a particular scanning speed.

The direct metal laser sintering process was followed, using an EOSINT M 280 machine from EOS GmbH (Figure 26). The EOS M280 machine was setup and the Ti6Al4V substrate was used and levelled to ensure that the surface is flat.

The machine comprises of a process chamber with the recoating system, computer controlled elevating systems, platform module, and an optical system with a laser, a process gas management system and a process computer with control software. The machine is equipped with a 400 W Yb-fibre laser. The process chamber was filled with high purity argon gas to permit processing of the reactive titanium alloy powders.

The EOSINT M280 machine can scan its laser up to a speed of 7 m/s and can have an exposure area of 250 mm x 250 mm. The EOSINT M 280 machine is computer controlled by process software called PSW. The PSW software virtually controls the whole machine; it is used to program the building protocol prior to the manufacturing process. The graphical layout of the parts, which will be built, is displayed on the computerized screen by the PSW software.

The machine set-up comprised of sieving and refilling of the powder-dispensing container, build platform preparation, selection of the right recoater blade, levelling the recoater blade with the build platform and flushing the building environment with argon gas to achieve the minimum acceptable oxygen content of 0.07-0.12%. The level of oxygen gas content in the build chamber is also of great concern since it can cause oxidation of the manufactured part

Sieving of the Powder

The powder needs to be sieved before it is used, to remove any agglomerates or other large particles and to ensure even distribution of the metal powder.

During the sieving process, it is critically important to wear the recommend protective clothing namely a mask, gloves, a laboratory coat and antistatic shoes. The sieve used with the EOSINT M280 machine is shown in Figure 27.

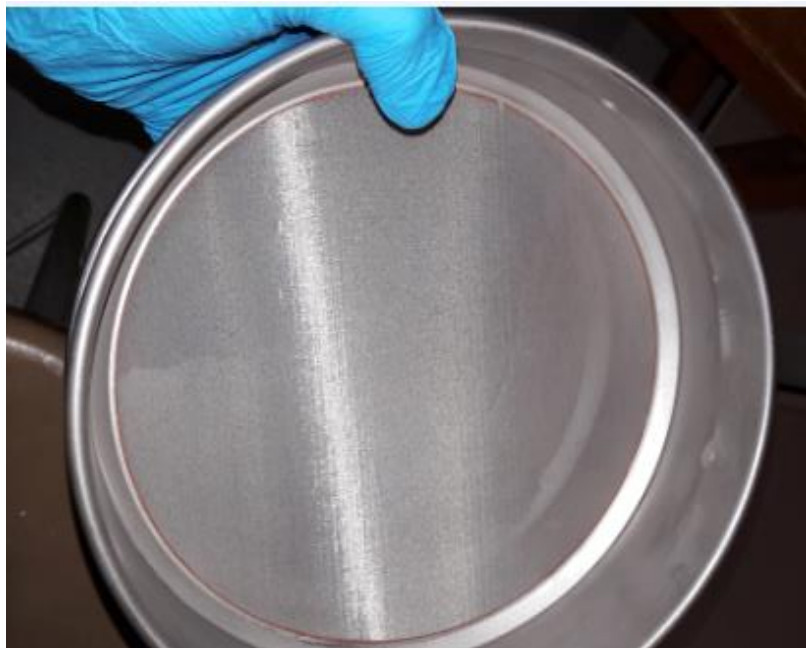


Figure 26. Sieving of the powder manually

Platform preparation

A Ti6Al4V plate was used as the base plate. The base plate, which served as substrate is held in place by four corner screws onto the elevating system on the carrier plate in the process chamber (see figure 28). The platform was set to move down at a precisely predetermined value based on the desired powder layer thickness.

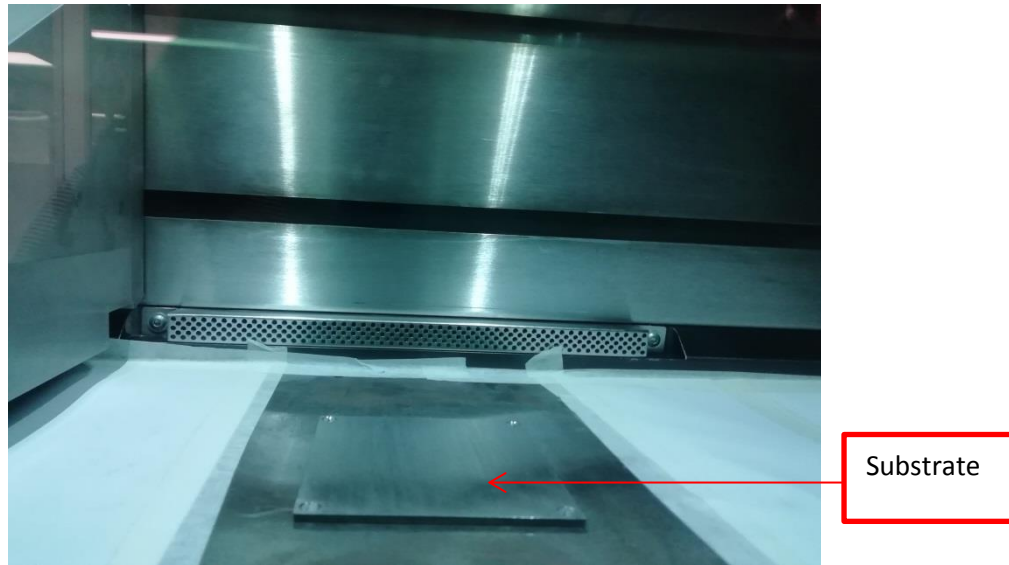


Figure 27. The substrate prepared and levelled onto the elevating system

Recoater blade settings

Setting the gap between the re-coater blade and the base plate accurately is very important because it is the main tool that controls powder deposition on the substrate. The manual setting of the gap between the re-coater and the base plate is a complicated task. This part of the preliminary activities is crucial because it can affect the densification of the build parts if the re-coater does not deposit the powder evenly. A gauge clock and feeler gauge were used to level and determine the gap between the base plate and the re-coater blade. The feeler gauge was used to determine the gap between the base plate and the recoater blade, which determined the deposited powder layer thickness. For the current experiment, the powder layer thickness was 60 μm and a feeler gauge of 0.06 mm thickness was used to set the gap between the base plate and the recoater blade (Khaing *et al.*, 2001).

The Protective atmosphere

Ti-based alloy powders are highly reactive and therefore be processed under an inert atmosphere. In the EOSINT M280 machine, an argon gas was flushed continually into the building chamber. The type of gas used could influence the depth of penetration of the laser beam into the substrate (Kurzynowski *et al.*, 2012).

An example of completed single tracks and single layers on the Ti6Al4V substrate are shown in Figure 29.

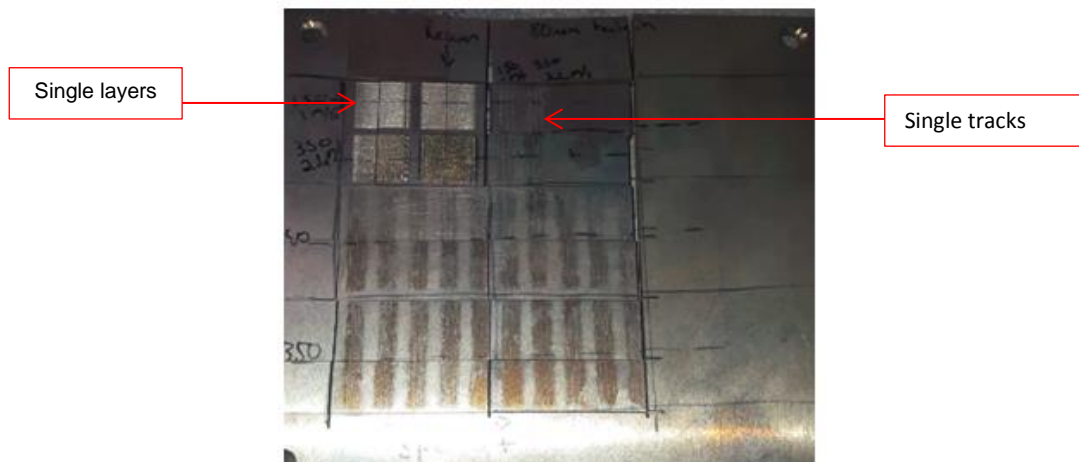


Figure 28. Top view of the substrate with single tracks and single layers

Top surface analysis

The top surface analysis of the single tracks was done by using the ZEISS Axio Scope.A1 optical microscope shown in Figure 30.

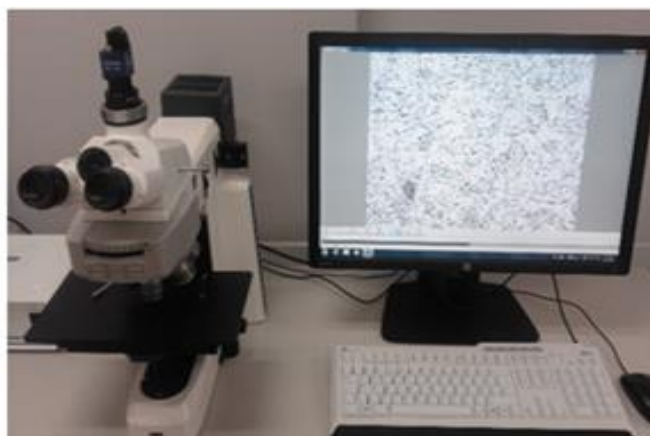


Figure 29. Optical microscope (ZEISS Axio Scope.A1)

Using the microscope the single tracks were analysed (the single track width, cross-section height, the depth of penetration between the deposited alloy and substrate) to understand the interaction of the process parameters at different laser power and at different scanning speeds. The single track widths were measured and plotted on graphs for interpretation. The relationships of the width of the tracks with the scanning speed, the laser power and the linear energy density were analysed and interpreted. A process map was developed using the scanning speeds and the laser

powers to show the range of continuous single tracks, the range of balling and pre-balling single tracks.

Cross sectional Analysis

For metallographic analysis, the samples were cross-sectioned into smaller units for mounting using the Struers CitoPress-1 machine (Figure 31(a)). The samples were mounted in ClaroFast. The mounting of each sample took 4 min at a temperature of 180°C and a pressure of 350 bar. The samples were subsequently cooled by water for 6.5 min.

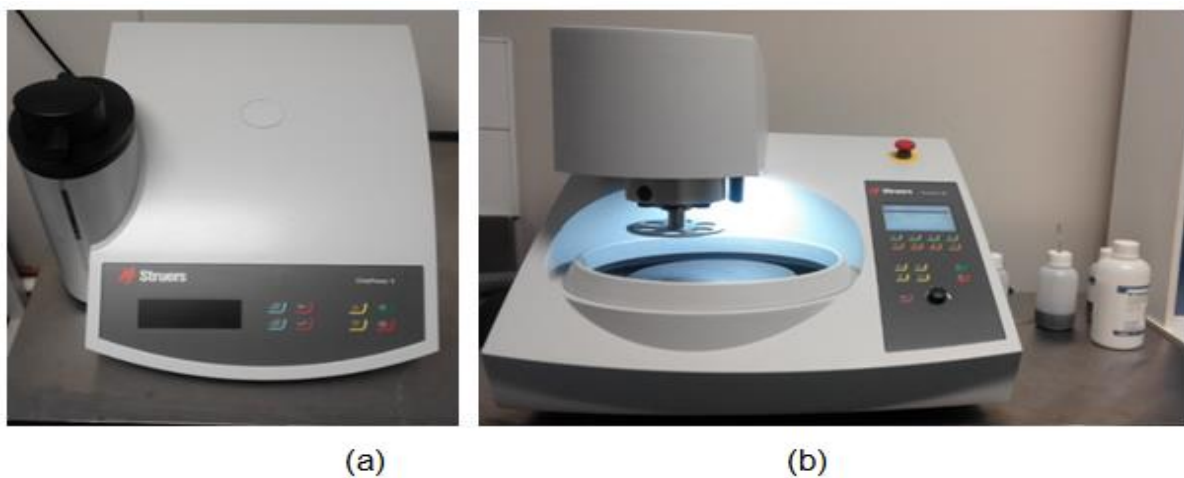


Figure 30. Struers CitoPress-1 (a) and polishing machine Struers Tegramin-25 (b).

Grinding and polishing of the samples were conducted with a Struers Tegramin-25 (Figure 32(b)) according to the protocol suggested by Struers for Ti-based alloys. The details of the grinding and polishing steps recommended by Struers are recorded in Table 6.

Table 6. The polishing procedure recommended by Struers and adopted for the studies

Process	Wheel/Cloth	Lubricant	Force	Speed	Time
Coarse Grinding	320 SIC	Water	25 N	300 rpm	1.50 min
Fine Grinding	MD-Largo	DiaPro All/Lar.9	30 N	150 rpm	5.00 min
First Polishing	MD-Mol	DiaPro Mol.3	25 N	150 rpm	2.20 min
Final Polishing	MD-CHEM	OP-S Suspension	20 N	150 rpm	1.50 min

The OP-S colloidal silica suspension for the final stage of the polishing in conjunction with the MD-CHEM polishing disk ensured that the surface of the sample was mirror finished and free of mechanical deformation. Each sample was cleaned under tap water and then in Lab Companion UC-02 Ultrasonic Cleaner for 3 min before polishing and in between each polishing step (Figure 32(a)). Each sample was then washed with alcohol and dried in air at room temperature. The sample was subsequently etched in an ESCO Ductless Fume Hood (Figure 32(b)) with Kroll's reagent. The Kroll's reagent is a dilute aqueous solution containing made up of 5ml of HNO₃ + 10ml of HF (48% concentration) + 85 ml H₂O, which is mostly used for etching titanium alloys.

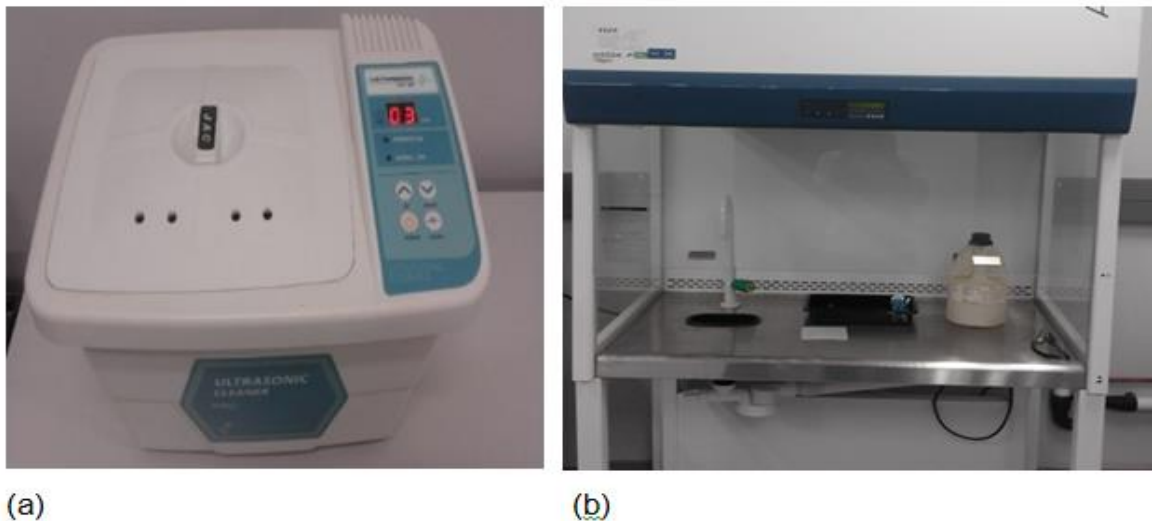


Figure 31. Lab Companion UC-02 Ultrasonic cleaner (a) and ESCO Ductless fume hood (b).

After etching, the samples were ready for microscopic examination. The ZEISS Axio Scope.A1 Optical Microscope (Figure 30) was used to analyse the single-track cross- sections. Each single-track depth, its width and its height were measured as showed in figure 33. The measurements were recorded in Microsoft Excel and used to further analyse the relationships between the process parameters and the quality of the single tracks. The cross-sections were also examined for defects.

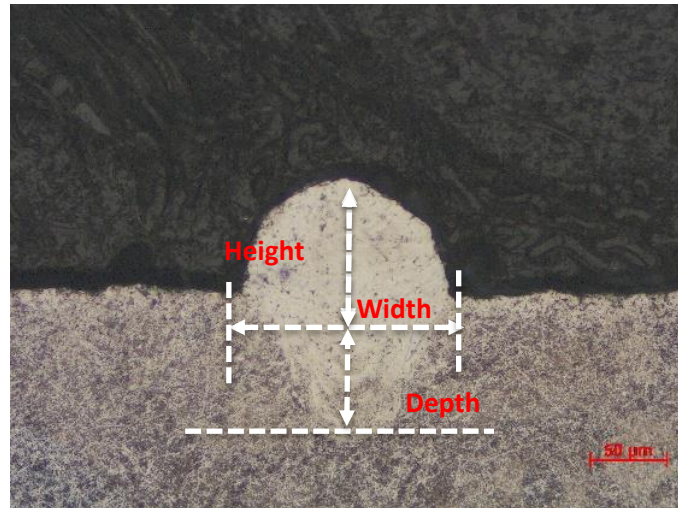


Figure 32. Cross-section of the single track.

Scanning Electron Microscope (SEM) analyses was conducted on the samples. Secondary electron (SE) and backscattered electron (BSE) imaging were employed for the analyses.

The morphology of the samples and powders was conducted in the SE and BSE mode under 15-20 kV and working distance up to 10 mm. The chemical analysis and elemental mapping of the samples to determine the distribution of the Al in the Ti matrix were conducted in the energy dispersive X-ray spectroscopy (EDS) mode. The analysis was done using a JEOL JSM-7800F SEM (Figure 34) with integrated EDS .



Figure 33. The JEOL JSM-7800F SEM used in the study

Mechanical property analysis

Microhardness tests were conducted using the FM-700 Digital Vickers Microhardness Tester from Future-Tech Corporation (Figure 35). The sample was placed on the specimen holder and the pyramid-shaped diamond indenter pressed into the surface of the material at a constant test load of 200 g for 10 seconds.

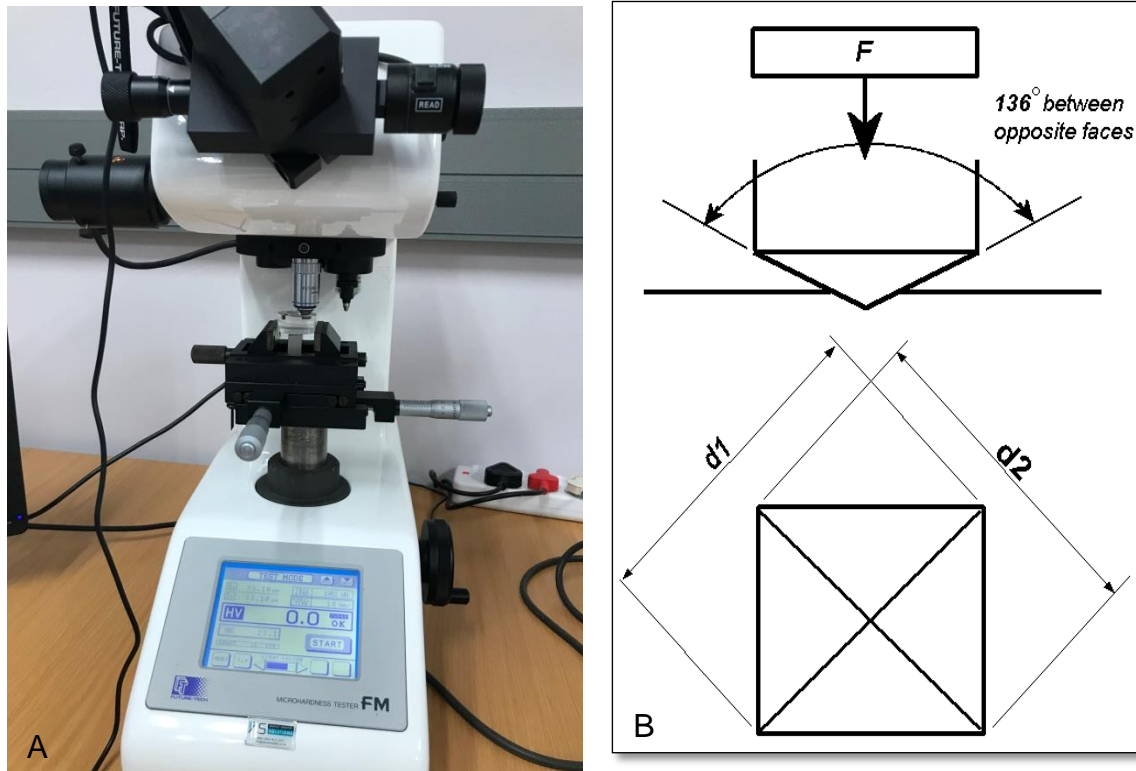


Figure 34. (A) FM-700 Digital Vickers microhardness tester (B) Indenter for Vickers hardness test

Surface Roughness Measurements

Surface roughness measurement is useful for quantifying the irregularities on the surface of a manufactured object. These irregularities can be characterised by height and depth (R_z) and interval (R_a). The surface roughness of the samples was measured with Surftest SJ-210 portable surface roughness tester from Mitutoyo Corporation (figure 35). The set parameters on the Surftest SJ-210 that were used to conduct the measurements are documented ISO 1997 standard for roughness measurements.

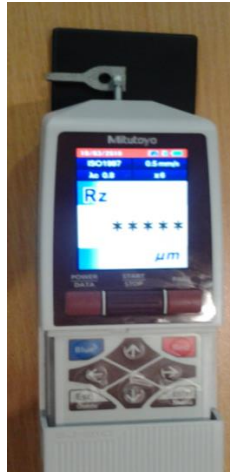


Figure 35. Surftest SJ-210 portable surface roughness tester.

3.1.2 Ti46Al Experiment - Run 1

The powder was prepared for the in-situ alloying process by mixing Ti and Al to make up 54 wt.% Ti and 46 wt.% Al. The two powders were mechanically mixed for 30 min using a wooden stick. The Ti particle size was $<45 \mu\text{m}$ and the Al powder particle sizes ranged from 20 - 45 μm . A powder layer of thickness 60 μm was deposited on the Ti6Al4V substrate. Single tracks were sintered at laser powers of 150 W and 350W and scanning speeds ranging from 0.4 – 3.4 m/s (details in table 7) with laser spot diameter of $\sim 80 \mu\text{m}$.

Table 7. Experimental process parameters of the Ti46Al Run 1.

	150 W	350 W
1	0.4 m/s	1.0m/s
2	0.6 m/s	1.2 m/s
3	0.8 m/s	1.6 m/s
4	1.0m/s	2 m/s
5	1.2m/s	2.4m/s
6	1.4m/s	2.6m/s
7	1.6m/s	2.8m/s
8	1.8m/s	3.0m/s
9	2m/s	3.2m/s
10	2.2m/s	3.4m/s

All tracks were of 20 mm length. For each scanning speed, three single scan lines were produced. A gap of 1.0 mm was used between adjacent single tracks to avoid any interaction between neighbouring scan tracks. To easily differentiate each set of scan lines a gap of 2 mm was placed between each set of single tracks produced by a particular scanning speed. The direct metal laser sintering process was followed, using the EOSINT M 280 machine from EOS GmbH. The top surface and cross-sectional analyses of the single tracks and layers were performed using the same experimental procedures followed for analysing the Ti6Al. The experiment was completed and the results were interpreted. It was decided to do a follow up experiment of the same composition (Ti46Al) to try to achieve better results.

3.1.3 Ti46Al experiment - Run 2

From the previous experimental results, a new range of process parameters for the next experiment were decided on and the same composition of Ti46Al was used with the new range of parameters. A powder layer thickness of between 50 and 60 μm was deposited on the Ti6Al4V substrate. Single tracks were sintered at laser powers of 50 W, 100 W, 150 W and 170 W and scanning speeds ranging from 0.08m/s – 2.2 m/s (details in table 8) with laser spot diameter of $\sim 80 \mu\text{m}$. The same layout was used as in the previous experiments.

Table 8. Design of experiment process parameters of the Ti46Al 2nd t run.

	170 W	150 W	100 W	50 W
1	0.1 m/s	0.08 m/s	0.4 m/s	0.08 m/s
2	0.2 m/s	0.1 m/s	0.6 m/s	0.1 m/s
3	0.3 m/s	0.12 m/s	0.8 m/s	0.12 m/s
4	0.4 m/s	0.14 m/s	1.0m/s	0.14 m/s
5	0.5 m/s	0.16 m/s	1.2m/s	0.16 m/s
6	0.6 m/s	0.18 m/s	1.4m/s	0.18 m/s
7	0.7 m/s	0.2 m/s	1.6m/s	0.2 m/s
8	0.8 m/s	0.26 m/s	1.8m/s	0.26 m/s
9	0.9m/s	0.3 m/s	2m/s	0.3 m/s
10	1m/s	0.4 m/s	2.2m/s	0.4 m/s

3.1.4 Ti46Al single layers and 3D samples experiment

From experiment 1 of the Ti6Al run and experiment 2 of the Ti46Al run , the optimum process parameters were identified as laser power of 150 W and 1.2 m/s scanning speed for the Ti6Al run and as laser power of 170 W and 0.1 m/s scanning speed from an analysis of the top surfaces and the cross-sectional surfaces.

These optimum process parameters were used to produce single layers and ten-layer cubes. Three hatch distances (60 μm , 70 μm , 80 μm) were used for the single layers and for the 3D objects a hatch distance of 70 μm was selected from the successful single layers.

The samples were cut using a CNC wire cutter for further analysis. After cutting the samples, they were mounted using a struers machine.

The following design of the experiment was used (see figure 36).

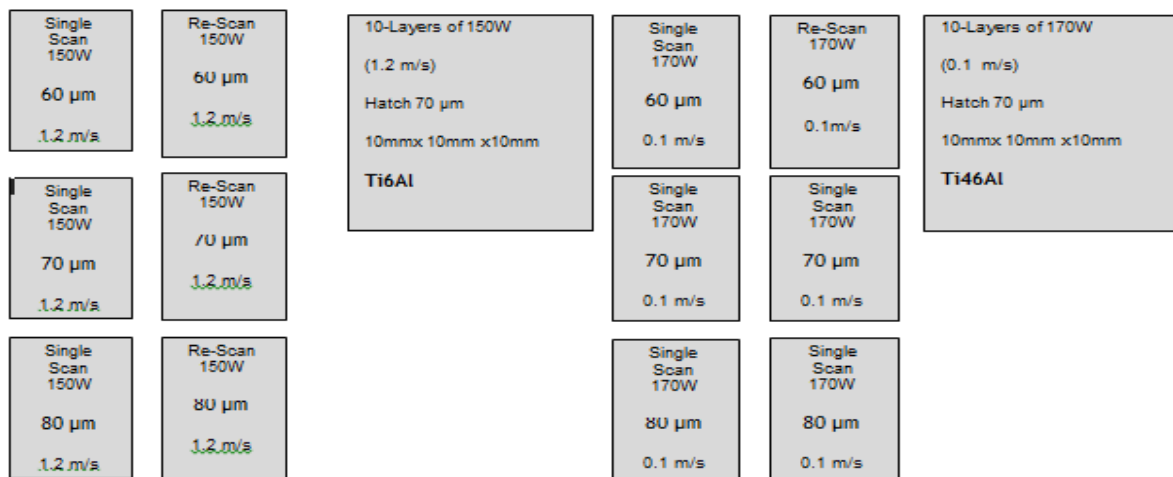


Figure 36. The design of the experiment

CHAPTER 4

Results and Discussion

4.1 Ti6Al Experiment

The results obtained from in-situ alloying blended elemental Ti and Al powders are discussed here. It is critical to ensure that the process input parameters, the machine input parameters and the material based input parameters are kept under control, as they all directly affect the results of each experiment. The same process parameters shown in Table 7 were used to identify the optimum process parameters.

The single track results are discussed first, followed by the single layer results and analysis and, finally, the 3D built parts are discussed.

4.1.1. Top surface analysis of the single tracks

Figure 37 shows representative optical micrographs of the top surface view of single tracks at different parameter settings. It was observed that at 150 W laser power and 1.2 m/s scanning speed, the single tracks were continuous (Figure 37A). At 350 W laser power and 2.4 m/s, the single tracks were irregular (Figure 37B). At 350 W laser power and 3.4 m /s scanning speed, the single tracks showed the balling effect (Figure 37C).

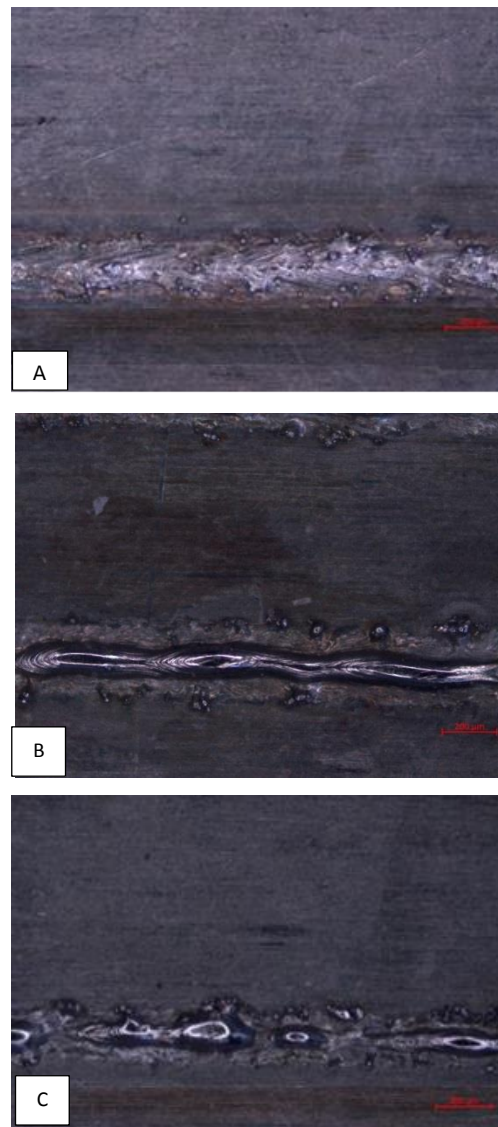


Figure 37. Top surface optical micrographs of Ti6Al single tracks (a) Continuous track at 150 W and 1.2 m/s (b) Irregular track at 350 W and 2.4 m/s and (c) Balling track at 350 W and 3.4 m/s

A process map for continuous and discontinuous single tracks was generated based on the top surface analysis. A laser power and scanning speed range of the continuous, Irregular and balling single tracks was mapped (Figure 38). As mentioned above, at 150 W laser power and 1.2 m/s scanning speed, the single tracks were continuous. The single tracks were discontinuous and irregular at 150 W laser power and 0.6 m/s – 1 m/s, 1.6 m/s – 2.2 m/s scanning speeds, as well as at 350 W laser power and 1 m/s – 2.6 m/s scanning speeds. The single tracks were discontinuous with the balling effect at 350 W laser power and 2.8m/s – 3.4m/s scanning speeds.

The balling effect occurs when the surface tension breaks the continuous molten pool into individual droplets (Figure 37 B & C). At low laser power, the molten pool exists at lower temperatures, the surface tension coefficient, as well as the melt viscosity, increase and lead to pre-balling and/or balling (Yadroitsev, 2009).

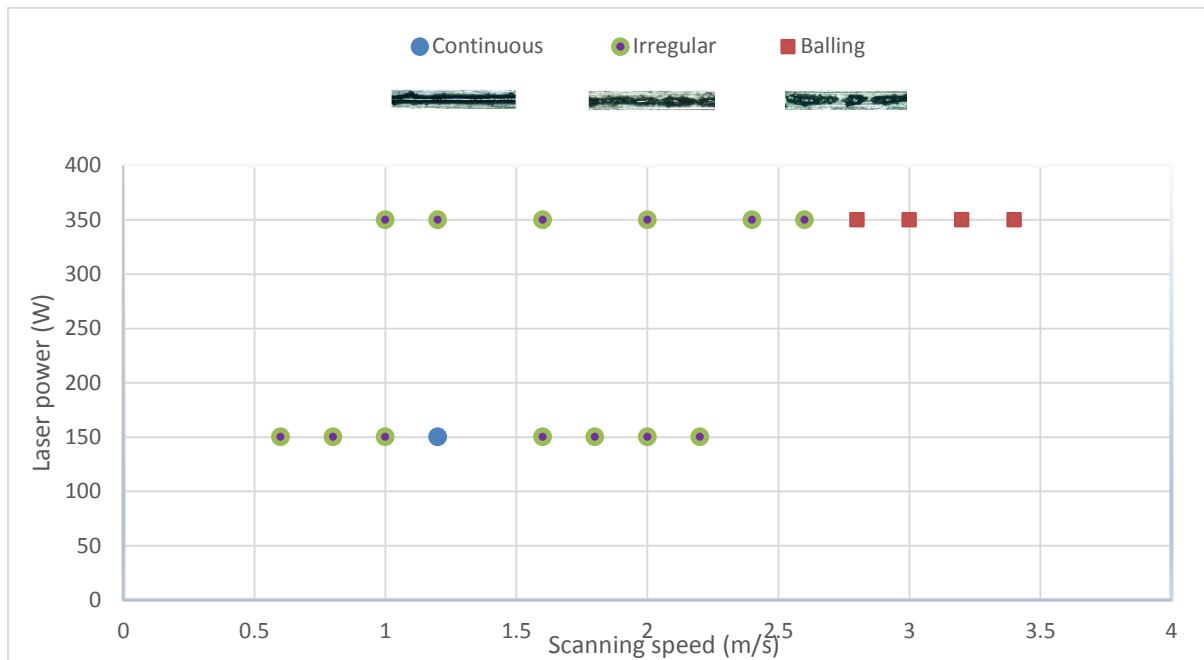


Figure 38. Process map for Ti6Al single tracks

Analysis of the characteristics of the DMLS single tracks showed that the process has a threshold character: there are “stability zones” where the track is continuous and “instability zones” where the track is discontinuous. Instabilities appear at lower scanning speed in the form of distortions and irregularities, and, on the contrary, excessively high speed gives rise to the balling effect (Yadroitsev *et al.*,2010).

A high-quality stable single track, i.e. continuous track with stable geometrical characteristics, without the balling effect and irregularities and adequate penetration depth for providing strong metallurgical bonding between the substrate and the track, is the first step in finding an algorithm for optimal DMLS process parameters (Yadroitsev *et al.*,2010). The features of a track depend on laser power, scanning speed, powder layer thickness, substrate material, physical properties and morphology of the powder used. The properties of a part produced by SLM

technology depend strongly on the properties of each single track and each single layer (Yadroitsev *et al.*, 2007).

During the DMLS process, the laser beam energy is absorbed by the powder particles, which causes a rapid rise of the surface temperature of the powder particles, resulting in surface melting of the powder particles. This is followed by heat flow towards the core of the powder particles to form a molten pool. The amount of liquid formed and the characteristics of the molten pool depend on the temperature. The latter is dependent on the thermal properties of the alloy, the laser energy input (laser power, spot size and scanning speed) and the thickness of the deposited powder layer. Consequently, the laser energy density determines the hydrodynamic movement of the molten liquid and the final geometry of the solidified liquid (Fischer *et al.*, 2003).

It was observed that the molten pool forms droplets on the powder bed at the edge of the tracks as shown in Figure 39. Droplets are caused by molten liquid build-up ahead of the laser spot, during the laser melting process. The advancing molten liquid has a tendency to spill over onto the powder particles ahead of the laser beam and pinch off onto the powder bed as spatter particles (Matilainen *et al.*, 2015).

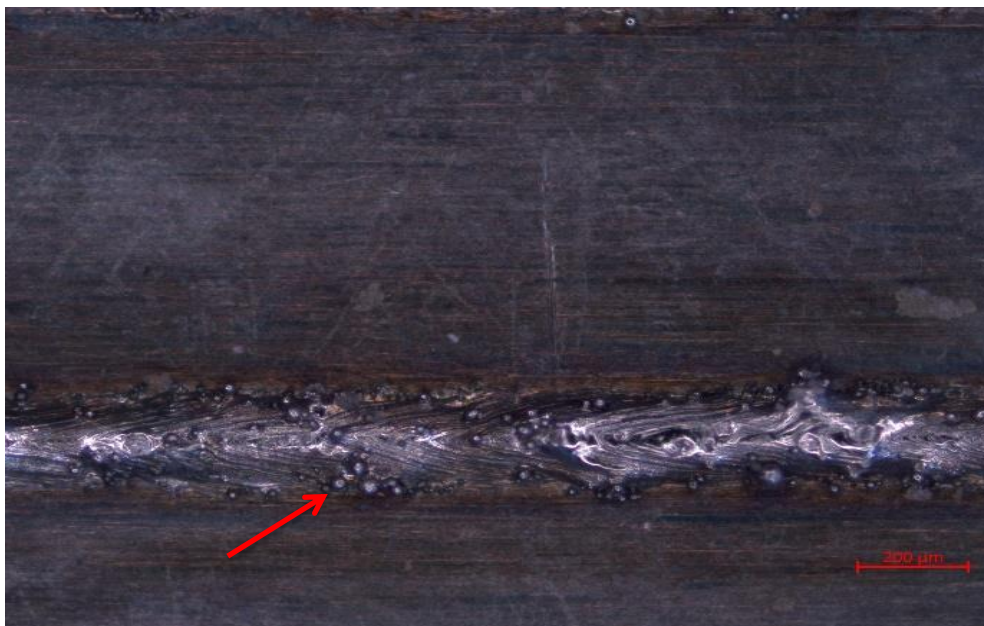


Figure 39 . Droplets next to a single track of Ti6Al and satellites on the track surface

Figure 39 also shows satellites, indicated by the arrow. Satellites are particles sticking to the surface of the scan tracks and they may be formed by two main

mechanisms: melt spattering and partial powder melting in the peripheral zone of the laser spot. Since the energy transferred to the spatter particles is not enough for them to be melted and incorporated into the bulk material they stack to the surface of the build parts (Yadroitsev *et al.*, 2013).

Satellites are surface defects and may be associated with thermo physical properties of the material, particle morphology characteristics of the powder, deposition and spreading of the powder, powder layer thickness, laser radiation energy, laser scanning speed, and melt hydrodynamics (Yadroitsev *et al.*, 2010). The formation of satellites, surrounding the track and having metallurgical contact with the track, could result in the formation of pores in 3D parts and increase surface roughness (Mumtaz & Hopkinson, 2010).

If the scanning speed decreases, the time of irradiation is increased and it results in a higher energy input and irregular tracks are formed because the heat-affected zone becomes larger, more powder is involved and tracks tend to have satellites or dislodged sections that form during solidification (Rai, 2007). An example of this was found with a number of process parameters as shown in Figures 44,45 and 46. Figure 40 shows the relationship between laser power, scanning speed and width of the single track.

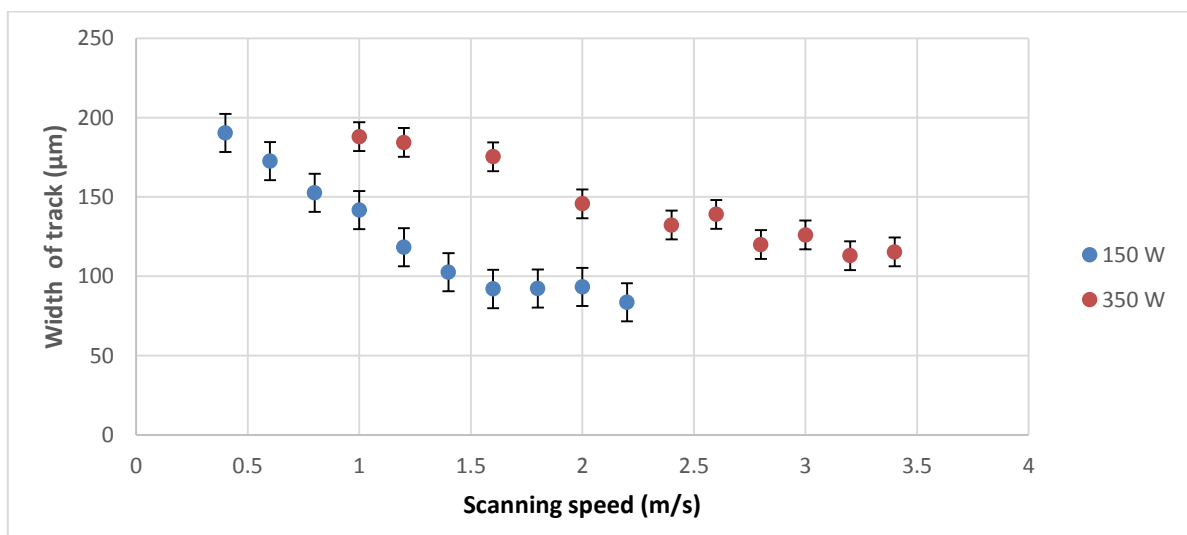


Figure 40. The width of the Ti6Al single tracks at different scanning speeds and laser power.

From Figure 40 it was noted that, as the scanning speed increases, there is a reduction in track width at the same laser power.

Figure 41 shows the relationship between the linear energy density, the laser power and the scanning speed.

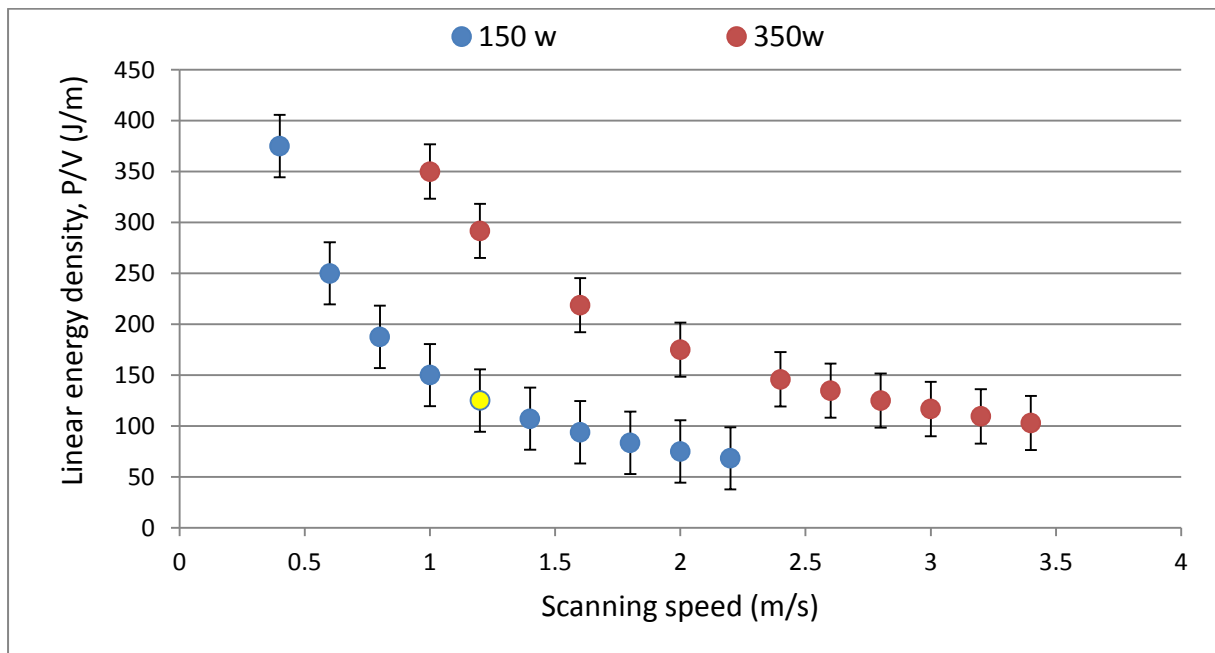


Figure 41. Linear energy density of Ti6Al single tracks at different scanning speeds and laser power.

From Figure 41 it is noted that an increase in the scanning speed results in reduction of the linear energy density. A reduction in the linear energy density leads to a reduction of the temperature in the molten pool. The lowered temperatures at the molten pool produce molten fluid of higher viscosity, which obstructs the free movement of the powder particles. The high viscous liquid forms semi-discontinuous tracks known as pre-balls and balling.

On the other hand, high-energy input increases the temperature of the molten pool with a subsequent production of a large amount of liquid phase with low viscosity, which enhances the flow of the molten pool. At low scanning speeds, increased heat conduction promotes heating of the substrate and the powder, thus creating conditions for involvement of new material into the fusion process. In Figure 41, the corresponding linear energy density for achieving continuous single tracks is at 125 J/m (shown in yellow).

4.1.2 Cross-sectional analysis of the single tracks

After completing the microscopic analyses of the top surfaces of the single tracks, the samples were sectioned for further analysis to determine the re-melted depth and height of the single tracks. During the in-situ DMLS process, if the selected process parameters lead to sufficient laser energy density, to melt the powder and penetrate into the previous layer, bonding between the substrate (or previous layers) and the next layer takes place. Figure 42 shows cross sectional views of the single tracks penetration to the substrate.

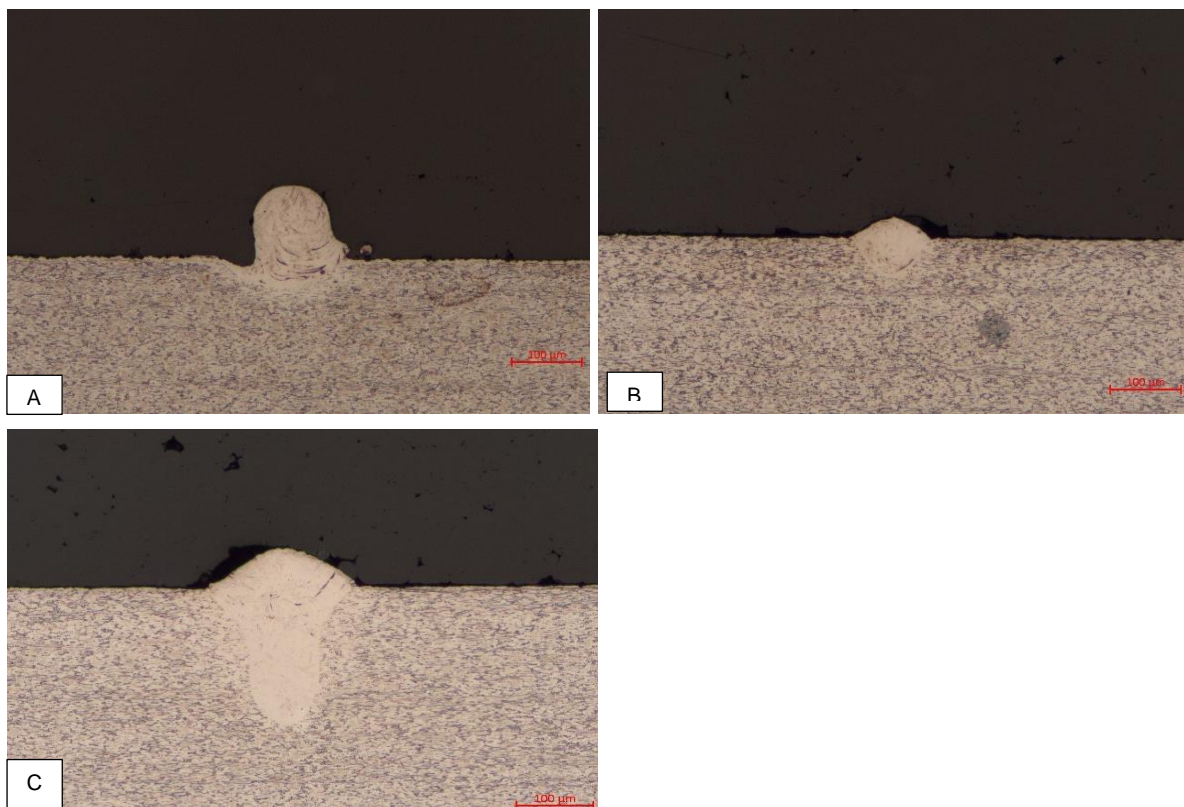


Figure 42. Cross-sectional views of the level of penetration into the substrate of the Ti6Al laser sintered single tracks.

The cross-section of the single tracks can be divided into 3 cases as presented in Figure 42: A) poor penetration, B) good penetration (conduction mode) and C) deep penetration (keyhole mode) into the substrate. Eagar & Tsai, (1983) described the cross-section of a solidified molten pool formed in the conduction mode as being semi-circular (U-shaped) and keyhole mode as V-shape. During the conduction mode, the laser produces sufficient energy density to melt the powder and penetrate into the previous layer (in the case of a single track, the substrate acts as the previous layer) forming a strong bond between the substrate and the single track.

In the keyhole mode, the laser energy density is sufficient to cause evaporation of the metal leading to vapour formation (formation of a plasma). The vapour formation causes laser energy absorption deeper into the substrate and subsequently it drills into the substrate. When the combination of the processing parameters in DMLS exceeds the conduction mode threshold, the mode of thermal conduction in the molten pool changes from semi penetration to the keyhole mode, as illustrated in Figure 42C.

According to Rai, (2007), the collapse of the vapour cavity formed during the fusing process could leave a pore in the wake of the laser beam, which would contribute to pore defects in the final product. Reducing the linear energy density too far below the conduction mode threshold through too high scanning speed leads to insufficient re-melting depths and long molten pools as shown in Figure 43A. At high laser power, excessive energy input can lead to a keyhole mode resulting in deep re-melting of the substrate and pores inside the molten pool, and this would contribute to porosity in the final product (see Figure 42C).

From the above, it is clear that at optimal DMLS process parameters the single tracks will be continuous, defect free and the penetration will resemble a U shape cross-sectional profile as shown in Figure 42B.

In this investigation, the analysis of the cross-sections showed that the re-melted depth decreased with an increase in scanning speed (Figure 43).

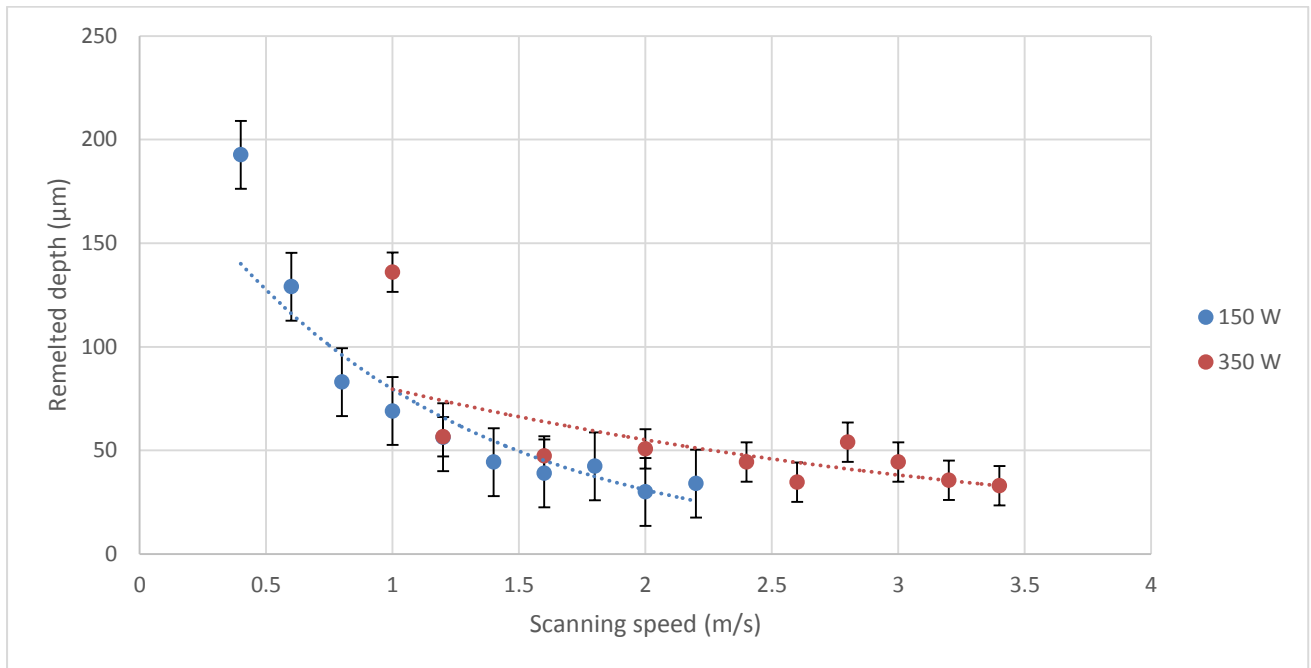


Figure 43. Re-melted depth of Ti6Al single tracks at different scanning speeds and laser power

Figure 44 presents cross-sectional profiles of Ti6Al single tracks with poor penetration into the substrate.

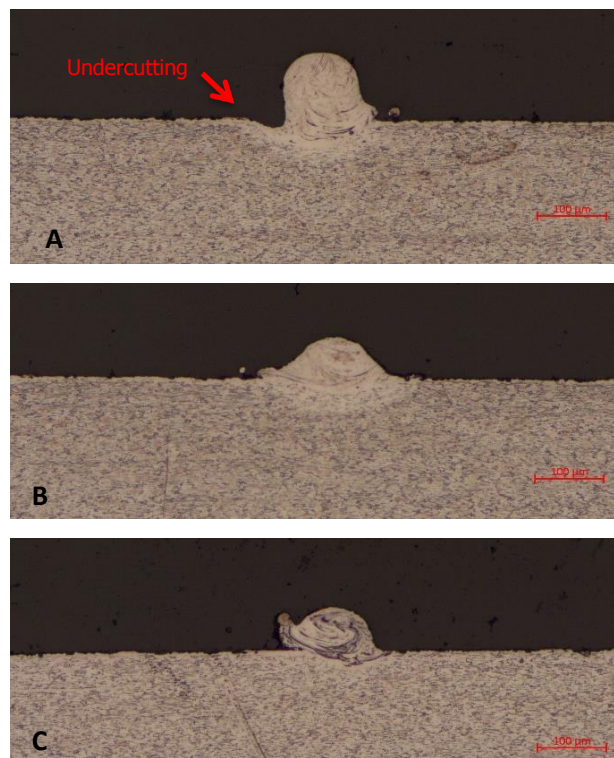


Figure 44 Cross sectional profiles of the Ti6Al single tracks with poor penetration (a) 150W at 2.2m/s (b) 350W at 1.8m/s (c) 350W at 2.6m/s

At 150 W laser power with 2 m/s - 2.2 m/s scanning speeds and at 350 W laser power and 1.6 m/s – 3.4 m/s scanning speeds, poor penetration of the single tracks into the substrate was observed (Figure 44). This is the effect of too high scanning speeds, resulting in insufficient time for the laser beam to melt the powder completely and penetrate into the substrate. At 150 W laser power with 2 m /s - 2.2 m /s scanning speeds, the humping effect was also observed (Figure 44A). Fabbro (2011) defines “humping” as “the occurrence of a prominent weld seam with negative strong undercuts, composed of solidified large swellings of quite ellipsoidal shape, separated by smaller valleys”.

In figure 45, it was observed that the cross sections of the single tracks at 150W laser power and corresponding scanning speed of 0.4m/s – 1m/s and 350W at scanning speed 1m/s – 1.2m/s showed a deep penetration with a V-shaped profile.

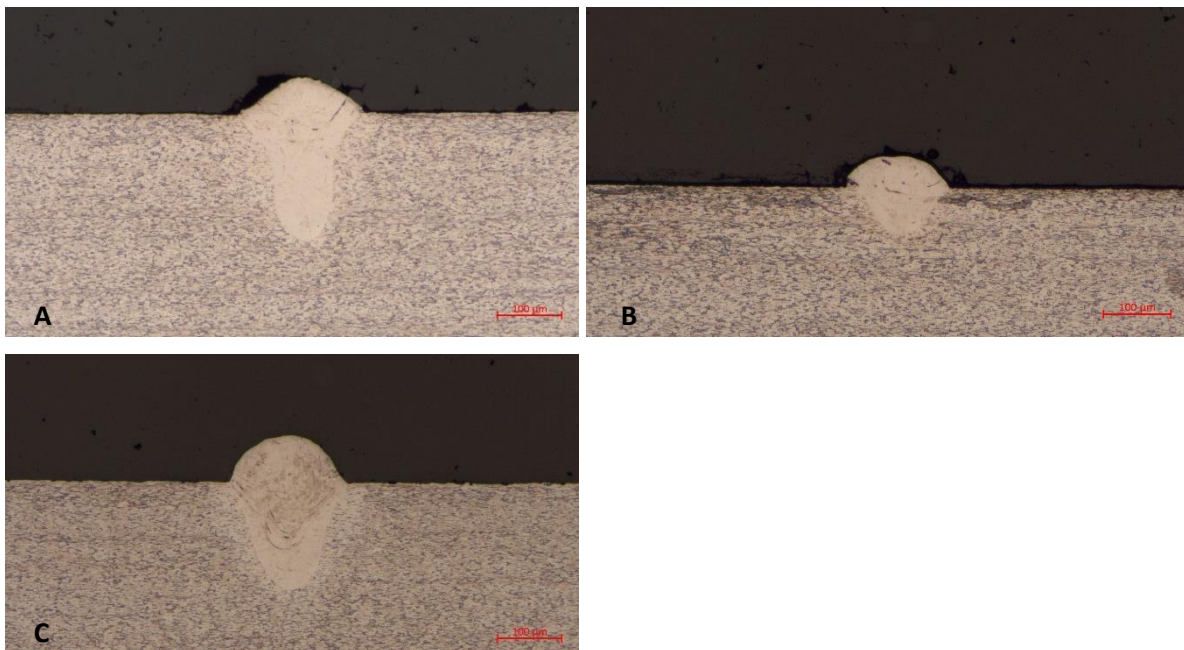


Figure 45. Cross sectional profiles of Ti6Al single tracks with deep penetration (V-shape) profiles (a) 150W at 0.4m/s (b) 150W at 0.8m/s (c) 350W at 1m/s

At laser power 150W and scanning speeds 1.4m.s – 1.8 m/s humping and undercutting was noted on the single tracks (Figure 46).

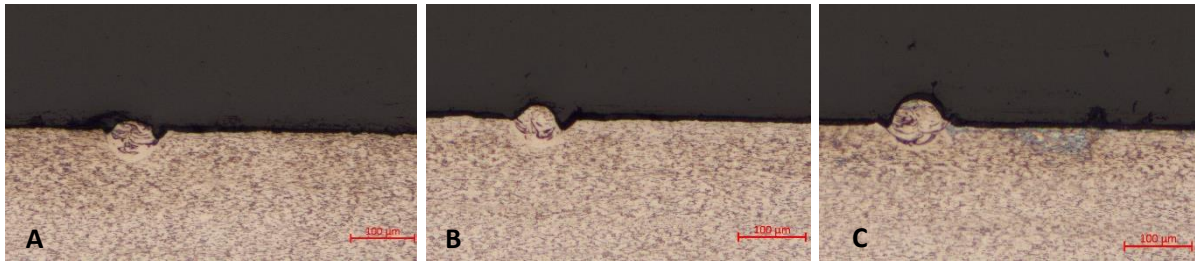


Figure 46. Cross sectional profiles of Ti6Al single tracks with humping and undercutting (a) 150W at 1.4m/s (b) 150W at 1.6m/s (c) 150W at 1.8m/s

The cross-section of the single track formed at 150 W laser power of and 1.2 m/s scanning speed of reveals a semi-circular (*U*-shape) profile as shown in Figure 47. This confirms that the process was performed in the conductive mode, which leads to good bonding between the tracks and the substrate, and indicates optimum processing parameters.

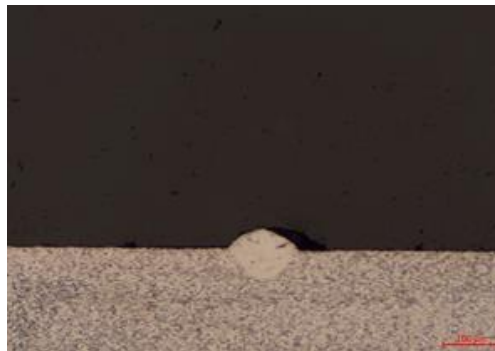


Figure 47. Cross-sectional profile of a Ti6Al single track, formed at optimal process parameters of 150 W at 1.2 m/s, with a U-shape profile

4.1.3 Top Surface Analysis of Ti6Al single layers

Superposition of the various tracks and layers leads to the manufacturing of 3D objects. The quality of the individual sets of single tracks determines the morphology and mechanical properties of the final object. Key parameters such as laser power, spot diameter, scanning speed, hatch distance, powder layer thickness and powder characteristics have a decisive effect on the structural integrity and surface morphology of DMLS parts.

From the analysis of the single tracks, optimum process parameters at a laser power of 150 W and scanning speeds of 1.2 m/s were selected to produce single layers from Ti6Al powder. To investigate the influence of scanning strategy on single layer morphology at different hatch distances of 80 µm, 90 µm and 100 µm, two different types of layers were produced: single scanned

and rescanned layers. For the rescanned single tracks each track was scanned twice before moving to next track. These were analysed using an optical microscope and a Scanning Electron Microscope (SEM).

Figure 48 shows the results obtained with the selected hatch distances, which allowed for single track overlapping and permitted the formation of single layers. 80 h, 90 h and 100 h represent the hatch spacing.

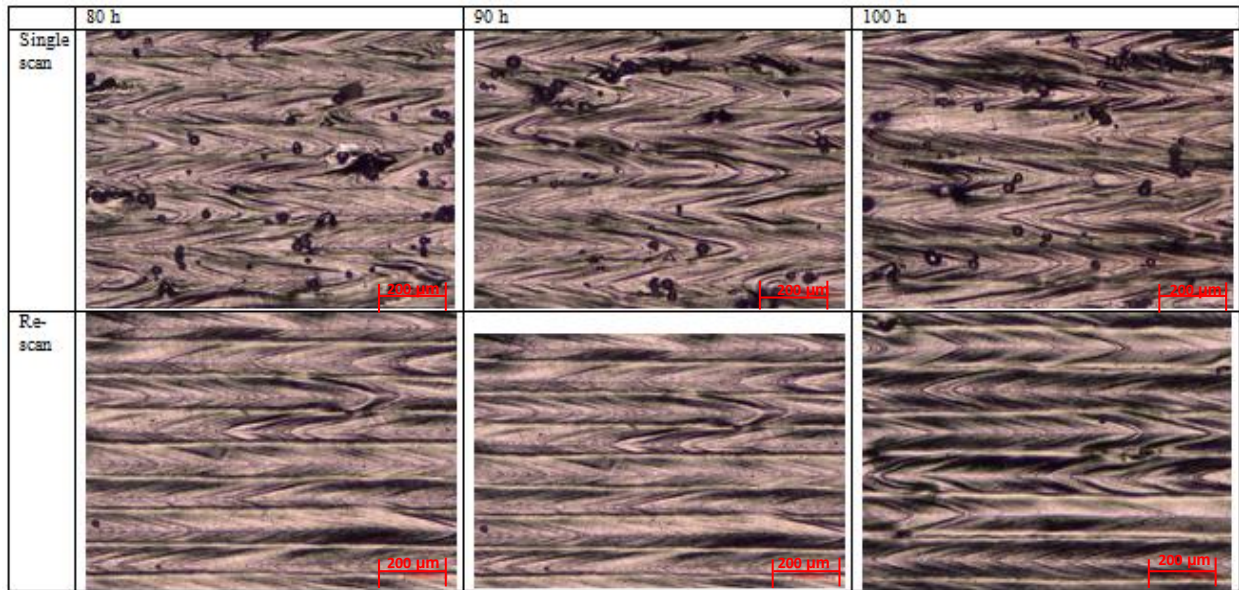


Figure 48. Optical micrographs of the top surfaces of Ti6Al single layers at 150 W and 1.2 m/s at hatch distances 80 μm , 90 μm and 100 μm .

Figure 49 shows secondary electron micrographs of Ti6Al samples at different hatch distances (80 μm , 90 μm and 100 μm) and shows a comparison between the single scanned and rescanned layers. It was observed that the layers overlapped completely forming metallurgical bonding with fully dense solidified surfaces at all the selected hatch distances.

Satellites were observed on the solidified surfaces after the single scanned process at 90 μm . The satellites were considerable reduced after the rescanning process. These results confirm what was noted earlier in theory; that rescanning of DMLS layers increase the surface quality (Kruth *et al.*, 2010).

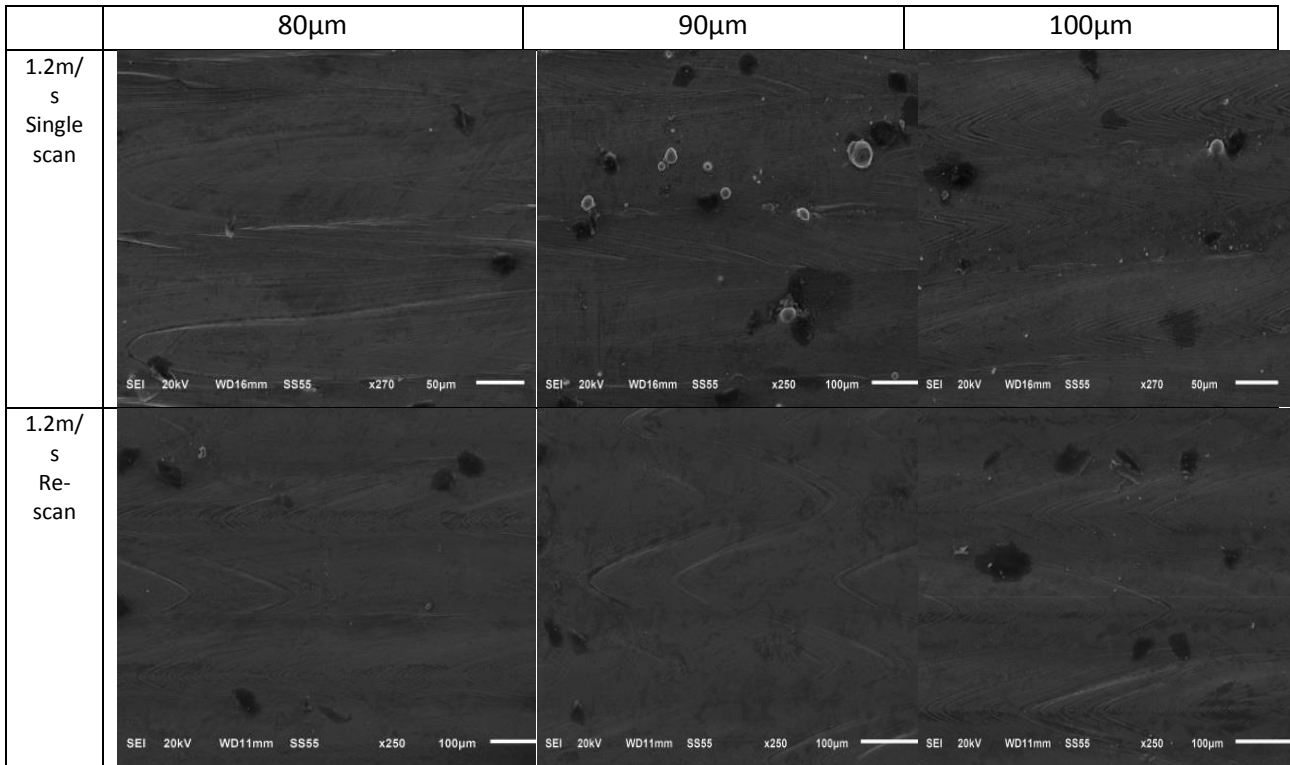


Figure 49. SEM secondary electron micrographs of Ti6Al samples at different hatch distances for single scanned and rescanned layers built at 150 W and 1.2 m/s.

4.1.4 Cross-sectional analysis of single layers

Figure 50 presents optical micrographs of cross-sections of Ti6Al showing a comparison between the single scanned and rescanned layers. The cross-sectional examination revealed that the Ti and Al powder particles melted completely, because there no visible unmelted particles on the cross-sectional views.

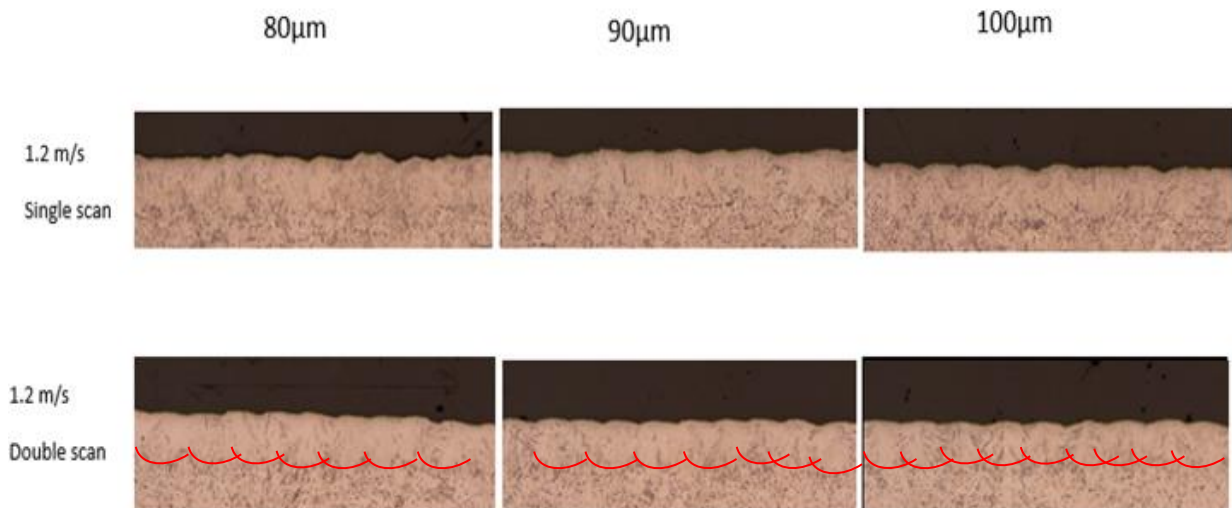


Figure 50. Optical micrographs of cross-sectional views of Ti6Al built at 150 W laser power and 1.2 m/s scanning speed for single and re-scan at hatch distances 80 μm, 90 μm and 100 μm.

EDS elemental mapping analysis was conducted to verify the distribution of the Al in the Ti matrix in the cross-sectional areas of the Ti6Al samples. These results are shown in Figure 51.

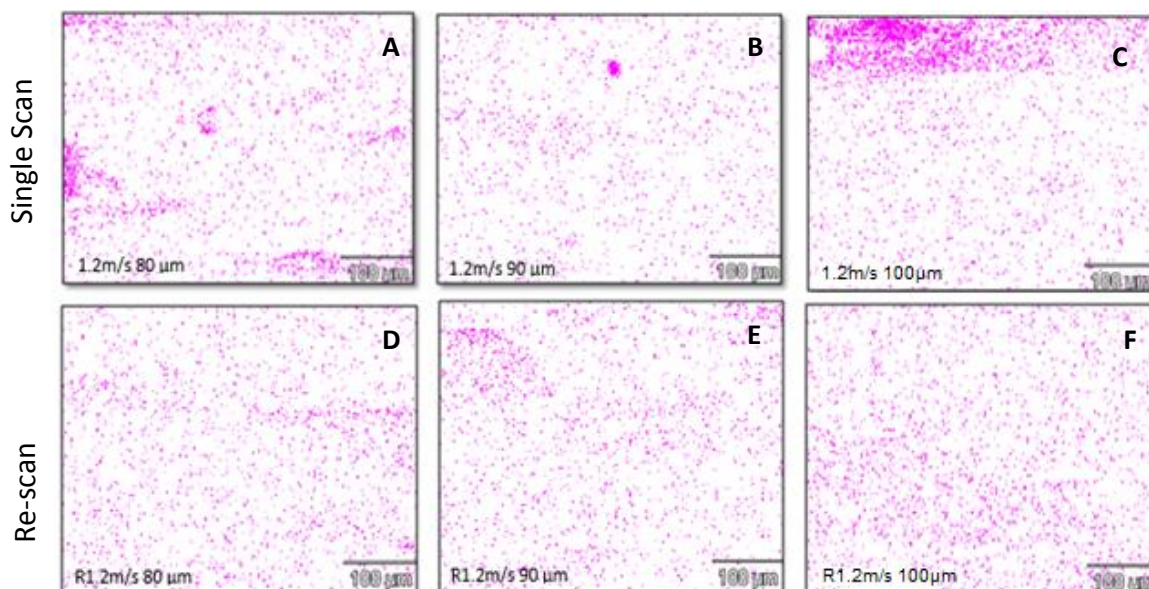


Figure 51. EDS Al elemental mapping of single scanned and rescanned areas on the cross-sections of the Ti6Al samples built at different hatch distances and at 150 W laser power and 1.2 m/s scanning speed.

The results given in Figure 51 indicate that, even though all powder particles melted completely, Al was not evenly distributed in the Ti matrix for single scanned layers. There were areas rich in Al that were random distributed in the Ti matrix. However, rescanning had improved the homogeneity of the alloy in the Al rich areas as can be seen in Figure 51F. The rescanning strategy enhances homogeneity of the in situ alloyed material, by ensuring that the laser melts all powder particles and satellites. The process of rescanning helps to homogenise the Al distribution in the Ti. During the rescanning process, the previously rough surface enhances laser radiation absorption. The increase in laser absorptivity due to the rougher surface leads to an increase in temperature and more prominent flow of the molten pool. The increased temperature and the more prominent liquid flow causes the Al concentrated zones to homogenise (Bergström *et al.*, 2007).

The difference in hatch distance seems not to have had any significant effect on the Al distribution in the Ti. All the samples demonstrated a similar level of Al distribution at each hatch distance (80 μm , 90 μm and 100 μm) in the Ti alloy matrix at a given constant laser speed (see Figure 54).

SEM area scans observations of the DMLS samples demonstrated complete melting of the alloy. The average concentration of Al in the alloy was 4.98 wt.%, showing a loss of 1.2 wt.% of Al.

The observed loss of Al and effect of energy input on *in situ* alloying of a Ti and Al powder mixture can be explained with the differences in the material properties of the two metals. These properties are stipulated in table 9

Table 9. Material properties of Ti and Al

Properties	Ti	Al
Density	4500 kg/m ³	2710 kg/m ³
Specific heat capacity	528 J/(kg.K)	900 J/(kg.K)
Melting point	1668 °C	660 °C
Thermal conductivity	17 W/(m.K)	205 W/(m.K)
Latent heat of fusion	435 kJ/kg	398 kJ/kg

From Table 9 it is clear that Al has a higher specific heat and a higher thermal conductivity than Ti, which results in Al absorbing more laser radiation than Ti. The effect of the lower melting point of Al (660 °C) compared to that of Ti (1668 °C) explains why there was a significant loss of Al compared to Ti; because Al will reach the melting point before the Ti and in the process Al could evaporate. The density of Al is only 60% of that of Ti, which will cause Al to move to the top and Ti to sink to the bottom in the molten pool. This brings Al to the top surface and even closer to the laser beam and promotes an accelerated melting and loss of Al as more radiation is experienced by Al.

4.2 Ti46Al Experiment Run 1

4.2.1. Top surface analysis of the single tracks

Figure 52 shows top surface optical micrographs of the Ti46Al single tracks. It can be noted that the single tracks have irregularities and they are discontinuous for both the 150W and the 350W range of scanning speeds. The single tracks became more unstable, and irregular with increasing scanning speed and laser power as seen from Figure 52A to 52F. Satellites are noted on the single tracks throughout the scanning speed range 150W (0.4m/s – 2.2m/s) and 350 (1m/s – 3.4m/s) and they are shown in red arrows in Figure 52.

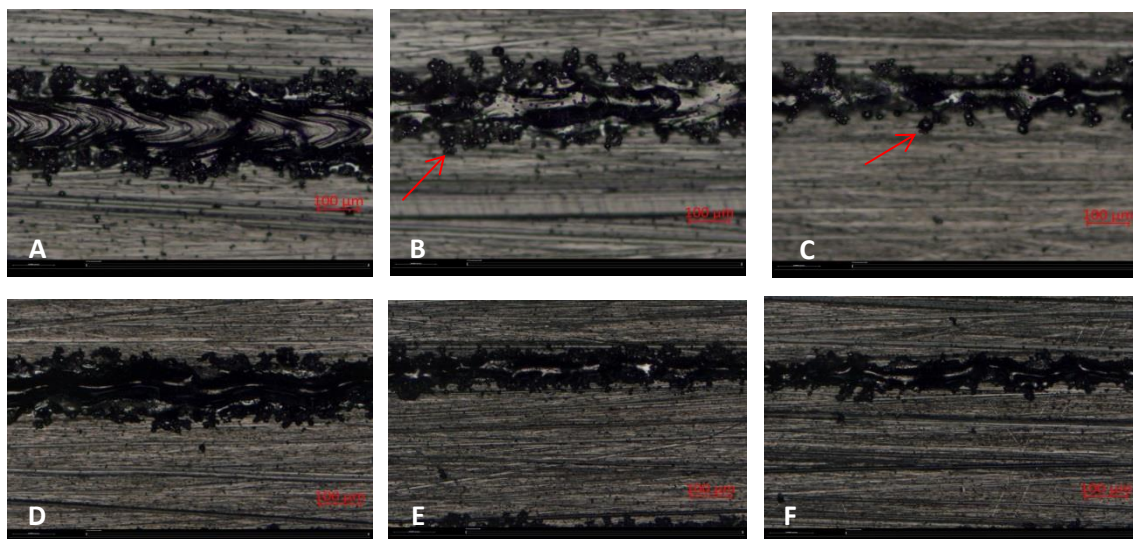


Figure 52 Top surface optical micrographs of Ti46Al single tracks (A) 150W at 0.4m/s (B) 150W at 0.8m/s (C) 150W at 2m/s (D) 350W at 1m/s (E) 350W at 2m/s (F) 350W at 3.4m/s

A process map was generated based on the top view analysis of the single tracks and it is shown in Figure 53. All the single tracks throughout the 150W and 350W laser power range were irregular and discontinuous.

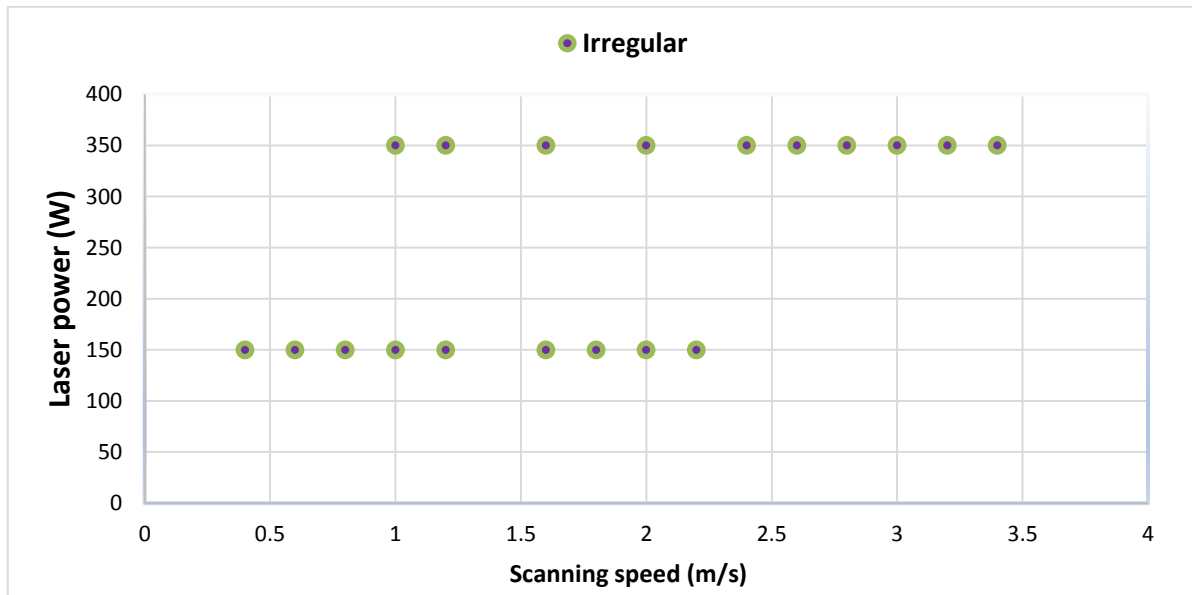


Figure 53. Process map for Ti6Al single tracks produced at laser powers from 150 W to 350 W with varied scanning speeds (0.4–3.4 m/s).

In a plotted coloration between the track width, the laser power and the scanning speed, it is noted that; as the scanning speed increases, there is a general reduction in tracks width at the same laser power (Figure 54). Yadroitsava *et al.* (2015) experimented with different powder layers of Ti6Al4V and reported a reduction in tracks width with increasing scanning speed; the result of the current experiment shown in figure 54 are in agreement with what was reported.

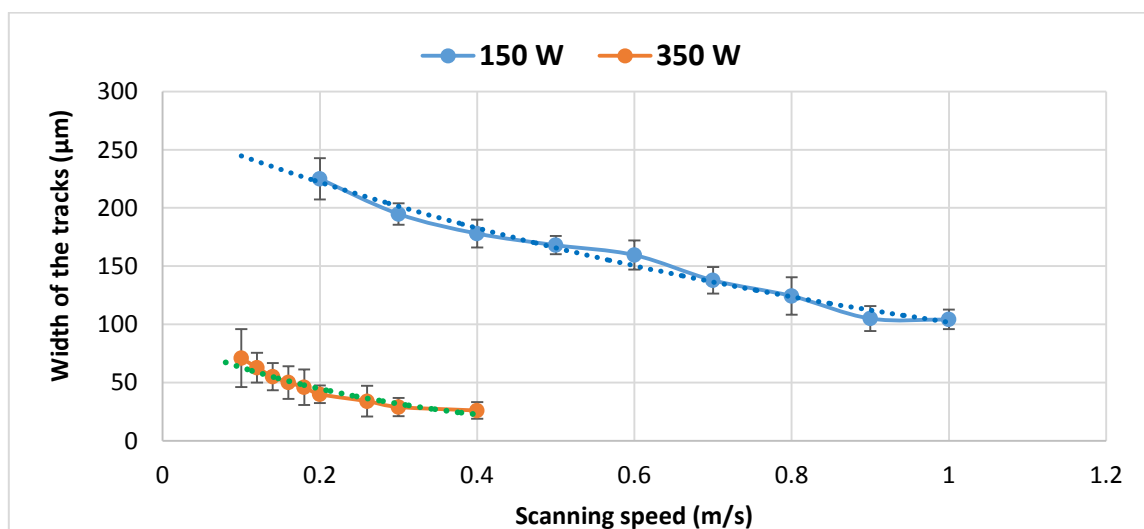


Figure 54. The width of the Ti6Al single tracks at different scanning speeds and laser power

Figure 55 shows a plotted coloration between the linear energy density, the laser power and the scanning speed. It was noted that an increase in the scanning speed reduces the linear energy density.

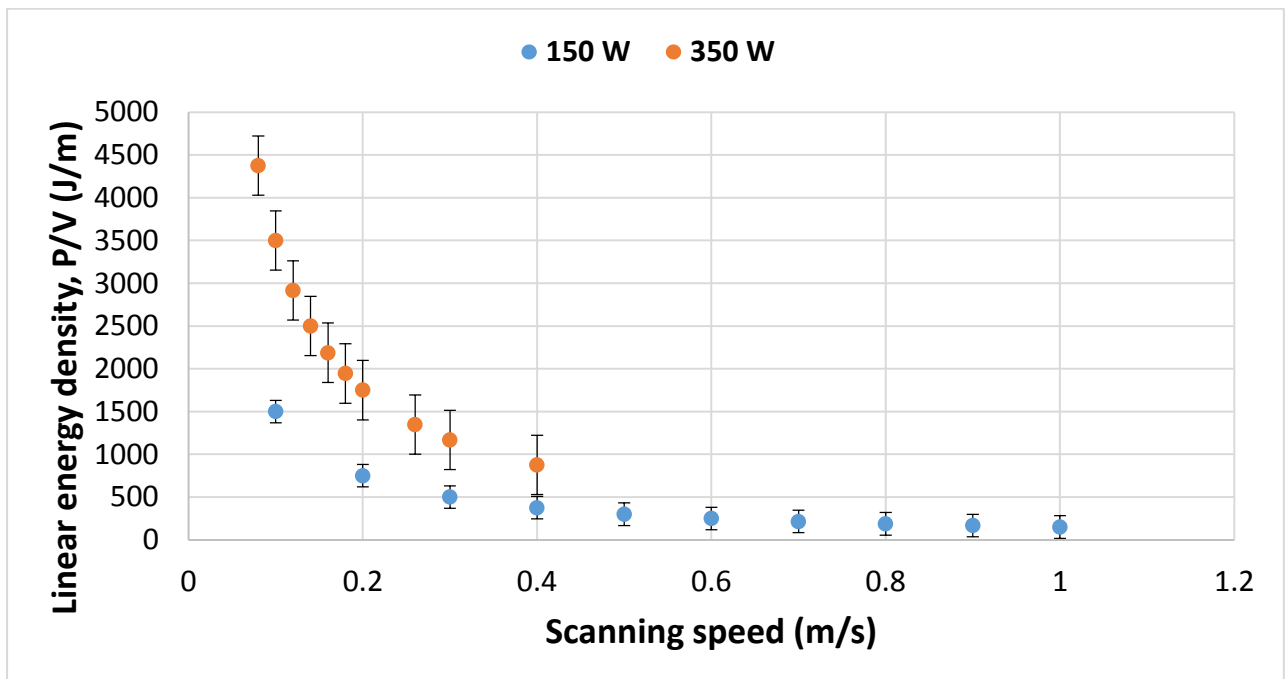


Figure 55. Linear energy density of the Ti46Al single tracks versus scanning speed

4.2.2. Cross sectional analysis of the Ti46Al single tracks

In figure 56, the cross sectional profiles of the single tracks range from lack of penetration to partial penetration on the 150W (0.4m/s – 2.2m/s). The analysis of the cross-sections shows that for the chosen layer thickness and the chosen scanning speeds range, the laser power of 150 W could not produce sufficient energy to penetrate the substrate, even though the powder particles could be melted, there is only small metallurgical bonding of the single tracks to the substrate.

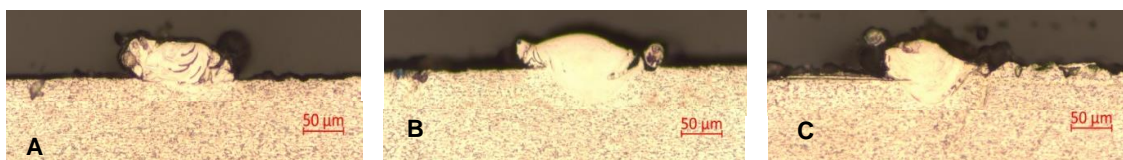


Figure 56. Cross-sectional view of single laser tracks at a laser power of 150 W (A) 0.6m/s (B) 2m/s (C) 2.2m/s

At laser power 350W, scanning speed 1m /s to 2.6m /s, the single tracks show a poor penetration to the substrate in figure 57. The poor penetration is caused by the reduced radiation time in the molten pool caused by the increase in the scanning

speed. The molten pool temperature is reduced, and the single-track penetration to the substrate is reduced.

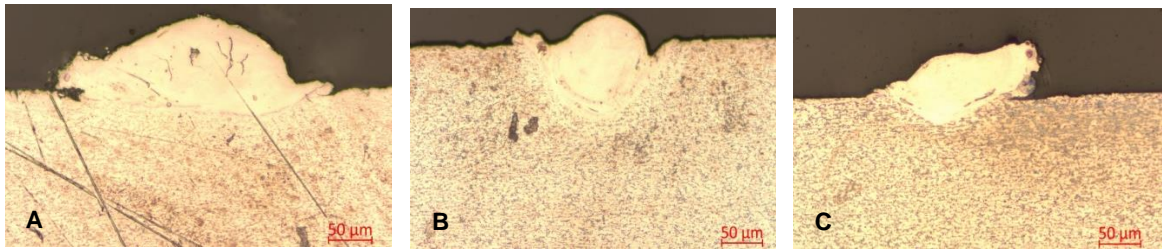


Figure 57. Cross-sectional view of single tracks at a laser power of 350 W (A) 1m/s (B) 1.2 m/s (C) 2.6m/s

At Laser power 350W and scanning speeds 2.8m/s to 3.4 m/s respectively, the single tracks are irregular shaped and have very poor penetration to no penetration at all to the substrate (figure 58).



Figure 58. Cross-sectional view of single laser tracks at a laser power of 350 W (A) 2.8m/s (B) 3m/s (C) 3.4m/s

Figure 59 shows the graphical representation of the relationship between the remelted depths of the single tracks with scanning speed. It was noted that the remelted depth decreased with an increase in scanning speed.

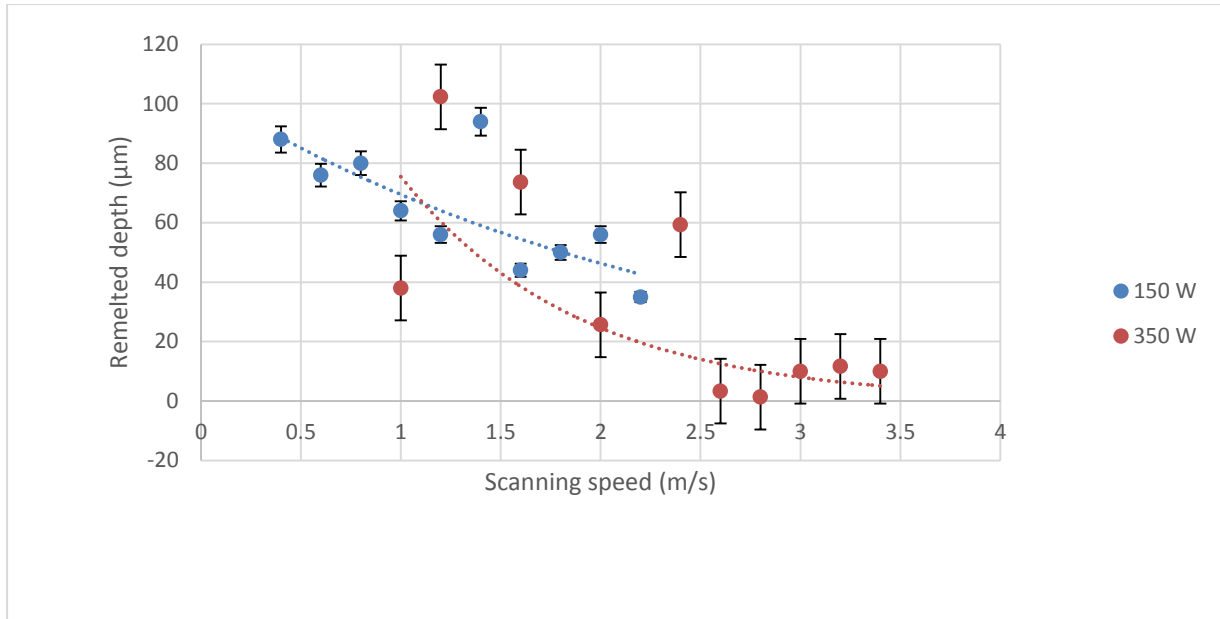


Figure 59. Remelted depth of Ti46Al single tracks versus scanning speed and laser power

4.3 Ti46Al Experiment run 2

4.3.1. Top surface analysis of the single tracks

Figure 60 shows the top surface view of Ti46Al single tracks. The analysis was done at laser powers 50W, 100W, 150W and 170W. Satellites were noticed on the boundaries of all the single tracks. Continuous single tracks were noted at laser power 150W (0.08m/s), 150W (1m/s) and at 170W (0.1m/s) shown in Figure 60.

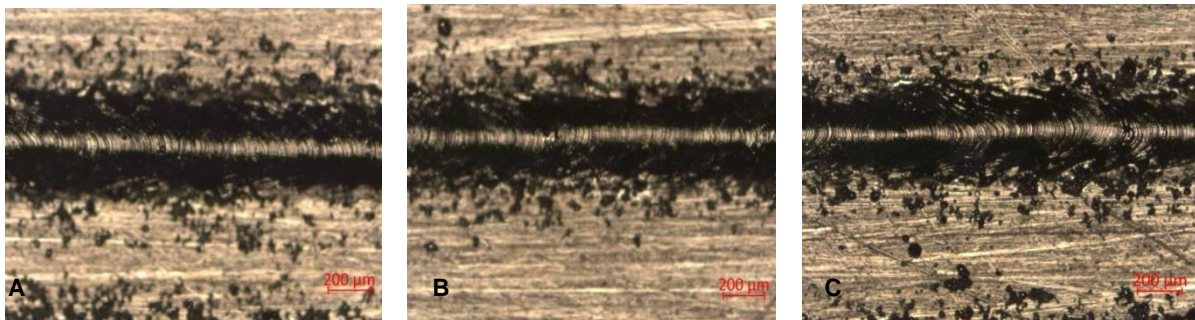


Figure 60. Top view of Ti46Al single tracks (A) 150W 0.08m/s (B) 150W 0.1m/s (C) 170W 0.1m/s

Figure 61 shows that at laser power 170W and scanning speed 0.2m/s to 1m/s respectively, the single tracks were discontinuous and irregular shaped. It is also noted that; the width of the single tracks became smaller as the scanning speed increased.

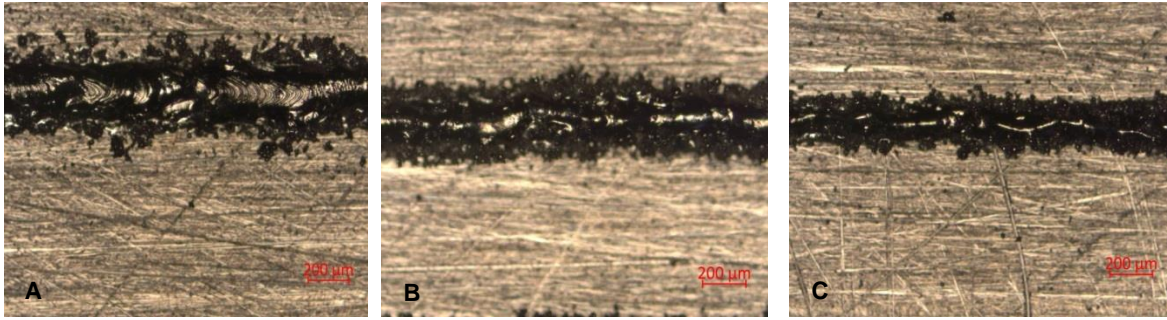


Figure 61. Top view of Ti46Al single tracks (A) 170W 0.2m/s (B) 170W 0.4m/s (C) 170W 0.7m/s

Figure 62 shows that at laser power 150W and scanning speed 0.12m/s to 0.4m/s respectively, the single tracks are irregular

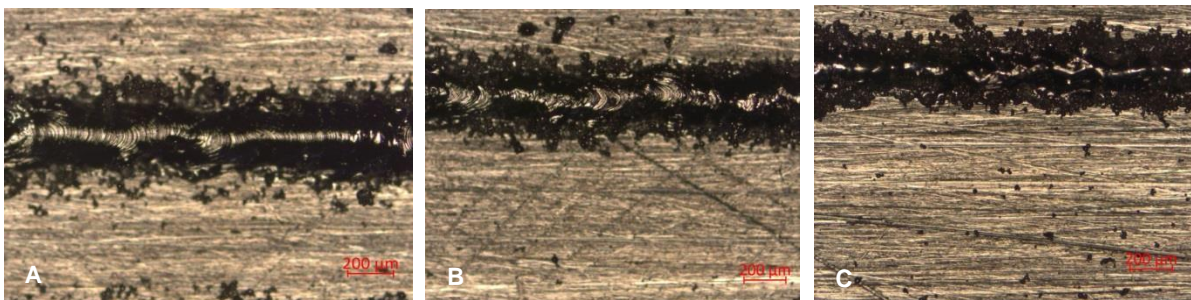


Figure 62. Top view of Ti46Al single tracks (A) 150W 0.12m/s (B) 150W 0.18m/s (C) 150W 0.26m/s

Figure 63 shows that at laser power 100W, the single tracks are irregular, there are visible satellites and they are discontinuous. At scanning, speeds 0.4m/s to 2m/s respectively the single tracks are irregular and at 2.2 m/s balling.

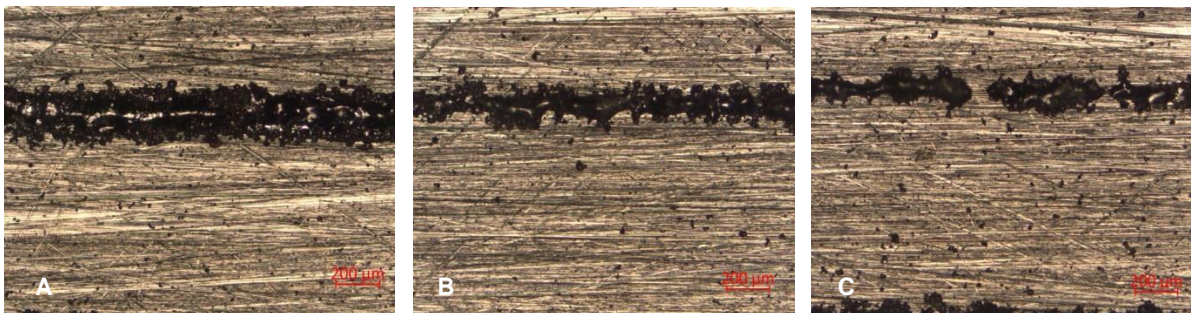


Figure 63. Top view of Ti46Al single tracks (A) 100W 0.4m/s (B) 100W 1.8m/s (C) 100W 2.2m/s

Figure 64 shows at laser power 50W and scanning speed 0.08m/s to 0.4m/s respectively, the single tracks are distorted and irregular.

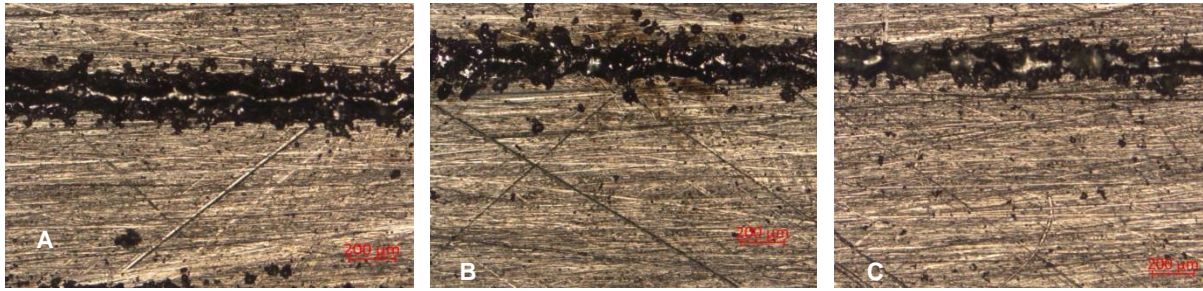


Figure 64. Top view of Ti46Al single tracks (A) 50W 0.08m/s (B) 50W 0.18m/s (C) 50W 0.4m/s

In figure 65, the process map shows that there were no other continuous single tracks achieved throughout the set parameters range except the three identified (Figure 65 in a red colour). The single tracks were mostly irregular and a few had the balling effect.

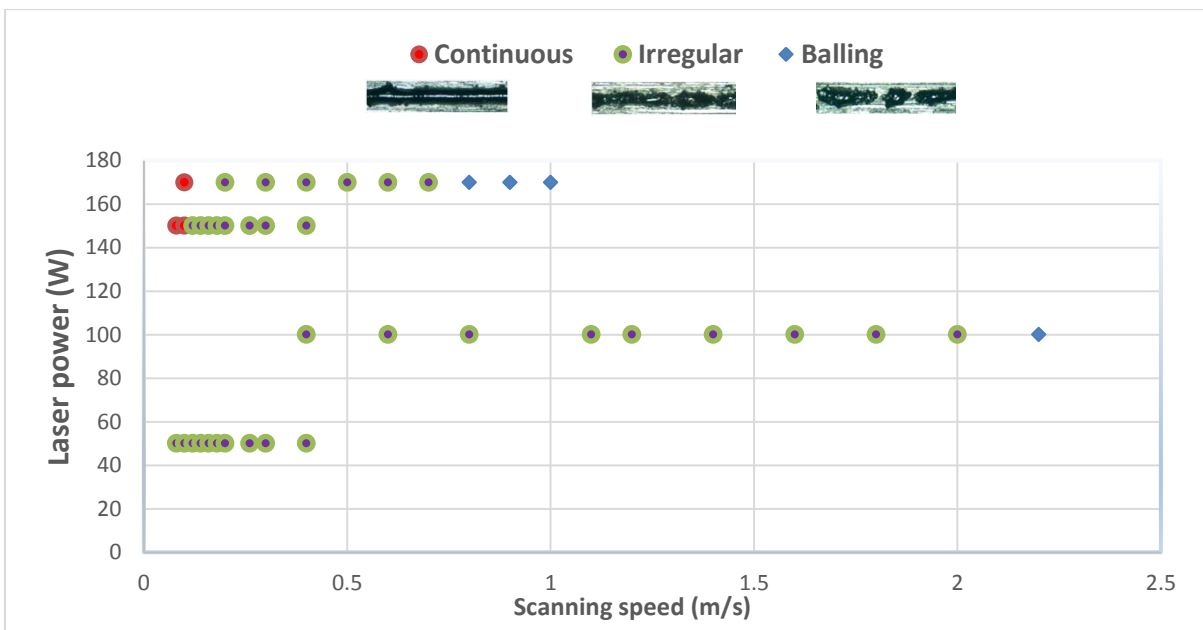


Figure 65. Process map for Ti46Al single tracks produced at laser powers from 50W, 100W, 150 W and 170 W with varied scanning speeds

Figure 66 shows the coloration between the width of the Ti46Al single tracks and the scanning speeds. It can be noted that as the scanning speed increases, the width of the track decreases. However, 50W shows an undefined coloration and differs from each single track.

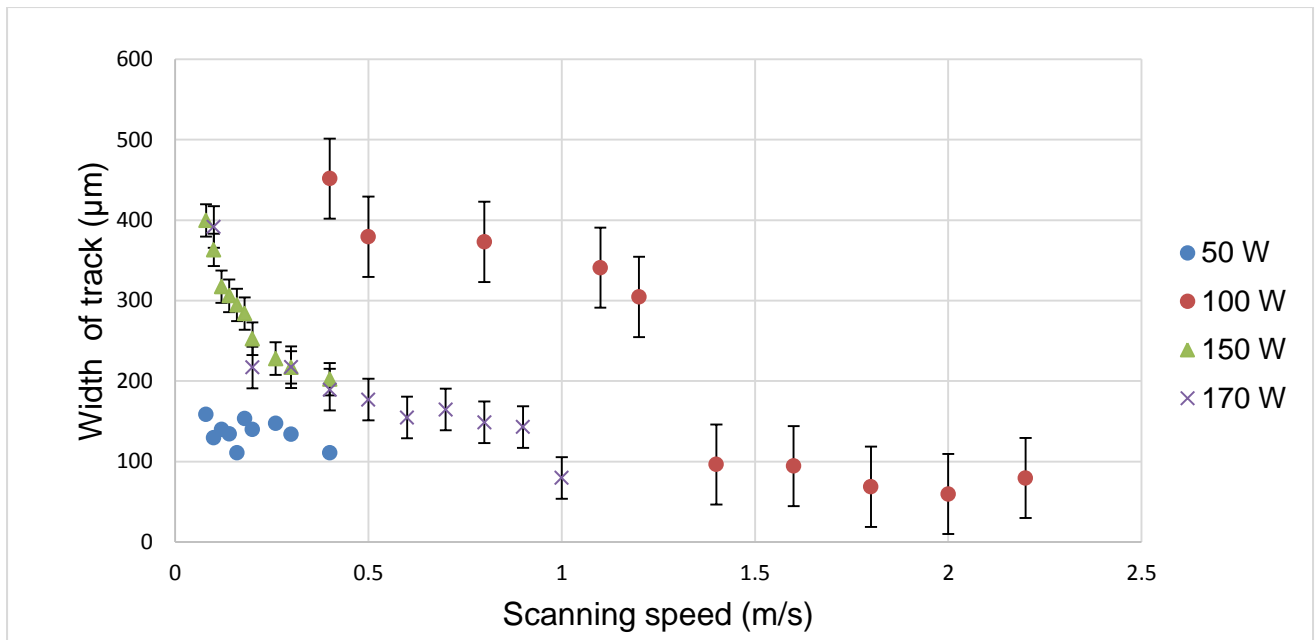


Figure 66. Width of Ti46Al single tracks versus the scanning speed

4.3.2. Cross sectional analysis of the single tracks

Figure 67 shows that at laser power 170W and scanning speed 0.1m /s, the cross section shows a profile of a semi-circle (U-Shape), even though the profile would identify a possible good process parameter on a single track, it is not a perfect U-shape as anticipated (Figure 67A). The rest of the cross sectional profiles of the single tracks from 0.2m/s to 0.7m/s show a deep penetration profile (Figure 67B). As the scanning speed increases from 0.8m/s to 1m/s, the single tracks penetration into the substrate is poor (Figure 67C). When the scanning speed increases it results to insufficient molten pool time and the laser beam is unable to melt the powder completely and penetrate the single track into the substrate. From 0.2m/s, there is deep re-melting of the substrate, and it can be attributed to the high laser power and excessive energy input at 170W. The excessive energy leads to a keyhole mode, however as the scanning speed increases at 0.8m/s to 1m/s there is poor penetration and insufficient re-melting of the substrate.

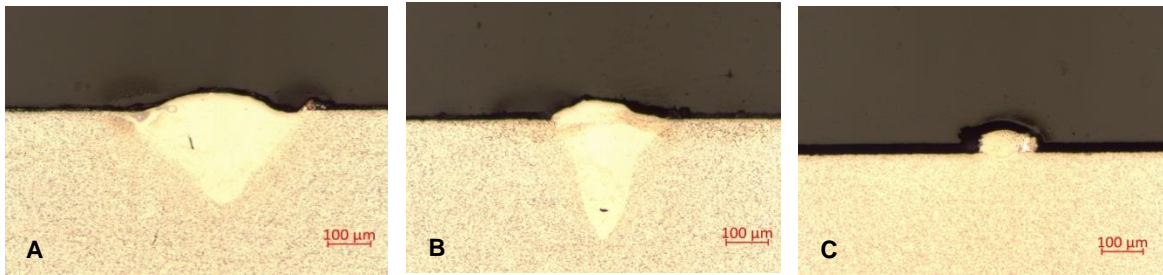


Figure 67. Cross-sectional view of Ti46Al single tracks at a laser power of 170 W (A) 0.1m/s (B) 0.2m/s (C) 1m/s

Figure 68 shows that, at laser power 150W, the cross sectional profiles of all the single tracks follow a deep penetration. The cross sectional analysis at 150W Scanning speeds 0.1m/s and 0.2m/s show a different view from the anticipated view for continuous single tracks (Figure 60). The deep penetration of all the single tracks at 150W can be attributed to the high laser power and the relatively low scanning speeds selection. As previously explained that, slow scanning speed results in the time of irradiation of the molten pool increases, it results in a higher energy input, and irregular tracks are formed because the heat-affected zone becomes larger.

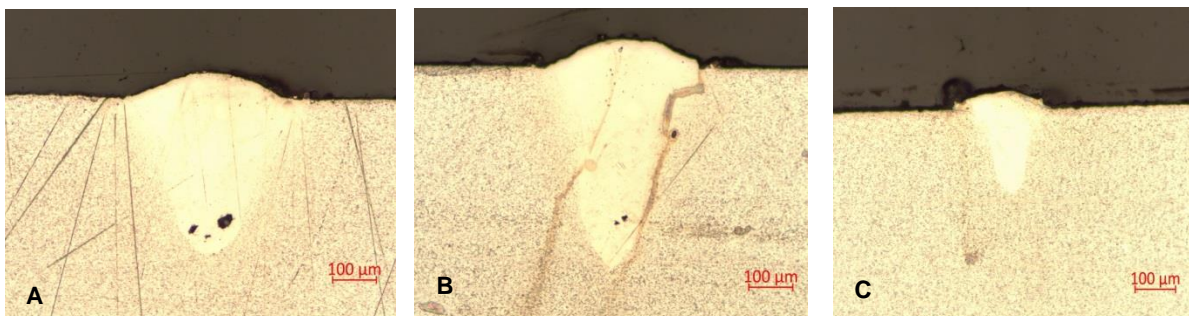


Figure 68 Cross-sectional view of single laser tracks at a laser power of 150 W (a) 0.08m/s (b) 0.1m/s (c) 0.4m/s

Figure 69A and 69B shows that at laser power 100W and 0.4m/s to 1.2m/s scanning speeds respectively, the cross sectional profiles show deep penetration. At 100W and 1.4m/s to 2.2m/s, there is poor penetration between the single tracks and the substrate (Figure 69C).

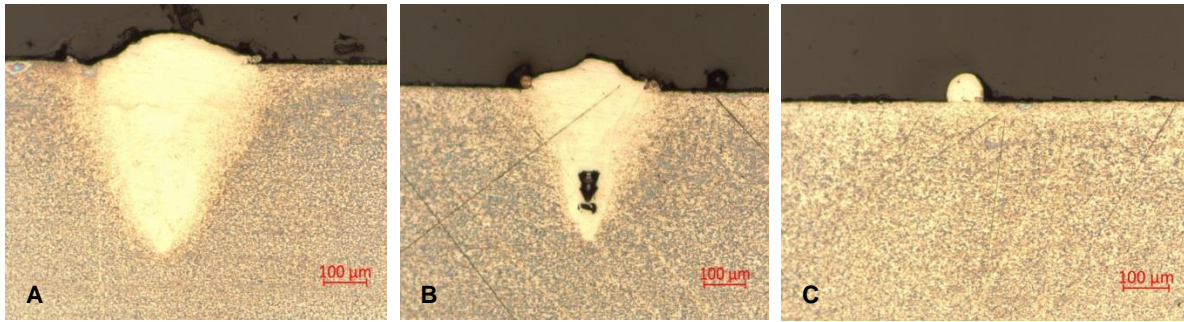


Figure 69 Cross-sectional view of Ti46Al single laser tracks at a laser power of 100 W (a) 0.6m/s (b) 1.2m/s (c) 2.2 m/s

Figure 70 shows that at laser power 50W and 0.08m/s to 0.4 m/s scanning speeds respectively, the single tracks have poor penetration to the substrate. The laser power is not sufficient to re-melt and penetrate the substrate.

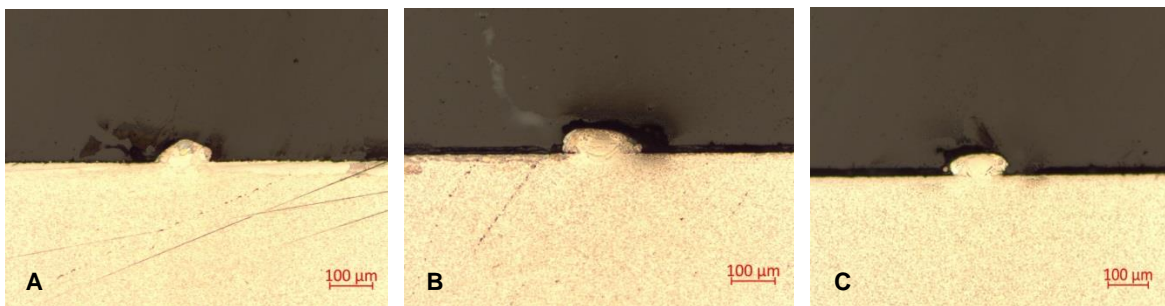


Figure 70. Cross-sectional view of single laser tracks at a laser power of 50 W (a) 0.14m/s (b) 0.18m/s (c) 0.4 m/s

4.4 Ti6Al and Ti46Al single layers and 3D samples Experiment

Single layers were built from the identified optimum process parameters and thereafter-3D samples were built as shown in figure 71. Figure 71A shows 150 W and 1.2 m/s runs and figure 71B shows 170 W and 0.1 m/s runs.

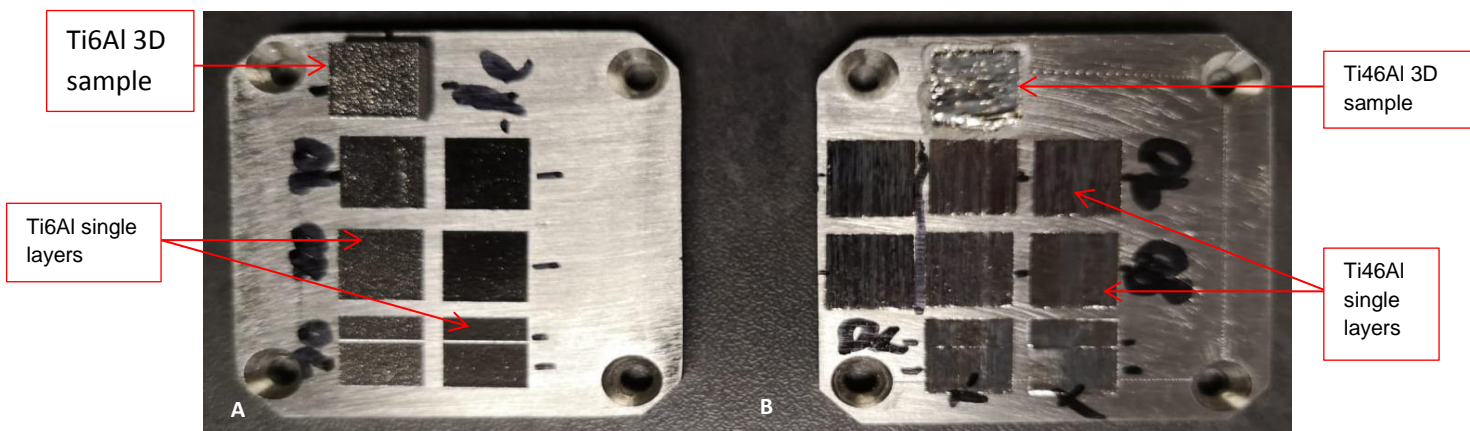


Figure 71. Single layers and 3D samples (A) Ti6Al (B) Ti46Al.

4.4.1. Top surface analysis of the single layers

Using the optical microscope, top surface views of the single layers were captured. In Figure 72, it can be noted that all three selected hatch distances at 150W and 1.2m/s show complete overlapping of the single tracks and form a single layer. It can also be seen that as the hatch distance increases, there were visible satellites appearing in between the single tracks especially at hatch distance 90 μm . However, after rescanning, the satellites were melted and the homogeneity was improved.

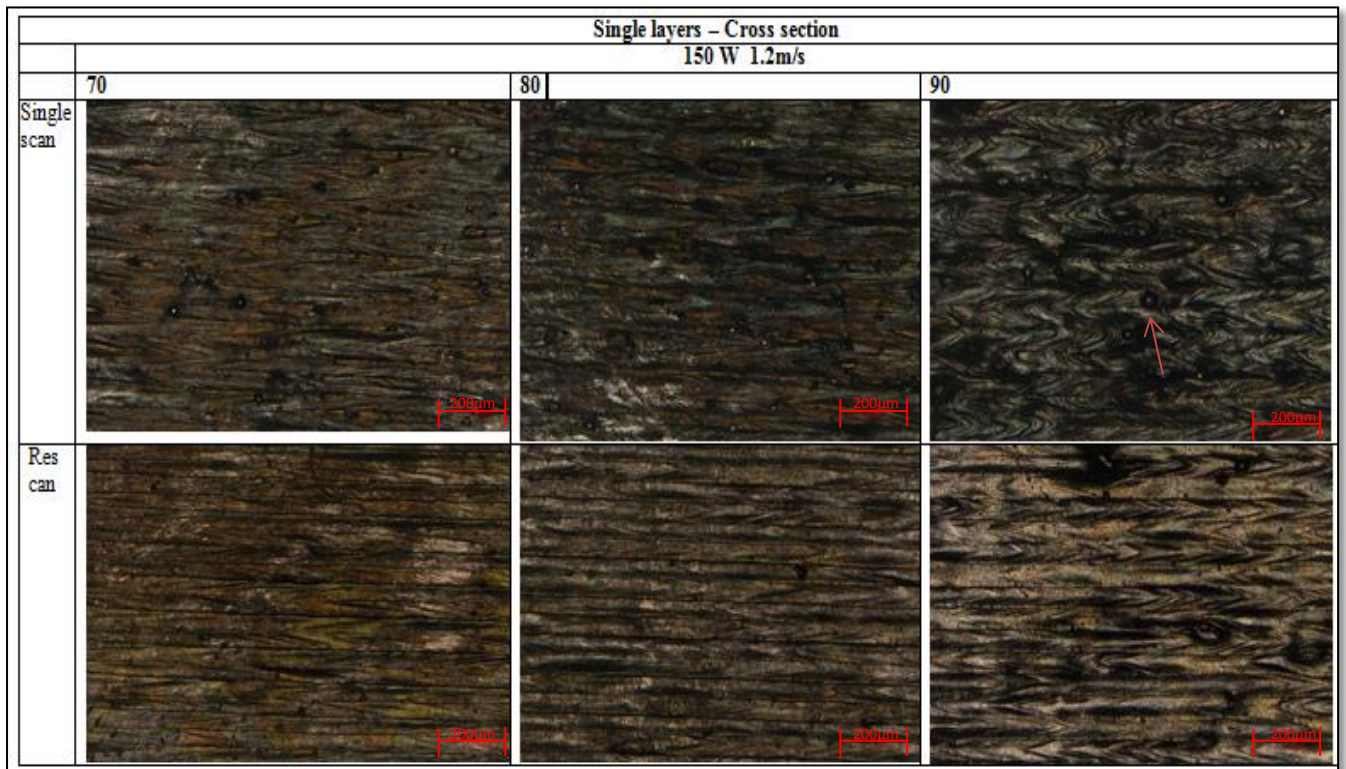


Figure 72. Optical micrographs of the top surfaces of Ti6Al at 150W and 1.2m/s

Figure 73 showed a complete overlap of the single tracks at all three hatch distances. There are no unmelted particles.

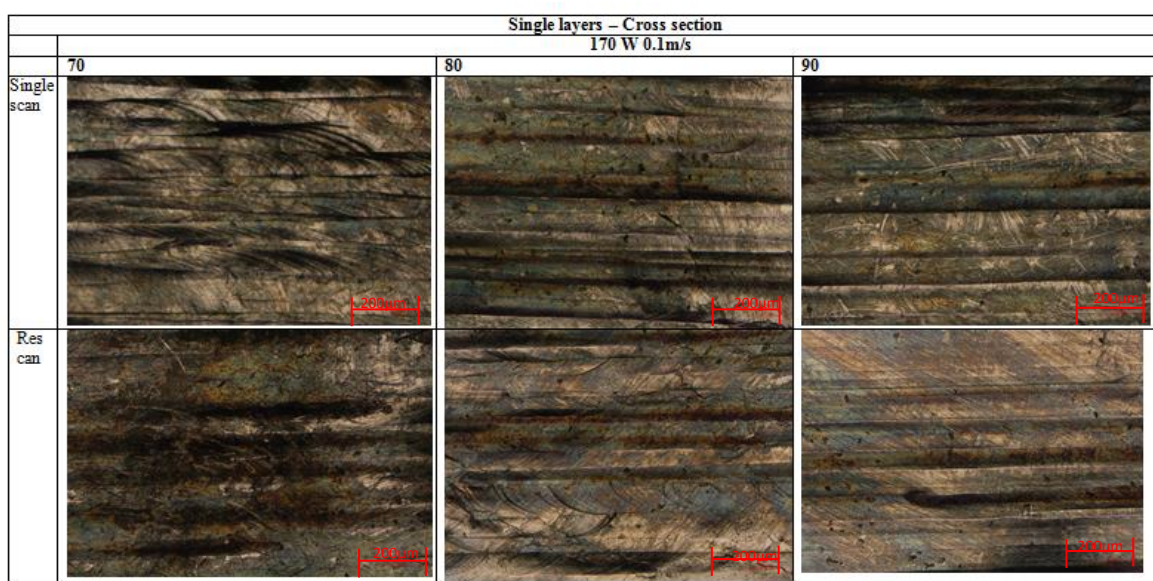


Figure 73. Optical micrographs of the top surfaces of Ti46Al at 170W and 0.1m/s

Surface roughness measurements were taken on the single layers. It is clear that the surface roughness of all the samples is reduced after rescanning. Re-scanning improves the surface homogeneity and melts completely any un-melted powder particles lying on the surface of the single layer (Figure 73).

At both 150W (1.2m/s) and 170W (0.1m/s), the surface roughness increases with an increase in hatch distance. This is because at lower hatch distances, a larger surface area of the previously solidified layer is re-melted which melts any un-melted powder particles. The size of the molten pool surface area increases as the hatch distance increases, and therefore input energy has to be distributed over the increased surface area of the molten pool and still re-melt the previously solidified layer. Due to this, it is expected that surface roughness would increase with increasing hatch distance (Figure 74 and 75).

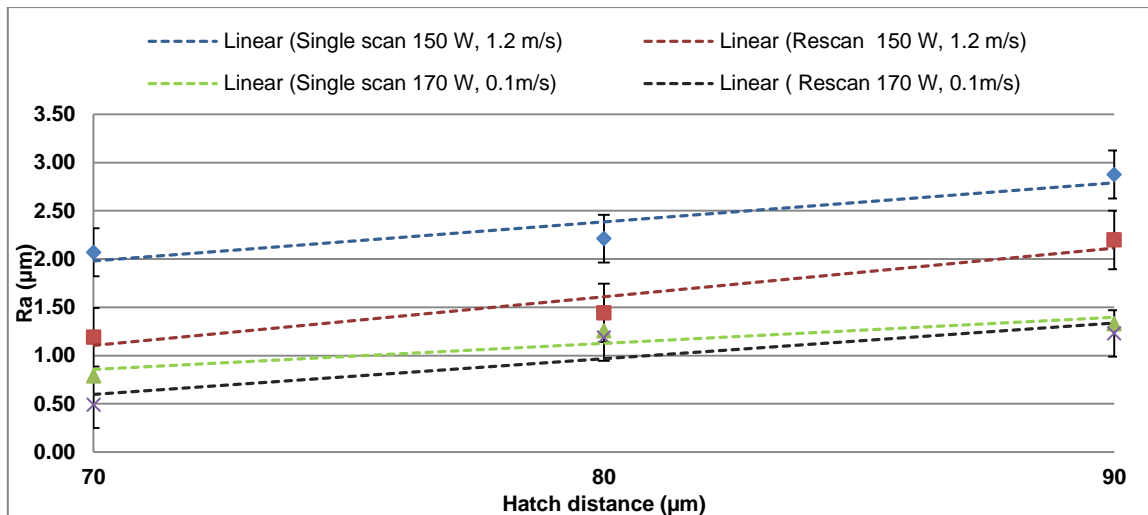


Figure 74. Surface roughness R_a of Ti6Al and Ti46Al at varied hatch distance, laser power and scanning speeds.

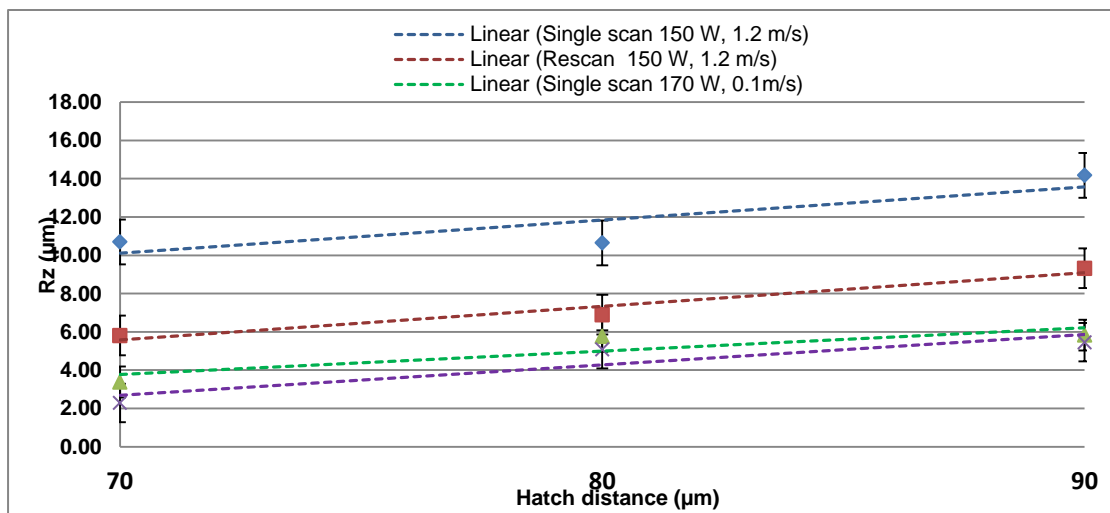


Figure 75. Surface roughness R_z of Ti6Al and Ti46Al at varied hatch distance, laser power and scanning speeds.

In the current experiment, a layer thickness of 60 µm was used. According to the EOS material data sheet for a powder layer thickness of 60 µm, the corresponding R_a value is in the range of 6-10 µm and R_z value in the range of 35-40 µm for Ti6Al4V alloy produced by EOS M280 machine (EOS, 2014). In a Ti6Al4V experiment of cylindrical samples with EOSINT M270 machine, mean values of about 6.2 µm for R_a and 30 µm for the mean roughness R_z were achieved (Longhitano *et al.*,2015). In the current experiment, mean values of about 2 µm for R_a and 10 µm for the mean roughness R_z were achieved on the Ti6Al samples.

Surface roughness plays an important role in mechanical parts, since irregularities on the surface of the part may form nucleation sites for cracks and corrosion. The results achieved in the current study are lower than those achieved from the mentioned experiments are therefore parts with acceptable surface quality can be produced.

4.4.2. Cross-sectional analysis of the single layers

Figure 76 shows optical micrographs of the cross-sectional views of the Ti6Al samples. It can be noted that there is complete melting of the powder particles, and there are no visible satellites. A consistent remelted depth is achieved.

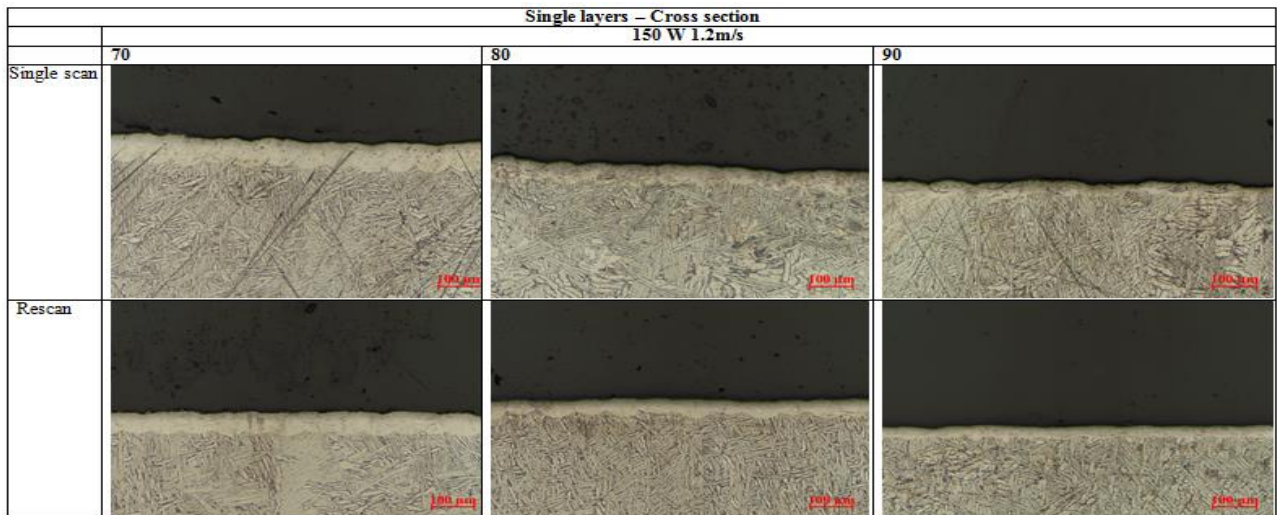


Figure 76. Optical micrographs of the cross-sections of single layers of Ti6Al at 150W and 1.2m/s at different hatch distance, on a single and re-scan method

Figure 77 shows the cross-sectional profiles of the Ti6Al samples at 170 W and 0.1 m/s. The profiles are irregular, with inconsistent penetration, deep penetration to the substrate and poor penetration to the substrate.

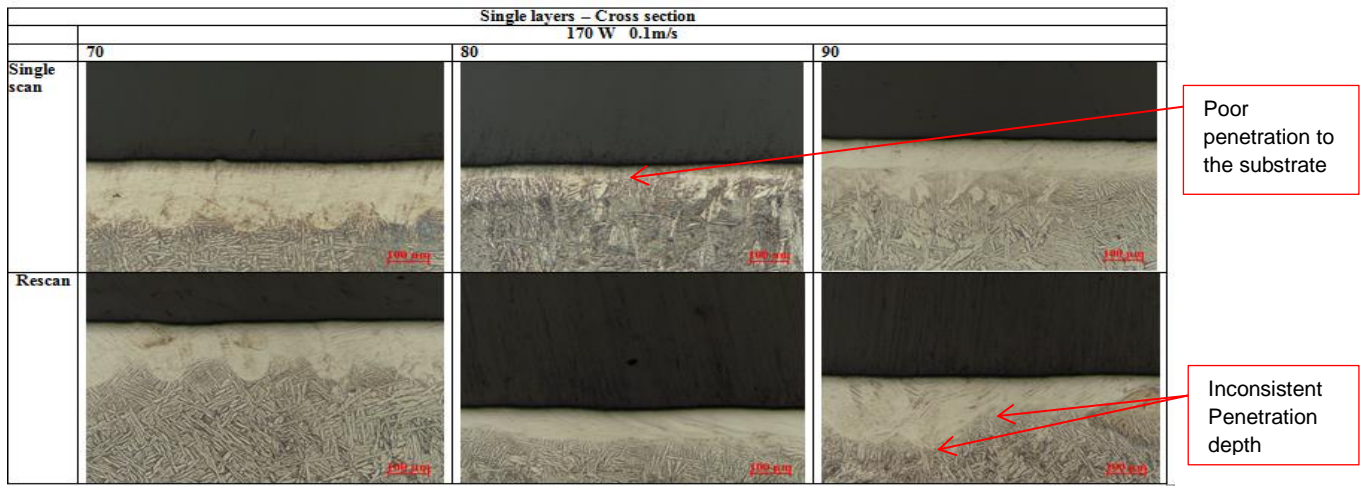


Figure 77. Cross-sections of single layers of Ti6Al at 170W and 0.1m/s at different hatch distances, on a single and re-scan method

EDS analyses of the percentage Al and Ti at different points of the single layers were conducted in the SEM to verify the distribution of the Al in the Ti matrix near the top surface of the layer (Figure 79). The average compound percentage of Al is 3.68 % for the Ti6Al samples, showing a loss of about 2% Al during the in-situ alloying process (Figure 78).

Processing		WDS Setup		WDS Acquisition Status	
Element Setup		Analysis Setup		Compare Information	
Quant Results					
Atom %	Atom % Error	Compnd Formula	Compnd Wt.%	Norm. Compnd	Num. of Cations
6.35	± 0.04	Al	3.68	<u>3.68</u>	---
---	---	Ti	96.32	96.32	---
93.65	± 0.19		---	---	---
-----			-----	-----	
100.00			100.00	100.00	

Figure 78. EDS analysis results for Ti6Al

The results of the Ti46Al show an average of 5,3% for the Ti46Al. There are poor penetration areas on the layer's cross-section on the Ti46Al sample. The poor penetration areas (see figure 77), these areas will cause the point of analysis to be very close to the substrate, as the point of analysis has to be selected and pinned on

the small penetration depth and would influence the correctness of the 5.3% achieved (see pinned labels in figure 79).

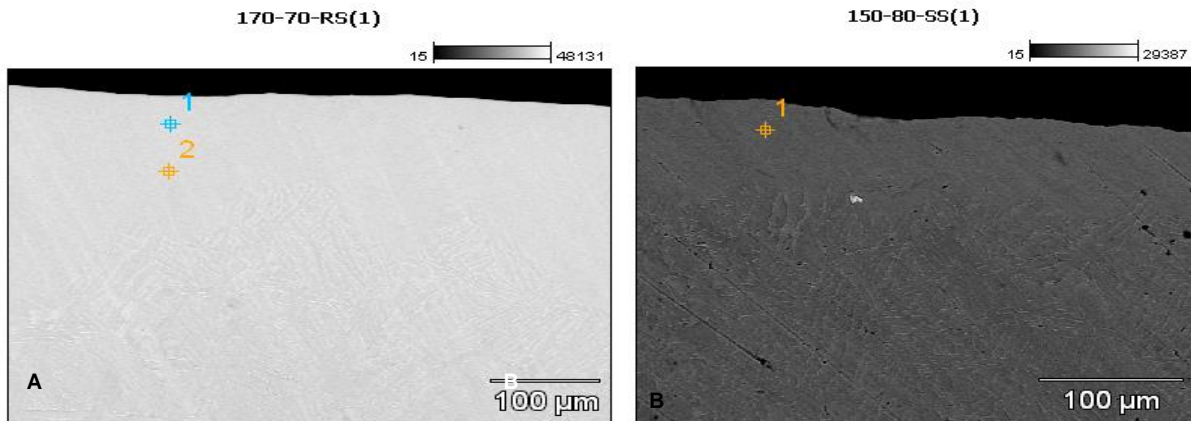


Figure 79. Point analyses of the (a) Ti6Al (b) Ti5Al single layers in the SEM

The impact of the substrate may also affect the Ti6Al samples, even though it is not easy to notice because both the substrate and the Ti6Al samples have the same contents of Al (6%). The observed 2% loss of Al and effect of energy input on *in situ* alloying of a Ti and Al powder mixture can be explained by the differences in the material properties of the two metals as already explained in section 4.1.4.

4.4.3. Analysis of the 3D sample

Figure 80 shows 3D samples (10-layer cubes), produced at 150 W laser power and 1.2 m/s scanning speed and 170 W laser power and 0.1 m/s scanning speed, respectively.

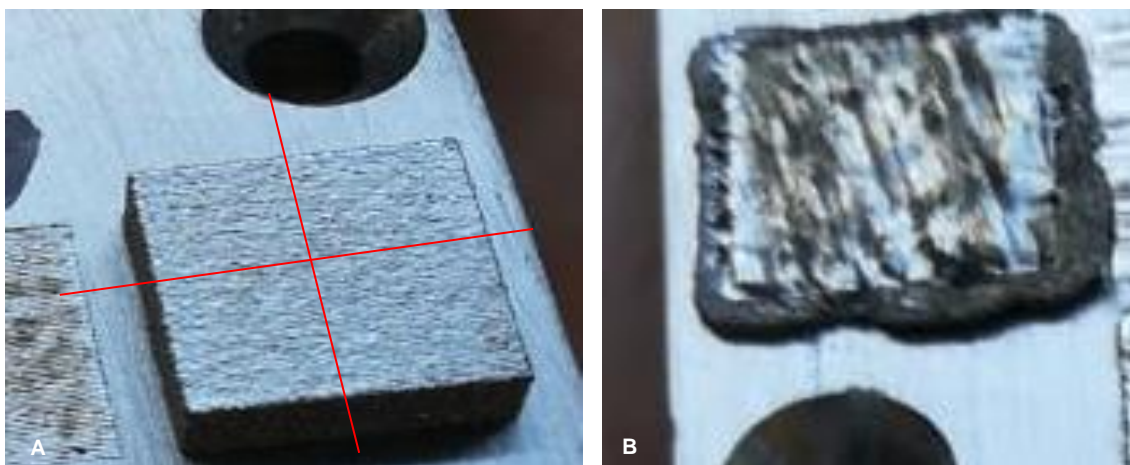


Figure 80. Cubes of (a) Ti6Al at 150W 1.2m/s (b) Ti46Al at 170W 0.1m/s

As can be noted the 3D sample for 170W at 0.1m/s failed to build and collapsed (Figure 80B), and therefore 170W at 0.1m/s was not an optimum process parameter as anticipated. Further analysis is done on the successfully built 150W at 1.2m/s cube (Figure 80A). The Ti6Al cube (Figure 80A) is further cut using a CNC wire cutter into four cubes for analysis of the different planes.

The DMLS technology uses a layer-by-layer building process and that results in different features of the microstructure of DMLS built parts to be visible on sections along different planes. The coordinate system used is illustrated in Figure 81. The build direction is along the Z-axis and the build substrate is in the X-Y plane, with the scanning direction along the X-axis.

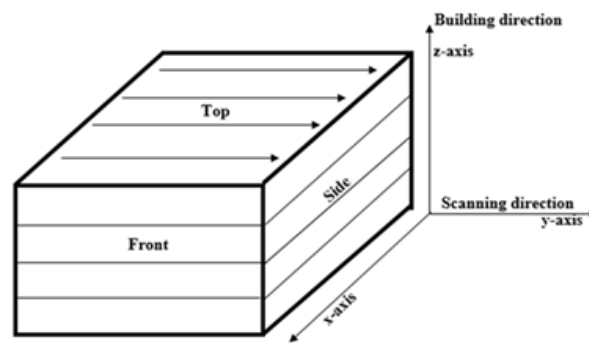


Figure 81. The DMSL scanning co-ordination system

Using the Optical microscope, it was noted that the powder melted completely and there were no visible satellites at the top, side and front planes. The front (y-axis) and the side (x-axis) views microstructures show overlapping of subsequent scanned tracks because of the optimum hatch distance and the selected scanning strategy. The overlapping edges of the single tracks are curved shaped and are noted on the front and the side views (Figure 82). These curves signify merging of each layer into the nearby layers. From figure 82A, $\alpha+\beta$ microstructure is observed, with the primary α grains in the transformed β matrix. In figure 82B and 82C, needles of fine acicular martensitic nature inside the prior β grains of Ti alloy were found and signify high cooling rates during the DMLS process (Thijs *et al.*, 2010)

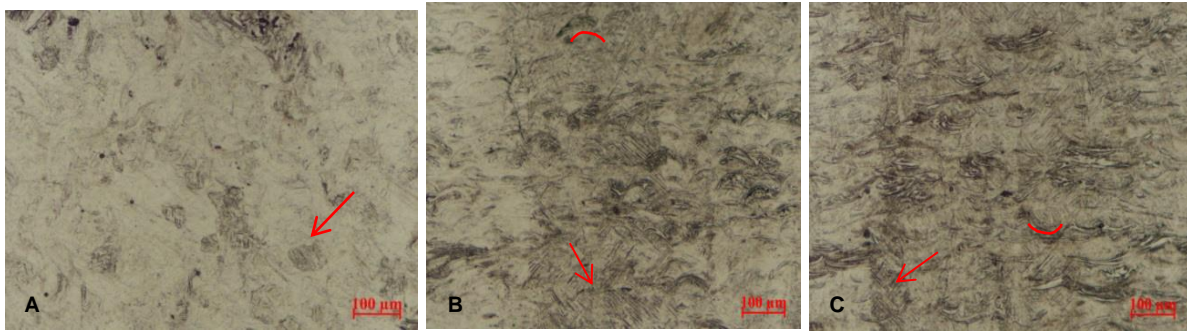


Figure 82. Optical microscope pictures of Ti6Al 3D part (a) Top view (b) Side view (c) Front view

Backscattered electron (BEC) and secondary electron (SEI) images of the three views (top, side and front) were captured. Dark spots on the BEC images were noted and these dark spots appear as small holes in the SEI view (Figure 83). These spots are possible pores on the 3D part. These pores are found in the (x-y plane) in-between the solidified layers. Porosity in-between solidified layers are known as interlayer porosity and can be caused by non-uniform powder delivery. During the layer-by-layer building process of DMLS, if the surface of the previous solidified layer is uneven, then the next powder distribution would be uneven and interlayer pores can form.

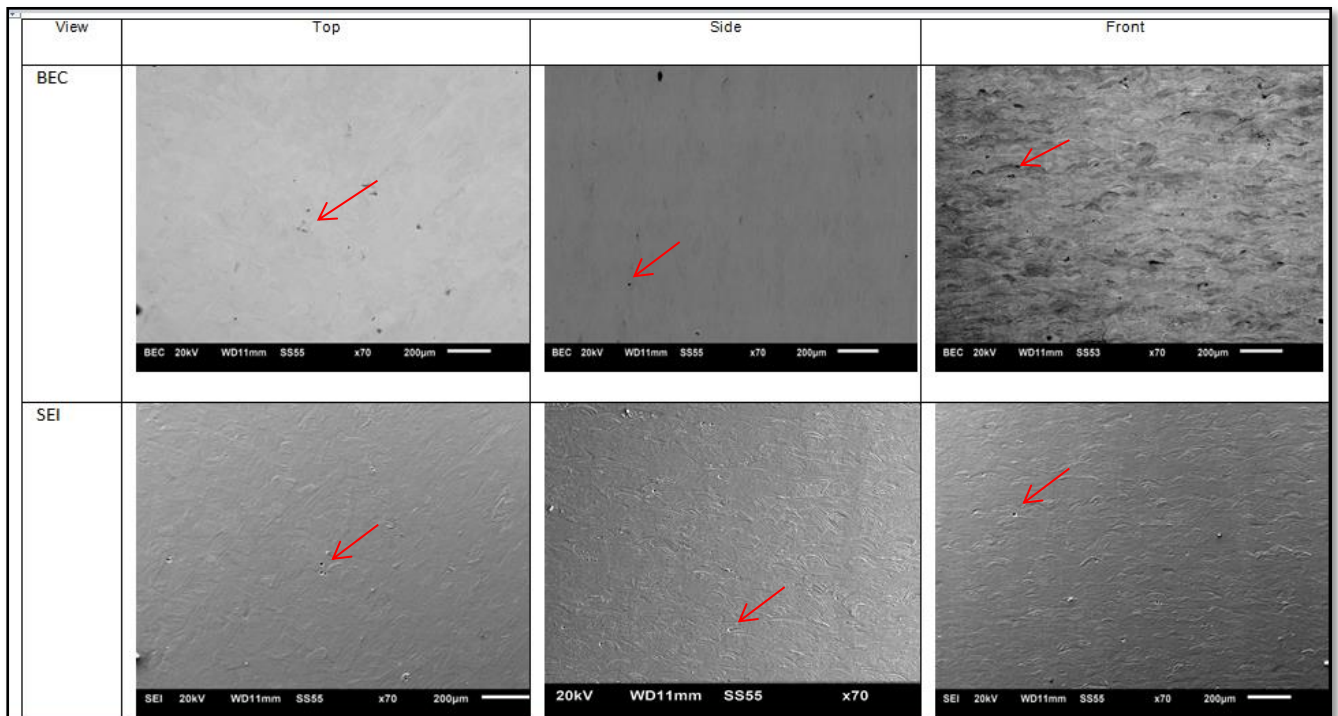


Figure 83. SEI and BEC SEM micrographs of the Ti6Al

Further analysis of the tiny pores was done by re-polishing the sample and using an optical microscope to view the pores; as it gives a clear contrast view on the optical microscope before etching (Figure 84). There is little porosity in random parts of the sectioned views shown in the 3D part, and in general, the part is well built and dense.



Figure 84. Optical microscope pictures of Ti6Al 3D part (a) Top view (b) Side view (c) Front view un-etched.

EDS Al elemental mapping analyses were done for the three views of the 3D part and these are shown in Figure 85. The Al distribution was even and homogeneous. There was an average of 4% Al in the Ti matrix of the 3D part, agreeing to the 2% loss of Al found for the Quant results in figure 79. There was a specific area with a higher concentration of Al noticed. The Al content in this area was about 7 %, which is 3% more than the average Al content in the surrounding.

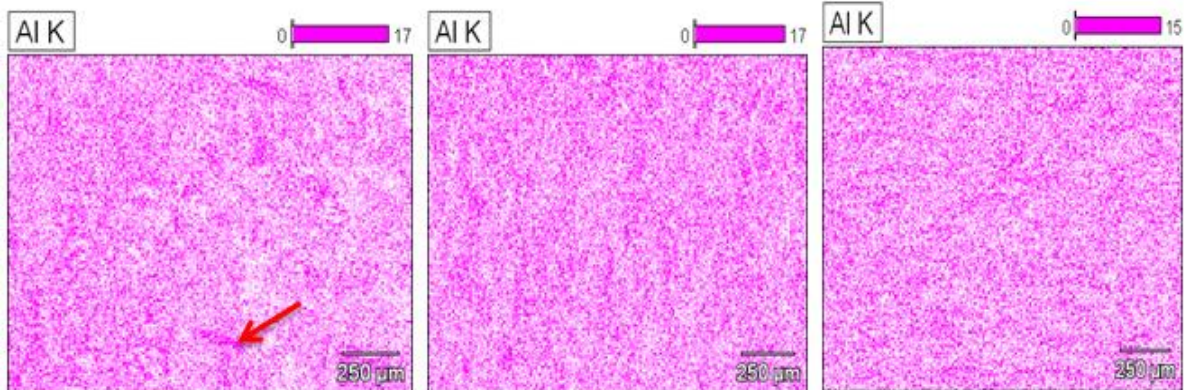


Figure 85. EDS Al elemental mapping of Ti6Al 3D part views (a) Top (b) Side (c) Front

4.4.4. Hardness of Ti6Al DMLS 3D built part

4.4.4.1 Microhardness Tests

The microhardness values of the top, front and the side surfaces of the Ti6Al samples were measured in order to study and understand the hardness properties of the part built through DMLS. Table 10 shows Vickers hardness numbers (VH) measured on these surfaces.

Table 10. Micro-hardness values of Ti6Al 3D part

Process parameters	Top (HV)	Side (HV)	Front (HV)
150 W, 1.2 m/s	319 ±26	339 ±32	322±14

The Vickers hardness values are between 255 – 364 HV as shown in Table 10 and graphically in Figure 86. The HV values have slight differences, depending on the places where the readings were taken on the different surfaces. This agrees to the fact that DMLS build parts are not entirely homogenous throughout the bulk material and this is because of the layer-by-layer building process and the heat conduction direction.

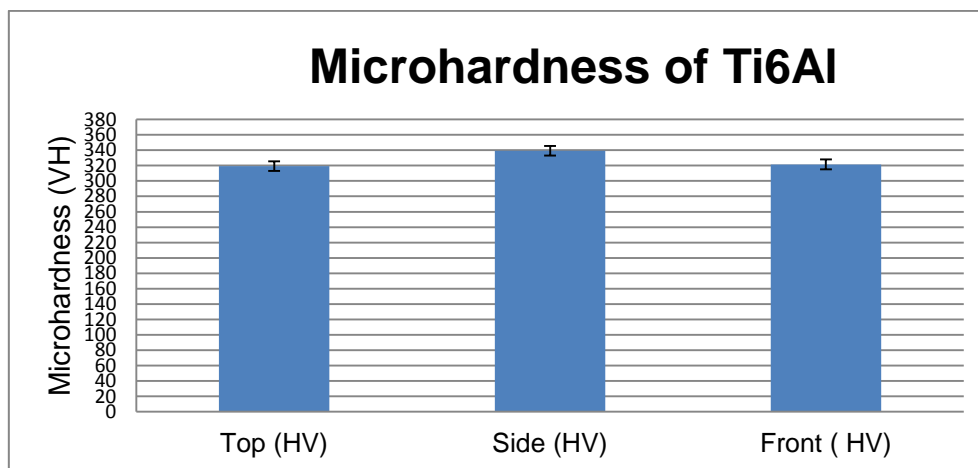


Figure 86. Vickers microhardness of different surfaces of the Ti6Al 3D part

The average VH value for the Ti6Al part built from DMLS is 327 ± 24 . According to the EOS material data sheet for Ti6Al4V alloy produced by EOS M280 machine, a Hardness value of 320 ± 12 (EOS, 2014). The Ti6Al part results show that the part built from this study has hardness comparable to that of other Titanium aluminide alloys (i.e Ti6Al4V).

4.5 Summary

In this chapter, single tracks and single layers were produced from Ti6Al and Ti46Al and optimum process parameters were determined for Ti6Al and not for Ti46Al. A 3D part was successfully built from blended elemental powders of Ti6Al, at optimum process parameters of 150W laser power, 1.2m/s scanning speed and 70 μ m hatch distance. The process parameters of the DMLS process were not relational to each other and an analysis of each parameter's impact is crucial to obtain the required optimum process parameters set.

The pre-mixing process of the elemental powder before the in-situ alloying process is a crucial step of the process, as it has a direct impact on the homogeneity and consistent distribution of the 6% Al in the 94% Ti matrix. Al rich zones were identified on the single layers and areas of the 3D part, refining the mixing process improved the powder distribution and reduced the Al rich zones in the alloyed part.

The process of rescanning improves the surface quality of the single layers. It was noted that after rescanning un-melted powder particles melted and Al rich areas with uneven powder distribution improved. However, the rescanning process increases the time and cost of production.

The Ti46Al 3D sample collapsed and was unsuccessful. The properties and phase of the alloy changes with the increase in Al content. The higher the Al content the more unstable the behaviour of the Al gets, even though a wider range than the Ti6Al range of the process parameters was tested on this study, optimum process parameters for the higher Al content mix (Ti46Al) were still not achieved. There is a 2 % loss of Al in the Ti matrix, which is identified to be caused by the differences in the thermo-physical properties between the powders (Ti and Al). A Vickers micro hardness value of 327 ± 24 was achieved from the Ti6Al 3D built part

CHAPTER 5 – Conclusions and recommendations

5.1 Conclusions

The aim of this study was to determine the feasibility of using the DMLS process to manufacture Titanium aluminide parts from blended elemental powders. From the results presented in the study, the following conclusions can be drawn:

- The objective to identify the optimum process parameters for the blended elemental powders was partially met. Optimum process parameters were successfully identified for the Ti6Al alloy and not for the Ti46Al alloy.
- The approach taken in the research to building a successful part from single tracks, identifying optimum process parameters and then building good single layers and finally building a good 3D part, was only a success for Ti6Al and not for Ti46Al where the single track and single layer showed good results, but the 3D build failed. The reason was the deep penetration depth causing collapse of the 3D structure.
- A homogenous and dense part built from Ti6Al was achieved, with a good microstructure.
- The hardness of the part compared favourably to the known alloys, confirming that a good part can be achieved from the blended elemental powder approach.

5.2 Recommendations

- Since the importance of the powder mixing process was emphasised, a further study on an effective and reliable way to mix the elemental powders is recommended.
- Further study on the Ti6Al4V blended elemental powders can be pursued, as that was the original intended study.
- Further studies on higher percentages of Al in a Titanium aluminide alloy can also be pursued.
- Further studies can be done to investigate the use of different particle sizes for Al to mitigate the loss of Al and improve density homogeneity.

References

- Anton, D.L., Shah, D.M., Duhal, D.N. and Giamei, A.F., 1989. Selecting high-temperature structural intermetallic compounds: the engineering approach. *JOM*, 41(9), p12-17.
- Appel, F., Oehring, M. & Wagner, R., 2000. Novel design concepts for gamma-base titanium aluminide alloys. *Intermetallics*, p1283-1312.
- ASM aerospace, 2016. ASM aerospace specification metals Inc. Available at: <http://www.matweb.com> [Accessed 28 October 2018].
- ISO / ASTM 52900-15, Standard Terminology for Additive Manufacturing – General Principles – Terminology, ASTM International, West Conshohocken, PA, 2015, www.astm.org
- Austin, C.M., 1999. Current Status of Gamma Titanium Aluminides for Aerospace Applications. *Curr Opin Solid State Mater*, 4(2), p39–42.
- AviationPros*, 2015. GE Aviation Rolls Out its 1, 000th GEnx Engine. Available at <http://www.aviationpros.com> [Accessed 11 May 2017].
- AZO, 2015. AZO materials. Available at: <http://www.azom.com> [Accessed 23 June 2017].
- Baudana, G., Biamino, S., Ugues, D., Lombardi, M., Fino, P., Pavese, M. & Badini, C., 2016. Titanium aluminides for aerospace and automotive applications processed by Electron Beam Melting. *Elsevier*, p193-199.
- Benson, J.M. & Snyders, E., 2015. The need for powder characterisation in the additive manufacturing industry and the establishment of a national facility. *South African Journal of Industrial Engineering*, 26(2), p104-114.
- Bergström, D., Powell, J. & Kaplan, A.F. H., 2007. A ray-tracing analysis of the absorption of light by smooth and rough metal surfaces. *Journal of Applied Physics*, 101(11), p113504.
- Bertol, L.S., Júnior, W.K., da Silva, F.P. & Aumund-Kopp, C., 2010. Medical design: direct metal laser sintering of Ti–6Al–4V. *Materials & Design*, 31(8), p3982-3988.
- Blackburn, M.J. Hill, J.T. & Smith, M.P., (1984). *Technical report AFWAL-TR-84-4078*. Ohio: WPAFB.

- Blackburn, M.J & Smith, M.P., (1978). *Technical Report AFML-TR-78-18*. Ohio: WPAFB.
- Blackburn, M.J & Smith, M.P., (1980). *Technical Report AFWAL-TR-80-4175*. Ohio: WPAFB.
- Bolzoni, L., Esteban, P.G., Ruiz-Navas, E.M. & Gordo, E., 2012. Mechanical behaviour of pressed and sintered titanium alloys obtained from prealloyed and blended elemental powders. *Journal of the Mechanical Behaviour of Biomedical Materials*, p29-38.
- Bradley, E.F., (1989). *Investment, Licensing and Strategic Partnering Opportunities, Emerging Technology, Applications, and Markets for Aluminides, Iron, Nickel and Titanium*. California: Monterey.
- Chesnutt, J., 1992. Titanium aluminides for aerospace applications. *Superalloys*, p381- 389.
- Court, S. A., Löfvander, J.P.A., Loretto, M.H. & Fraser, H.L., 1990. The influence of temperature and alloying additions on the mechanisms of plastic deformation of Ti3Al. *Philosophical Magazine* , p109 -139.
- Dimiduk, D.M., 1999. “Gamma Titanium Aluminide Alloys—an Assessment within the Competition of Aerospace Structural Materials.” *Materials Science and Engineering*, A263 (2), p281–88.
- Dilberoglu, U.M., Gharehpapagh, B., Yaman, U. & Dolen, M., 2007. The role of additive manufacturing in the era of industry 4.0. *Procedia Manufacturing*, p545-554.
- Donachie, M.J., 1982. *Introduction to titanium and titanium alloys*. Michigan: ASM International.
- Donachie, M.J., 2000. *Titanium: A Technical Guide, 2nd Edition*. Michigan: ASM International.
- Donachie, M.J., 2015. A Guide to engineering Selection of Titanium Alloys for Design. *Mechanical Engineer's Handbook*, p1-37.
- Eagar, T.W. & Tsai, N.S., 1983. Temperature fields produced by traveling distributed heat sources. *Welding Journal*, 62(12), p346-355.
- Elagli, K., Hildebrand, H.F. & Hamme, G., 1989. Biocompatibility of titanium and its alloys. *Le Chirurgien-dentiste de France*, 59(457), p35.

- EOS GmbH, 2016. EOS-alphaform-produces-hip-implant-by-using-additive-manufacturing. Available at <http://additive manufacturing.com> [Accessed 11 May 2017]
- EOS, 2014. Material data sheet, EOS Titanium Ti64: EOS GmbH - Electro Optical Systems.
- Fabbro, R., 2011. Melt Pool and Keyhole Behaviour Analysis for Deep Penetration Laser Welding. *Journal of physics D: applied Physics*, 43(44), p.445501.
- Ferrar, B., Mullen, L., Jones, E., Stamp, R. & Sutcliffe, C.J., 2012. Gas flow effects on selective laser melting (SLM) manufacturing performance. *Journal of Materials Processing Technology*, p355-364.
- Fischer, P., Romano, V., Weber, H.P., Karapatis, N.P., Boillat, E. & Glardon, R., 2003. Sintering of commercially pure titanium powder with a Nd: YAG laser source. *Acta Materialia*, 51(6), p1651-1662.
- Fraunhofer Institute, 2003. Generative Manufacturing Methods: Selective Laser Melting. Available at: <http://www.fraunhofer.de> [Accessed 12 July 2016]
- Froes, F.H., Suryanarayana, C. & Eliezer, D., 1992. Synthesis properties and applications of titanium aluminides. *Journal of materials science*, 27(19), p5113-5140.
- Gusarov, A.V. & Smurov, I., 2010. Modeling the interaction of laser radiation with powder bed at selective laser melting. *Physics Procedia*, 5, p 381-394.
- Gusarov, A.V., Yadroitsev, I., Bertrand, P.H. & Smurov, I., 2009. Model of radiation and heat transfer in laser powder zone at selective laser melting. *Journal of heat transfer*, 131(7), p72-101.
- Huang, S.C. & Siemers, P.A., (1989). Characterization of the high-temperature phase fields near stoichiometric γ -TiAl. *Metallurgical Transactions*, p1899-1906.
- Jacobson, D.M. & Bennett, G., 2006. Practical issues in application of direct metal laser sintering. *In Solid Freeform fabrication Symposium*, Austin, Texas, 2006.
- Kear, B.H., 1970. *Ordered alloys: structural applications and physical metallurgy*. Lake George, NY: Claitor.
- Kelly, S.M., 2004. *Thermal and microstructure modeling of metal deposition processes with application to Ti-6Al-4V*. Doctoral thesis: Virginia Polytechnic Institute and State University.

- Khaing, M. W., Fuh, J.Y.H. & Lu, L., 2001. Direct metal laser sintering for rapid tooling: processing and characterisation of EOS parts. *Journal of Materials Processing Technology*, 113(1), p269-272.
- Kim, Y.W. & Froes, F.H., (1990). *High Temperature Aluminides and Intermetallics*. Pennsylvania: Warrendale,.
- Kim, Y.W & Dimiduk, D. M., 1991. Progress in the understanding of gamma titanium aluminides. *Jom*, 43(8), p40 - 47.
- Kim, Y.W., (1991). High Temperature Ordered Intermetallic Alloys IV. In D.P.L.A. Johnson (Ed.), MRS, Pittsburgh, Pennsylvania.
- Kruth, J.P., Froyen, L., Van Vaerenbergh, J., Mercelis, P., Rombouts, M. & Lauwers, B., 2004. Selective laser melting of Iron-based powder. *Journal of materials processing Technology*, 616 - 622.
- Kruth, J.P. Mercelis, P., Van Vaerenbergh, J., Froyen, L.& Rombouts, M. 2005. Binding mechanisms in selective laser sintering and selective laser melting. *Rapid Prototyping Journal*,11, p26-36.
- Kruth, J. P., Badrossamay, M., Yasa, E., Deckers, J., Thijs, L. & Van Humbeeck, J., 2010. 'Part and material properties in selective laser melting of metals'. ISEM:XVI. *16th international symposium on electromachining*. Shanghai,China, 19 -23 April 2010.
- Kurzynowski, T., Chlebus, E., Kuźnicka, B. & Reiner, J., 2012. Parameters in selective laser melting for processing metallic powders. *International Society for Optics and Photonics, In SPIE LASE*, V8239, p823914
- Lancea, C., Chicos, L.A., Zaharia, S.M. & Pop, M.A., 2017. Microstructure and micro-hardness analyses of titanium alloy Ti-6Al-4V parts manufactured by selective laser melting. *EDP Sciences*, 94, p3009).
- Lei, Y., Xueyang, C., Wei, L., Frank, L. & Newkirk. J., (2016). Direct laser deposition of Ti-6Al-4V from elemental powder blends. *Rapid prototyping journal*, 22(5), p810-816.
- Lewandowski, J.J. & Seifi, M., 2016. Metal Additive Manufacturing: A review of mechanical properties. *Annual review of materials research*, p151-186.
- Lipsitt, H.A., 1985. *High Temperature Ordered Intermetallic Alloys*. MRS: Pittsburgh.
- Liu, C.T., Froes, F.H. & Stiegler, J.O.,1990. *Metals handbook*, 10th Edn, ASM International, Ohio, Materials Park.

- Liu, C.T., Schneibel, J.H., Maziasz, P.J., Wright, J.L. & Easton D.S., 1996. Tensile Properties and Fracture Toughness of TiAl Alloys with Controlled Microstructures. *Intermetallics* 4(6), p429–440.
- Loeber, L., Biamino, S., Ackelid, U., Sabbadini, S., Epicoco, P., Fino, P. & Eckert, J., (2011). *Comparison of selective laser and electron beam melted titanium Aluminides*. Torino: Leibniz Institute for Solid State and Materials Research.
- Löfvander, J.P.A., Court, S.A., Loretto, M.H. & Fraser, H.L., 1989. Mobility of c dislocations in Ti₃Al. *Philosophical Magazine Letters*, 60(3), p111-116.
- Longhitano, G. A., Larosa, M.A., Munhoz, A.L.J., Zavaglia, C.A.D.C. & Ierardi, M.C.F., 2015. Surface Finishes for Ti-6Al-4V Alloy Produced by Direct Metal Laser Sintering. *Materials Research*, 18(4), p838-842.
- Matilainen, V.P., Piili, H., Salminen, A. & Nyrhilä, O., 2015. Preliminary investigation of keyhole phenomena during single layer fabrication in laser additive manufacturing of stainless steel. *Physics Procedia*, 78, p377-387.
- McCullough, C., Valencia, J.J., Levi, C.G. and Mehrabian, R., 1988. The high temperature α field in the titanium-aluminum phase diagram. *Scripta metallurgica*, p1131-1136.
- McGeary, R.K., 1961. Mechanical Packing of spherical particles. *Journal of American Ceramic Society*, p1151-2916.
- Meiners, W. & Bremen, S., 2012. Selective Laser Melting - A manufacturing technology for the future. *Laser Technik Journal*, 9(2), p33–38.
- Mumtaz, K.A. & Hopkinson, N., 2010. Selective laser melting of thin wall parts using pulse shaping. *Journal of Materials Processing Technology*, 210(2), p279–287.
- Qiu, C., Adkins, N.J.E. & Attallah, M.M., 2013. Microstructure and tensile properties of selectively laser-melted and of HIPed laser-melted Ti–6Al–4V. *Materials Science and Engineering*, p230–239.
- Rai, R.E.W., 2007. Heat transfer and fluid flow during keyhole mode laser welding of tantalum, Ti–6Al–4V, 304L stainless steel and vanadium. *Journal of Physics D and Applied Physics*, 40(18), p5753.
- Sames, W.J., List, F.A., Pannala, S., Dehoff, R.R. & Babu, S.S., 2016. The metallurgy and processing science of metal additive manufacturing. *International Materials Reviews*, 61(5), p315-360.

- Sastry, S .M.L & Lipsitt, H.A., 1977. Ordering transformations and mechanical properties of Ti 3 Al and Ti 3 Al-Nb alloys. *Metallurgical Transactions*, p1543.
- Simonelli, M., Aboulkhair, N., Cohen, P., Murray, J., Clare, A.T., Tuck, C., & Hague, R.J., 2018. A Comparison of Ti-6Al-4V in-situ alloying in Selective Laser Melting using simply-mixed and saellite powder blend feedstocks. *Materials Characterization*, 143, p118-126.
- Spierings, B., Herres, N. & Levy, G. 2011. 'Influence of the particle size distribution on surface quality and mechanical properties in additive manufactured stainless steel parts'.SFF.*Solid Freeform Fabrication Symposium*. Austin, Texas.8-10 August 2011.
- Stoloff, N.S. & Davies, R.G. 1960. *Mechanical Properties of Intermetallic Compounds*, 13 edn. JH Westbrook, New York.
- Sun, S., Brandt, M. & Easton, M., 2017. Powder bed fusion processes: An overview. *In Laser Additive manufacturing*, p55 -77.
- Sun, Z. & Karppi, R., 1996. The application of electronic beam welding for joining dissimilar metals: An overview. *Journal of Materials Processing Technology*, p257-267.
- Terner. M., Biamino, S., Baudana, G., Penna, A., Fino, P., Pavese, M., Ugues, D. & Badini, C., 2015. Initial oxidation behavior in air of TiAl-2Nb and TiAl-8Nb alloys produced by electron beam melting. *Journal of Materials Engineering and Performance*, p3982-3988.
- Thijs, L., Verhaeghe, F., Craeghs, T., Van Humbeeck, J. & Kruth, J.P., 2010. A study of the microstructural evolution during selective laser melting of Ti–6Al–4V. *Acta Materialia*, 58(9), pp. 3303-3312.
- Thomas, M., Malot,T., Aubry,P., Colin, C., Vilaro,T. and Bertrand,P., 2016. The Prospects for Additive Manufacturing of Bulk TiAl Alloy. *Materials at High Temperatures*, 33(4–5), p571–77.
- Toshimitsu, T., Kentaro, S., Satoshi, K., Satoru, K. & Masao, T., 2005. Fabrication of TiAl Components by Means of Hot Forging and Machining. *Elsevier*, 13(9), p971–978.
- Voice,W.E., Henderson,M., Shelton,E.F & Wu,X., 2005. Gamma Titanium Aluminide, TNB. *Intermetallics*, 13 (9),p959–964.
- Vydehi, J.A., 2006. *Titanium alloys: an atlas of structures and fracture features book*. CRC Press,New York.

- Wei.C., Yukinori.Y., William H., 2010. Investigation of pressing and sintering processes of CP-Ti powder made by Armstrong Process . *Key Engineering Materials*, p123-130.
- WebElements, 2019. WebElements. Available at <http://www.webelements.com> [Accesse 25 June 2019].
- William, E. & Frazier, 2014. Metal Additive manufacturing - A review. *Journal of Material Engineering and Perfomance*,23(6), p1917-1928.
- Yadroitsava, I., Els, J.,Booyesen, G. & Yadroitsev, I., 2015. Peculiarities of single track formation from Ti6AL4V alloy at different laser power densities by SLM. *South African Journal of Industrial Engineering*, 26 (3), p86-95.
- Yadroitsev, I., Gusarov, A.,Yadroitsava, I. & Smurov, I., 2010. Single track formation in selective laser melting of metal powders. *Journal of Materials Processing Technology*, 210(12), p1624-1631.
- Yadroitsev, I., 2009. *Selective laser melting: Direct manufacturing of 3D-objects by selective laser melting of metal powders*. LAP Lambert Academic Publishing, Saarbrücken, Germany.
- Yadroitsev, I., Bertrand, P. & Smurov, I., 2007. Parametric analysis of the selective laser melting process. *Applied Surface Science*, p8064–8069.
- Yadroitsev, I., Krakhmalev, P., Yadroitsava, I., Johansson, S. & Smurov, I., 2013. Energy input effect on morphology and microstructure of selective laser melting single track from metallic powder. *Journal of Materials Processing Technology*, 213(4), p6.
- Yadroitsev, I., Krakhmalev, P. & Yadroitsava, I., 2015. Hierarchical design principles of selective laser melting for high quality metallic objects. *Additive Manufacturing*,7, p45-56.
- Yadroitsev.I, Yadroitsava.I., Bertrand. P. & Smurov, I., 2012. Factor analysis of selective laser melting process parameters and geometrical characteristics of synthesized single tracks. *Rapid Prototyping Journal*, 18(3), p201-208.
- Yu, J., Rombouts, M., Maes, G. & Motmans, F., 2012. Material properties of Ti6Al4V parts produced by laser metal deposition. *Physics Procedia*, 39, p416 - 424.

